Université du Québec à Chicoutimi

New generation of high performance aluminum electrical conductors for elevated temperature applications

By

Quan Shao

Under supervision of Prof. X.-Grant Chen, and co-supervision of Prof. Emad Elgallad, and industrial supervision of Dr. Alexandre Maltais

Thesis Presented to Université du Québec à Chicoutimi in Partial Fulfillment of the Requirements for the Degree of Doctor of Philosophy Ph.D.

Defended on 3 September 2025

BOARD OF EXAMINERS:

Professor Mousa Javidani, Department of Applied Sciences at UQAC, President of the board of Examiners

Professor, Daniel Larouche, Department of Mining, Metallurgy and Materials Engineering at Laval University, External Member of Examiners

Professor X.-Grant Chen, Department of Applied Sciences at UQAC, Internal Member of Examiners

Professor Emad Elgallad, Department of Applied Sciences at UQAC, Internal Member of Examiners

Professor Dilip Sarkar, Department of Applied Sciences at UQAC, Internal Member of Examiners

Québec, Canada

Nouvelle génération de conducteurs électriques en aluminium haute performance pour des applications à haute température

Résumé

La demande croissante en électricité et l'expansion des activités industrielles nécessitent le développement de nouveaux alliages conducteurs d'aluminium dotés de propriétés mécaniques et thermiques supérieures. Au Canada, plus de 166 000 kilomètres de lignes de transmission aériennes, dont une grande partie traverse des zones forestières, présentent une vulnérabilité importante en raison de la faible résistance mécanique et thermique des alliages conventionnels d'aluminium, augmentant les risques de pannes de courant et d'incendies de forêt. Bien que les alliages Al-Mg-Si de la série 6xxx soient couramment utilisés pour les conducteurs en aluminium, leur faible résistance thermique (inférieure à 100 °C) limite leur performance à haute température. En revanche, les alliages Al-Zr-Sc offrent une meilleure résistance mécanique et une grande stabilité thermique grâce à la formation de nanoparticules cohérentes $Al_3(Sc,Zr)$ de structure $L1_2$, permettant une utilisation à des températures bien plus élevées (180 à 310 °C). Cette étude vise à développer une nouvelle génération d'alliages conducteurs en aluminium thermiquement stables, combinant une conductivité électrique élevée avec d'excellentes performances mécaniques et thermiques. Elle est structurée en trois parties comme suit.

Dans la première partie, des alliages conducteurs à base d'Al-Zr résistants à la chaleur ont été développés par microalliage avec une faible teneur en Sc ($\leq$ 0,10 % en poids) et deux voies de traitement thermomécanique, dans lesquelles le tréfilage à froid a été réalisé avant ou après le traitement de vieillissement. Les propriétés mécaniques, la conductivité électrique et la résistance thermique de plusieurs alliages ont été évaluées selon la norme CEI relative aux conducteurs en aluminium résistants à la chaleur. L'évolution des précipités et de la structure des grains au cours du traitement a également été étudiée. L'ajout de Sc a conduit à la précipitation d'un grand nombre de particules fines $Al_3(Sc,Zr)$, procurant une résistance élevée de 188 à 209 MPa, soit une amélioration de 73 à 88 % par rapport à l'alliage de base sans Sc, tout en maintenant une excellente conductivité électrique de 57,4 à 59,9 % IACS. De plus, les alliages contenant du Sc ont présenté une excellente résistance thermique, la perte maximale de résistance étant limitée à $\leq$ 6,0 % après exposition thermique à 310 et 400 °C. Les meilleures combinaisons de propriétés mécaniques et de conductivité ont été obtenues après un vieillissement à 350 °C pendant 48 h, précédé d'un traitement de solution à 600 °C pendant 8 h. Les deux voies de traitement ont montré des renforcements comparables par précipitation et écrouissage, conduisant à des propriétés mécaniques et électriques similaires, avec des écarts maximaux de 12 MPa en résistance et de 1,4 % IACS en conductivité. L'excellent compromis entre propriétés mécaniques, électriques et thermiques fait de ces alliages de nouveaux candidats prometteurs pour la fabrication de conducteurs en aluminium thermorésistants conformes à plusieurs grades normalisés, tout en conservant un coût abordable et des procédés industriels classiques.

Dans la deuxième partie, quatre alliages conducteurs Al-Zr-Sc contenant entre 0,1 et 0,18 % Zr et entre 0,1 et 0,15 % Sc ont été élaborés par coulage, laminage à chaud, traitements thermiques et tréfilage à froid. Les propriétés mécaniques et la conductivité des fils ont été mesurées, et la microstructure a été caractérisée par microscopie électronique à balayage (MEB), microscopie électronique en transmission (MET) et diffraction d'électrons rétrodiffusés (EBSD). La stabilité thermique de ces alliages a été évaluée systématiquement après exposition à 310, 350 et 400 °C pendant jusqu'à 1000 h. Les résistances à la traction ultime (UTS) atteintes étaient comprises entre 206 et 214 MPa, et la conductivité électrique entre 57 et 57,5 % IACS. Tous les alliages ont été renforcés par une grande quantité de nanoprécipités $Al_3(Sc,Zr)$. Une légère augmentation de l'UTS a été observée avec l'augmentation de la teneur en Zr ou en Sc, indiquant un impact limité de leur teneur sur les propriétés mécaniques et électriques. Aucun changement notable de la résistance mécanique ni de la structure des grains déformés n'a été observé après exposition à 310 °C jusqu'à 1000 h. À 350 °C pendant 200 h, les alliages ont conservé une excellente stabilité thermique. En revanche, des expositions prolongées à 350 et 400 °C ont entraîné une dégradation progressive des propriétés mécaniques. Les alliages Al-0,18Zr-0,1Sc et Al-0,18Zr-0,15Sc ont montré une meilleure stabilité thermique à long terme à 350 et 400 °C. Cette étude fournit des données précieuses pour l'utilisation industrielle de fils conducteurs en aluminium dans des conditions extrêmes.

Dans la troisième partie, de faibles ajouts d'étain (Sn, 0,05 et 0,15 % en poids) et de strontium (Sr, 0,006 et 0,013 % en poids) ont été introduits dans des alliages Al–Zr–Sc afin d'en étudier l'effet sur la microstructure et les propriétés mécaniques. Des paramètres de vieillissement en deux étapes ont été optimisés séparément pour les alliages contenant Sn et Sr, en fonction de l'évolution de la microdureté et de la conductivité électrique sous différentes conditions de traitement. Dans l'alliage Sn15, le vieillissement en deux étapes a permis d'atteindre une microdureté et une conductivité de 78,3 HV et 58,3 % IACS, contre 74,2 HV et 57,5 % IACS avec un vieillissement traditionnel. De même, l'alliage Sr13 a atteint 83,2 HV et 58,0 % IACS après vieillissement en deux étapes, contre 78,3 HV et 57,5 % IACS avec le vieillissement traditionnel. La résistance à la traction ultime est passée de 205,9 MPa à 215,9 MPa pour l'alliage Sn15, et de 214,9 MPa à 226,5 MPa pour l'alliage Sr13. Ces améliorations – 0,8 % IACS, 5,5 HV et 10,7 MPa pour Sn15 ; 0,7 % IACS, 5,2 HV et 10,9 MPa pour Sr13 – sont principalement attribuées à une densité plus élevée de précipités $Al_3(Sc,Zr)$ de très petite taille. Des précipités à un stade précoce ont été observés dans l'alliage Sn15 après vieillissement à 300 °C pendant 4 h. Dans les alliages contenant du Sr, le renforcement est également lié à une résistance accrue au mouvement des dislocations due à la présence de défauts d'empilement. L'ajout de traces de Sn ou de Sr, combiné à un vieillissement en deux étapes, constitue une stratégie rentable pour développer une nouvelle génération d'alliages conducteurs en aluminium, stables à haute température et à haute performance.

New generation of high performance aluminum electrical conductors for elevated temperature applications

Abstract

The increasing demand for electricity and the expansion of industrial activities necessitate the development of advanced conductor alloys with superior mechanical and thermal properties. In Canada, over 166,000 kilometers of overhead transmission lines, many passing through forested regions, are vulnerable due to the low strength and poor thermal resistance of conventional aluminum conductor alloys, leading to risks such as power failures and forest fires. While Al-Mg-Si 6xxx alloys are commonly used for aluminum conductor alloys, their limited thermal resistance (below 100 °C) restricts their performance under elevated temperatures. In contrast, Al-Zr-Sc alloys offer enhanced strength and thermal stability through the formation of coherent $L1_2$-$Al_3(Sc,Zr)$ nanoparticles, enabling operation at much higher temperatures (180–310 °C). This study aims to explore a new generation of thermally stable aluminum conductor alloys that combine high electrical conductivity with excellent mechanical and thermal performance. It is presented in three parts as outlined below.

In the first part, thermal-resistant Al-Zr based conductor alloys were developed using microalloying with a low level of Sc ($\leqslant$ 0.10 wt.%) and two thermomechanical processing routes, in which the cold wire drawing was conducted before and after the aging treatment. The mechanical properties, electrical conductivities, and thermal-resistant properties of several alloys were investigated and evaluated according to the IEC standard of thermal-resistant aluminium conductors. The evolutions of the precipitates and grain structure during processing were also studied. The microalloying with Sc resulted in the precipitation of a large number of fine $Al_3(Sc,Zr)$ precipitates, which provided substantially high strength of 188-209 MPa, representing 73-88% improvement compared to the Sc-free base alloy, while maintaining excellent electrical conductivity of 57.4-59.9% IACS. Moreover, the Sc-containing alloys exhibited outstanding thermal-resistant properties, where the maximum strength reduction was limited to $\leqslant$ 6.0% after thermal exposures at 310 and 400 ºC. The best combinations of mechanical properties and electrical conductivities of the Sc-containing alloys were obtained after aging at 350 ºC for 48 h, following solutionizing at 600 ºC for 8 h. Both processing routes yielded comparable precipitation strengthening and strain hardening, and consequently comparable mechanical and electrical properties, where the maximum differences in the strength and electrical conductivity between both routes were 12 MPa and 1.4% IACS, respectively. The excellent combinations of mechanical, electrical, and thermal-resistant properties made the developed alloys promising candidate materials for four standard grades of thermal-resistant aluminium conductors, while taking advantage of an affordable material cost and using conventional thermomechanical processes.

In the second part, four Al-Zr-Sc conductor alloys with 0.1–0.18 wt.% Zr and 0.1–0.15 wt.% Sc were processed through casting, hot rolling, heat treatments, and cold wire drawing. The mechanical properties and electrical conductivities of the alloy wires were

evaluated, and the microstructures were characterized using scanning electron microscopy, transmission electron microscopy, and electron backscattering diffraction techniques. The thermal stabilities of these alloys were systematically assessed during thermal exposures at 310, 350, and 400 °C for up to 1000 h. The ultimate tensile strengths (UTSs) of four Al-Zr-Sc alloy wires reached 206–214 MPa, while the electrical conductivities were 57%–57.5% IACS. All four alloy wires were strengthened by a large number of $Al_3(Sc,Zr)$ nanoprecipitates. With the increase in Zr or Sc content, the UTS only slightly increased, which shows a low impact of the Zr and Sc levels on the tensile strength and electrical conductivity. Notably, remarkable reduction in tensile strength and change in the deformed grain structure were not observed for the four alloy wires during thermal exposure at 310 °C for up to 1000 h. After thermal exposure at 350 °C for 200 h, all four wires still exhibited excellent thermal stabilities. With prolonged exposures at 350 and 400 °C, the alloy wires became unstable. The high-Zr-content Al-0.18Zr-0.1Sc and Al-0.18Zr-0.15Sc alloys exhibited better thermal stabilities after long-term thermal exposures at 350 and 400 °C. This study on the thermal stability of Al-Zr-Sc conductor alloys under extreme conditions provides a valuable reference for industrial applications of thermally resistant Al conductor wires.

In the third part, trace additions of Sn (0.05, 0.15 wt.%) and Sr (0.006, 0.013 wt.%) were introduced into Al–Zr–Sc alloys to investigate their effects on microstructure and mechanical properties. Two-step aging parameters were optimized separately for Sn- and Sr-containing alloys based on the evolution of microhardness and electrical conductivity under various aging conditions. In the Sn15 alloy, two-step aging enhanced microhardness and electrical conductivity to 78.3 HV and 58.3% IACS, compared to 74.2 HV and 57.5% IACS after traditional aging. Similarly, the Sr13 alloy exhibited improved properties with 83.2 HV and 58.0% IACS after two-step aging, versus 78.3 HV and 57.5% IACS using traditional aging. The ultimate tensile strength (UTS) of the Sn15 alloy increased from 205.9 MPa after traditional aging to 215.9 MPa following two-step aging, while the Sr13 alloy showed an increase from 214.9 MPa to 226.5 MPa under the same conditions. These improvements, 0.8% IACS, 5.5 HV, and 10.7 MPa for Sn15; 0.7% IACS, 5.2 HV, and 10.9 MPa for Sr13, are primarily attributed to a higher number density of fine strengthening $Al_3(Sc,Zr)$ precipitates. Early-stage $Al_3(Sc,Zr)$ precipitates were observed in the Sn15 alloy after aging at 300 °C for 4 h. In Sr-containing alloys, enhanced strengthening was also associated with increased dislocation resistance due to the presence of stacking faults. The trace addition of Sn or Sr combined with two-step aging offers a cost-effective strategy for developing the next generation of thermally stable, high-performance conductor alloys.

Table of Contents

List of Tables

List of Figures

List of Abbreviations

wt.%	Weight percent
SEM	Scanning Electron Microscopy
EBSD	Electron Back-Scatter Diffraction
EDS	Energy Dispersive Spectrometry
IPF	Inverse Pole Figure
TEM	Transmission Electron Microscopy
SADP	Selected Area Diffraction Pattern
HV	Hardness Vickers
EC	Electrical Conductivity
IACS	International annealed copper standard
UTS	Ultimate Tensile Strength
El	Elongation

List of Symbols

Al	Aluminum
Si	Silicon
Fe	Iron
Sc	Scandium
Zr	Zirconium
Cu	Copper
Mg	Magnesium
Mn	Manganese
Er	Erbium
Sb	Antimony
Y	Yttrium
MPa	Megapascal
β'	Beta prime precipitate
ºC	Centigrade temperature scale definition
K	Kelvin temperature scale definition
h	Hour
N_V	Number density
t	TEM foil Thickness
D	Diameter/Equivalent Diameter

N	Number of precipitated particles
A	Area
R_A	Area fraction
mm	Millimeter
nm	Nanometer
kV	Kilovolt

Dedication

To my beloved parents, Baoshi Shao and Xiaoping Zhang,

Thank you for your unwavering support, constant encouragement, and endless understanding throughout every step of this journey. Your love and belief in me have been my greatest source of strength.

Acknowledgment

First and foremost, I would like to express my deepest gratitude to my supervisor, Prof. X.-Grant Chen, for welcoming me into his research group and for his unwavering support and guidance throughout my PhD journey. His scientific expertise, thoughtful mentorship, and constant encouragement have been instrumental in shaping both my research capabilities and personal development. I am sincerely grateful for his trust, patience, and commitment, which have motivated me through every stage of this work.

I am also profoundly thankful to my co-supervisor, Prof. Emad Elgallad, and my industrial supervisor, Dr. Alexandre Maltais. Their technical insight, constructive feedback, and continuous support have been invaluable to my research and professional growth. I have learned a great deal under their mentorship, and I deeply appreciate their dedication and generosity with their time and knowledge.

Special thanks go to Prof. Mousa Javidani for his support and valuable input, and to Prof Zhan Zhang for his excellent training in TEM and SEM techniques, as well as his insightful advice on microstructural analysis. I would also like to thank the laboratory staff at CURAL, Zhixing Chen, Félix Tremblay, and Samuel Dessureault, for their technical assistance, which was essential to the success of this work.

I am grateful to all my colleagues at CURAL for their collaboration, insightful discussions, and the supportive atmosphere they helped create. Their friendship and encouragement made this journey more enjoyable and enriching.

To my beloved family, my parents, brother, sister-in-law, and nephew, thank you for your endless love, sacrifice, and unwavering support. You have been the foundation of my perseverance.

To my wife, Yuqing Zhang, your steadfast support, understanding, and belief in me have been a constant source of strength throughout this journey. I am deeply thankful for your presence and partnership in my life.

I would also like to acknowledge the financial and institutional support provided by the Natural Sciences and Engineering Research Council of Canada (NSERC) and Rio Tinto Aluminum through the NSERC Industrial Research Chair in the Metallurgy of Aluminum Transformation at Université du Québec à Chicoutimi (UQAC). Your support made this research possible.

Finally, to all those who contributed to this work in ways both direct and indirect, your support has not gone unnoticed, and I am sincerely grateful.

Chapter 1

Introduction

1.1 Background

1.1.1 Overview of the overhead transmission lines

Since the 1940s, global electric demand has steadily increased, largely driven by population growth, urbanization, and expanding industrial activity. This demand is expected to continue rising due to factors such as the widespread use of electrical appliances, shifts in lifestyle and consumption patterns, and the electrification of transportation. In addition, global industrial energy consumption has increased significantly since 2006, largely driven by technological advancements associated with the Fourth Industrial Revolution [1]. As a result, total energy demand is projected to reach an unprecedented 71,961 ZW by the year 2030 [2]. The global demand for electricity has been steadily increasing over the past decades, and projections indicate that annual electricity consumption will continue to rise significantly in the coming years due to ongoing industrialization, urbanization, and the electrification of transportation and heating systems [3]. Overhead transmission lines are categorized based on distance into short, medium, and long spans, each requiring specific voltage levels ranging from 33 kV to over 500 kV [4]. Among the various conductors used in these systems, All-Aluminum Alloy Conductors (AAAC) are the most commonly applied. They are valued for their lightweight structure and cost-effectiveness. However, depending on the geographic terrain and the required transmission capacity, other types of conductors may be selected. To meet future energy needs and ensure efficient power transmission, it is essential to develop overhead line conductors with improved electrical and mechanical performance [5, 6].

1.1.2 Effect of Zr addition on the properties of aluminum alloy conductors

In addition to its use in the manufacture of Zr-based nanostructures, which are widely employed in numerous technological fields including gas turbines, diesel engines, electrochemical capacitor electrodes, environmental remediation, catalysts and high-temperature fuel cells, Zr is deemed effective in improving the thermal resistance of aluminum alloys [7, 8]. Thermal-resistant aluminium alloy wires designed for overhead line conductors have been developed for continuous operating temperatures ranging from 150 to 230 ^{o}C, which are significantly higher than the maximum operating temperature of Al-Mg-Si alloy wires. The high thermal stability of Al-Zr alloys arises from the precipitation of $L1_2$-Al_3Zr nanoparticles, which are stable at elevated temperatures due to the low diffusivity of Zr in the Al matrix [9]. However, the low strength of Al-Zr alloys generally limits their use as electrical overhead line conductors [10, 11]. Improving the strength of these alloys via the addition of other alloying elements or cold plastic deformation could negatively affect their electrical conductivity [11, 12]. Moreover, the strain hardening resulting from cold plastic deformation is relieved upon heating, thereby degrading the enhanced strength at elevated temperatures.

1.1.3 Effect of the combined additions of Zr and Sc on the properties of aluminum alloy conductors

Microalloying Al-Zr alloys with Sc yields better mechanical properties and thermal resistance [13-15] due to the precipitation of the coherent and thermally stable $L1_2$-$Al_3(Sc,Zr)$ nanoparticles, which possess slow coarsening kinetics and can effectively pin the grain boundaries and dislocations [15, 16]. Several studies on Al-Zr, Al-Sc, and Al-Zr-Sc alloy conductors were reported in the literature. Chao et al. [17] found that the best strength-electrical conductivity combination of Al wires was 160 MPa and 64.0% IACS with a combined addition of 0.12% Sc and 0.04% Zr, compared to 49 MPa and 62.7% IACS, and 110 MPa and 63.6% IACS with separate additions of 0.16% Zr and 0.16% Sc, respectively. A novel Al-0.2Y-0.2Sc conductor alloy was developed, providing a tensile strength of 199–202 MPa and electrical conductivity of 60.8%–61.5% IACS with good thermal stability and high recrystallization resistance owing to the pinning of the dislocations and grain boundaries by $L1_2$- $Al_3(Sc_xY_y)$ precipitates and eutectic Al_3Y-phase particles [18]. Low-cost Al-0.05Sc-0.1Zr-0.2Fe conductor wires were manufactured by continuous rheo-extrusion process, yielding a maximum strength-electrical conductivity combination of 165.7 MPa and 60.3% IACS with thermal resistance satisfying that of the AT1 type alloy wire (Table 1) due to the combined precipitation of $Al_3(Sc,Zr)$ and Al_3Fe precipitates [27]. Wang et al. [28, 29] compared different properties of Al-Ce-Sc, Al-Ce-Zr, and Al-Ce-Sc-Y alloy conductors. They demonstrated that Al_3Sc precipitates enriched with Y atoms in the Al-0.2Ce-0.2Sc-0.1Y alloy can optimize the trade-off between strength and electrical conductivity, and significantly improve the heat resistance and recrystallization behavior, resulting in the combinations of 200 MPa and 61.0% IACS, and 198 MPa and 61.8% IACS after cold drawing and annealing at 200 ºC for 5h, respectively. Tie et al. [19] reported that the strength of rheo-extruded Al-0.12Sc-0.04Zr alloy conductors could reach 217 MPa due to the enhanced dispersion of $Al_3(Sc,Zr)$ precipitates after cold drawing, but with a relatively low electrical conductivity of 53.8% IACS due to electron scattering by dislocations. A high Sc-content Al-0.35Sc-0.2Zr alloy could provide a strength of 210 MPa and electrical conductivity of 60.2% IACS, with only marginal strength reduction after thermal exposure at temperatures of 230 and 400 ºC [10]. Liu et al. [11] reported that a dilute Al-0.06Sc-0.23Zr alloy with optimized processing paths, exhibited a strength of 194 MPa with electrical conductivity of 61% IACS. The highest working temperature of an Al-0.2Sc-0.04Zr conductor with a good combination of strength and electrical conductivity (213 MPa and 61.7% IACS) can reach up to 345 ºC [17].

1.1.4 Effect of Fe addition on the properties of aluminum alloy conductors

With the addition of Fe can slightly reduce electrical conductivity, with no further improvement beyond 0.6% Fe. The addition of Fe forms high-melting Al_3Fe compounds, which clean die walls of adhered aluminum during drawing, improving deformability to smaller diameters. The Al_3Fe phase in the alloy refines after aging due to two main factors: first, large Al_3Fe phases, with higher surface energy, encourage diffusion of solute atoms, transforming coarse particles into stable, smaller spherical phases. Second, minimum surface energy principles drive Fe atoms to migrate from sharp angles to flatter regions [20], promoting a spherical shape for Al_3Fe. This refinement minimizes embrittlement, enhancing tensile strength. Further Sc and Zr precipitation reduces crystal defects, lowering conductive electron scattering.

1.1.5 Effect of Si addition on the properties of aluminum alloy conductors

Consistent with the strong interaction between Si atoms and aluminum vacancies, silicon accelerates: (1) the nucleation and growth of precipitates in the matrix, which increases microhardness at earlier aging stages, and (2) precipitate coarsening at higher temperatures, causing a faster loss of microhardness during overaging [21, 22]. Adding silicon to Al-Zr alloys not only accelerates hardening but also increases hardness. Silicon promotes the growth of Ll_2 phase (Al_3Zr) particles during the decomposition of (Al) in the annealing process. An increase in the Si content leads to an increase of Si content in the solid solution and negatively affects the electrical conductivity of the alloys and increases the hardness. Therefore, the favorable content of Si was equal to 0.25 wt. %–0.50 wt. % [23]. It was also described that Si accelerates the decomposition of the solid solution for alloys with a content of Zr equal to 0.3 wt. %. Studies show that Si suppresses the discontinuous precipitation and enhances the formation of the spherical precipitates with the $L1_2$ structure. Moreover, Si enhances the formation of the $(Al, Si)_3Zr$ phases which have the $D0_{22}$ type structure, different from the Al_3Zr stable phase which has the $D0_{23}$ type structure [24].

1.1.6 Effect of Sn addition on the properties of aluminum alloy conductors

Sn was found to refine precipitates, enhancing microhardness in an Al-Mg-Si 6060 alloy, and to accelerate precipitation kinetics in a commercial Al-Cu 2219 alloy, where Si-Ge precipitates served as nucleation sites for θ″-precipitates [25, 26]. First-principles calculations identified that it also have positive solute-vacancy binding energies in Al at 0 K [27]. It has also been demonstrated that interactions between Sn, In, and vacancies affect the formation of GP-zones in Al-Cu-Sn alloys [28]. Additionally, the Sn- and Ge- peaks observed in the outer shell of the precipitates may suggest nearest-neighbor attractions between Zr and Sn (or Zr and Ge), with these elements diffusing as dimers through a solute-vacancy exchange mechanism [29]. In Al–Cu–Mn alloys, the addition of 0.1 wt.% Sn results in an approximate 43% increase in peak hardness compared to alloys without Sn [30]. This enhancement is primarily attributed to the ability of Sn to refine the precipitation structure and stabilize strengthening phases such as θ″ and θ′, thereby promoting a finer and more uniform distribution of precipitates [31].

1.1.7 Effect of Sr addition on the properties of aluminum alloy conductors

The binary Al-Sr phase diagram shows that Sr has very limited solubility in Al, which is why an alloy with a nominal composition of 0.005 at. % (50 ppm) Sr is used in this study to prevent the primary precipitation of Al_4Sr during solidification and homogenization. The Sc-Sr binary phase diagram reveals no equilibrium intermetallic compounds, suggesting that bonding between these two elements is unfavorable [32]. In contrast, the Si-Sr binary phase diagram indicates the stability of several intermetallic compounds at temperatures relevant to aging aluminum alloys, implying that bonding between Si and Sr is favorable [33]. Al vacancies should be strongly correlated to Sr atoms in the matrix. This strong binding between Sr and Al vacancies in the solid solution can lead to accelerated $Al_3(Sc,Zr)$ precipitate nucleation rate due to the increased diffusivity of Sc, which is reflected in the increase of hardness values [34].

The addition of Sr to aluminum alloys has been shown to enhance mechanical properties through multiple mechanisms [35]. In Al–Mg alloys, Sr contributes to grain refinement [36], solid solution strengthening, and increased dislocation density, all of which contribute to improved mechanical performance [35]. In Al–Si alloys, Sr alters precipitation behavior by modifying the morphology of eutectic Si, resulting in enhanced ductility and strength [37]. For example, in the EN AC 46000 alloy, the addition of approximately 276 ppm of Sr increased the ultimate tensile strength from 300 MPa to 350 MPa and improved elongation from 3% to 6% [38]. Furthermore, the addition of a small amount of Sr to Al–Si–Cu alloys improved strength by generating numerous interacting stacking faults that effectively impeded dislocation motion [39]. These findings demonstrate the potential of Sr additions to enhance mechanical properties through microstructural refinement and precipitation control, suggesting promising applicability in Al–Sc–Zr alloy systems.

1.1.8 The thermal stability of aluminum alloy conductors

With the rapid increase in the global demand for electricity in recent years [40], the current load capacity of long-distance power transmission lines has to be significantly increased. The increased temperature of aluminum conductor wires can lead to recrystallization, which degrades their mechanical properties and deteriorates the overall performance and reliability of transmission lines [41-43]. Thermal stability refers to a material's ability to maintain its properties and resist degradation upon a prolonged exposure at elevated temperatures [44]. The thermal stability of aluminum alloys can be divided into three categories based on the service temperature. Stability at moderate temperatures typically refers to conditions up to 100 °C. For example, Al-Cu-Mg-Ag alloys with excellent creep properties are used for the fuselage of supersonic transport aircrafts for the temperature range of 70 to 85 °C [45]. The medium temperature range, which necessitates thermal stability, encompasses temperatures up to 200 °C. This includes impellers used in generators and turbochargers operating within a service temperature range of 150 to 180 °C. For example, Al-Cu-Mg-Fe-Ni alloys exhibit excellent heat resistances under such conditions [46]. On the other hand, it is challenging to achieve thermal stability of aluminum alloys for high-temperature exposures up to 400 °C [18, 47-49].

1.2 Problem statement

Due to the growing global demand for electricity, aluminum has increasingly replaced copper in long-distance power transmission lines, owing to its lower weight and cost advantages [50, 51]. Among aluminum alloys, the Al–Mg–Si 6xxx series is most commonly used for the production of All-Aluminum Alloy Conductors (AAACs), as it provides a favorable combination of mechanical strength and electrical conductivity, typically ranging from 52.6 to 59.0 % IACS [52]. However, the limited thermal resistance of Al–Mg–Si alloys remains a major constraint. These alloys can generally withstand continuous service temperatures only between 90 and 100 °C [53, 54]. This thermal limitation reduces their current-carrying capacity, as higher electrical loads result in increased conductor temperature, potentially compromising performance and reliability.

To address this limitation, it is necessary to develop thermally resistant aluminum alloy conductors capable of retaining their mechanical and electrical properties under elevated temperatures. One promising strategy is the addition of transition elements such as Sc and Zr, which promote the formation of coherent and thermally stable $Al_3(Sc,Zr)$ precipitates [11, 21, 55-57]. These precipitates can refine the microstructure, inhibit recrystallization, and improve strength retention during high-temperature exposure [58, 59].

This study aims to investigate the effects of Sc, Sn and Sr additions on the microstructure, precipitation behavior, and mechanical properties of Al-Zr-based alloys. The goal is to enhance the mechanical and electrical properties, as well as thermal resistance of these alloys and support the development of new generation of high performance aluminum electrical conductors with improved high-temperature performance suited to modern power transmission demands.

1.3 Objectives

The main objective of this project is to enhance the mechanical properties, electrical conductivity, and thermal resistance of aluminum alloys through the optimization of processing parameters, including heat treatments and microalloying with Sc, Sn and Sr. The research is structured around three main topics, each with the following specific sub-objectives:

1. Development of thermal-resistant Al-Zr based conductor alloys via microalloying with Sc and manipulating thermomechanical processing

I. Develop Al–Zr alloys with ⩽ 0.10 wt.% Sc micro alloying using two processing routes: cold drawing before and after aging.

II. Evaluate mechanical properties, electrical conductivity, and thermal resistance based on IEC standards.

III. Study the strengthening mechanisms by analyzing precipitate formation and grain structure evolution.

2. Thermal stability of Al-Zr-Sc conductor alloys during long-term elevated-temperature

I. Investigated the effects of varying Sc and Zr contents on the mechanical properties and electrical conductivity of Al–Zr–Sc alloy wires.

II. Evaluated the thermal stability of the alloys through long-term thermal exposure at 310, 350, and 400 °C for up to 1000 h.

III. Characterized the microstructural evolution under extreme high-temperature thermal exposure conditions.

3. Enhancing strength and electrical conductivity in thermal-resistant Al -Zr-Sc alloys via Sn and Sr microalloying with two-step heat treatment

I. Investigated the effects of trace Sn and Sr additions on the microstructure and mechanical properties of Al–Zr–Sc alloys.

II. Optimized two-step aging parameters for Sn- and Sr-containing alloys based on the evolution of microhardness and electrical conductivity.

III. Evaluated the improvements in tensile strength, conductivity, and hardness achieved by two-step aging compared to traditional aging.

IV. Analyzed the strengthening mechanisms associated with fine $Al_3(Sc,Zr)$ precipitate formation and stacking faults introduced by Sn and Sr additions.

1.4 Originality statement

This project focuses on the development of thermally resistant aluminum conductor alloys through microalloying with Sc, aiming to enhance mechanical strength, electrical conductivity, and high-temperature performance. The research strategy combines trace alloying additions (Sn and Sr) with optimized thermomechanical processing and heat treatments to address the growing performance demands in modern power transmission systems.

The first part of the study investigates the effects of Sc addition at levels up to 0.10 wt.% and two distinct thermomechanical processing routes. In these routes, cold wire drawing was applied either before or after the aging treatment. The mechanical, electrical, and thermal-resistant properties of the developed alloys were systematically evaluated based on IEC standards. Microstructural evolution, including the formation of $Al_3(Sc,Zr)$ precipitates and grain structure changes, was examined in detail. This study presents the first systematically study to directly compare the two thermomechanical processing sequences in this alloy system, demonstrating comparable performance and offering practical flexibility for industrial manufacturing. The excellent combinations of mechanical, electrical, and thermal-resistant properties made the developed alloys promising candidate materials for four standard grades of thermalresistant aluminium conductors, while taking advantage of an affordable material cost.

The second part systematically evaluates the thermal resistance of Al–Zr–Sc conductor alloys under high-temperature conditions, representing the first comprehensive study of its kind. Alloys with varying Zr and Sc contents were subjected to long-term thermal exposures at 310, 350, and 400 °C for up to 1000 hours. Their mechanical properties, electrical conductivity, and microstructural evolution were assessed using SEM, TEM, and EBSD. While changes in Sc and Zr levels had only a minor effect on peak strength, higher Zr content significantly improved the alloys' thermal stability during prolonged exposure. This original investigation fills a critical gap in the literature and provides valuable insights for the design of thermally resistant aluminum conductors intended for extreme service environments.

The third part explores the rarely reported effects of trace additions of Sn and Sr on the microstructure and mechanical properties of Al–Zr–Sc alloys. A two-step aging process was optimized for each system based on the evolution of microhardness and electrical conductivity. Compared to traditional aging, the two-step aging led to noticeable improvements in hardness, tensile strength, and conductivity. These enhancements were attributed to a higher number density of $Al_3(Sc,Zr)$ precipitates in Sn-containing alloys and increased dislocation resistance caused by stacking faults in Sr-containing alloys. This work introduces a novel and cost-effective strengthening strategy through microalloying and heat treatment optimization, addressing a significant gap in the literature regarding Sn and Sr additions in Al–Sc–Zr systems.

1.5 Thesis outline

The current PhD thesis comprises five chapters:

Chapter 1 provides a brief introduction to the current project, beginning with an overview of the overhead transmition lines, effect of several elements on the properties of aluminum conductor, and the thermal stability of aluminum conductor. The chapter concludes with the definition of the problem statement, research objectives, and the originality of this study.

Chapter 2 consistes of a published paper "Development of thermal-resistant Al-Zr based conductor alloys via microalloying with Sc and manipulating thermomechanical processing" in *Journal of Materials Research and Technology* (2023). This chapter focused on developing thermally resistant Al–Zr–Sc conductor alloys using low levels of Sc ($\leqslant$ 0.10 wt.%) and two thermomechanical processing routes. Mechanical properties, electrical conductivity, and thermal resistance were evaluated according to IEC standards. The microstructure and precipitation behavior were characterized to understand the strengthening mechanisms associated with fine $Al_3(Sc,Zr)$ precipitate.

In Chapter 3, another published paper "Thermal stability of Al-Zr-Sc conductor alloys during long-term elevated-temperature exposures" in the *Journal of Materials Research and Technology* (2025) is presented. This chapter systematically evaluated the long-term thermal stability of Al–Zr–Sc alloys with varying Sc and Zr contents. Alloys were subjected to thermal exposures at 310, 350, and 400 °C for up to 1000 hours. The influence of composition on strength retention, precipitate coarsening, and microstructural evolution was investigated.

Chapter 4 presents the manuscript titled "Enhancing strength and electrical conductivity in thermal-resistant Al-Zr-Sc alloys via Sn and Sr microalloying with two-step heat treatment." This manuscript is the third part of my Ph.D. project and is also intented to be published in a scientific journal. The study examined the effects of trace Sn and Sr additions on the properties of Al–Sc–Zr alloys, using a two-step aging process optimized for each element. Improvements in strength and conductivity were correlated with the precipitation of $Al_3(Sc,Zr)$ and the presence of stacking faults. The study demonstrated a cost-effective method for further enhancing alloy performance through microalloying and aging control.

Finally, Chapter 5 presents the general conclusions of this research, summarizing the key findings of this project. It also includes recommendations for future work, highlighting potential areas for further optimization and exploration. Subsequent to the primary chapters, a list of publications is provided.

References

[1] Omer AM. Energy, environment and sustainable development. Renewable and sustainable energy reviews 2008; 12(9):2265-2300.

[2] Sahoo T, Guharoy A. Energy cost savings with centrifugal pumps. World Pumps 2009; 2009(510):35-37.

[3] Mai TT, Jadun P, Logan JS, McMillan CA, Muratori M, Steinberg DC et al., Electrification futures study: Scenarios of electric technology adoption and power consumption for the United States, National Renewable Energy Lab.(NREL), Golden, CO (United States), 2018.

[4] Maw AA, Mawlamyine M. Performance Analysis of Overhead Transmission Line Design. International Journal of Science and Engineering Applications 2019; 8(08):307-311.

[5] Dève H. Importance of materials in composite conductors. Electric Power Systems Research 2019; 172:290-295.

[6] Hadzimuratovic S, Fickert L, Impact of gradually replacing old transmission lines with advanced composite conductors, 2018 IEEE PES Innovative Smart Grid Technologies Conference Europe (ISGT-Europe), IEEE, 2018, pp. 1-5.

[7] Li H, Bin J, Liu J, Gao Z, Lu X. Precipitation evolution and coarsening resistance at 400 C of Al microalloyed with Zr and Er. Scripta Materialia 2012; 67(1):73-76.

[8] Muthaiah VS, Mula S. Effect of zirconium on thermal stability of nanocrystalline aluminium alloy prepared by mechanical alloying. Journal of Alloys and Compounds 2016; 688:571-580.

[9] Knipling KE, Dunand DC, Seidman DN. Precipitation evolution in Al–Zr and Al–Zr–Ti alloys during isothermal aging at 375–425 C. Acta Materialia 2008; 56(1):114-127.

[10] Guan R, Shen Y, Zhao Z, Wang X. A high-strength, ductile Al-0.35Sc-0.2Zr alloy with good electrical conductivity strengthened by coherent nanosized-precipitates. Journal of Materials Science & Technology 2017; 33(3):215-223.

[11] Li Liu J-TJ, Bo Zhang, Wen-Zhu Shao, Liang Zhen. Enhancement of strength and electrical conductivity for a dilute Al-Sc-Zr alloy via heat treatments and cold drawing. J. Mater. Sci. Technol. 2019; 35(6):962-971.

[12] Khangholi SN, Javidani M, Maltais A, Chen XG. Review on recent progress in Al–Mg–Si 6xxx conductor alloys. Journal of Materials Research 2022; 37(3):670-691.

[13] Fuller CB, Seidman DN, Dunand DC. Mechanical properties of Al (Sc, Zr) alloys at ambient and elevated temperatures. Acta materialia 2003; 51(16):4803-4814.

[14] Knipling KE, Karnesky RA, Lee CP, Dunand DC, Seidman DN. Precipitation evolution in Al–0.1 Sc, Al–0.1 Zr and Al–0.1 Sc–0.1 Zr (at.%) alloys during isochronal aging. Acta Materialia 2010; 58(15):5184-5195.

[15] Knipling KE, Seidman DN, Dunand DC. Ambient-and high-temperature mechanical properties of isochronally aged Al–0.06 Sc, Al–0.06 Zr and Al–0.06 Sc–0.06 Zr (at.%) alloys. Acta Materialia 2011; 59(3):943-954.

[16] Zhou W, Cai B, Li W-J, Liu Z-X, Yang S. Heat-resistant Al–0.2 Sc–0.04 Zr electrical conductor. Materials Science and Engineering: A 2012; 552:353-358.

[17] Chao R-z, Guan X-h, Guan R-g, Di T, Chao L, Xiang W et al. Effect of Zr and Sc on mechanical properties and electrical conductivities of Al wires. Transactions of Nonferrous Metals Society of China 2014; 24(10):3164-3169.

[18] Pozdniakov AV, Barkov RY. Microstructure and mechanical properties of novel Al-Y-Sc alloys with high thermal stability and electrical conductivity. Journal of Materials Science & Technology 2020; 36:1-6.

[19] Tie D, Wang Y, Wang X, Guan R, Yan L, Zhang J et al. Microstructure Evolution and Properties Tailoring of Rheo-Extruded Al-Sc-Zr-Fe Conductor via Thermo-Mechanical Treatment. Materials 2020; 13(4):845.

[20] Cubero-Sesin JM, In H, Arita M, Iwaoka H, Horita Z. High-pressure torsion for fabrication of high-strength and high-electrical conductivity Al micro-wires. Journal of Materials Science 2014; 49(19):6550-6557.

[21] Booth-Morrison C, Mao Z, Diaz M, Dunand D, Wolverton C, Seidman D. Role of silicon in accelerating the nucleation of Al3 (Sc, Zr) precipitates in dilute Al–Sc–Zr alloys. Acta Materialia 2012; 60(12):4740-4752.

[22] Vo NQ, Seidman DN, Dunand DC. Effect of Si micro-addition on creep resistance of a dilute Al-Sc-Zr-Er alloy. Materials Science and Engineering: A 2018; 734:27-33.

[23] Morozova A, Mogucheva A, Bukin D, Lukianova O, Korotkova N, Belov N et al. Effect of Si and Zr on the microstructure and properties of Al-Fe-Si-Zr alloys. Metals 2017; 7(11):495.

[24] Sato T, Kamio A, Lorimer GW, Effects of Si and Ti additions on the nucleation and phase stability of the L12-type Al3Zr phase in Al-Zr alloys, Materials Science Forum, Trans Tech Publ, 1996, pp. 895-900.

[25] Maksimovic V, Zec S, Radmilovic V, Jovanovic MT. The effect of microalloying with silicon and germanium on microstructure and hardness of a commercial aluminium alloy. JOURNAL-SERBIAN CHEMICAL SOCIETY 2003; 68(11):893-902.

[26] Mørtsell EA, Marioara CD, Andersen SJ, Røyset J, Reiso O, Holmestad R. Effects of germanium, copper, and silver substitutions on hardness and microstructure in lean Al-Mg-Si alloys. Metallurgical and Materials Transactions A 2015; 46:4369-4379.

[27] Wolverton C. Solute–vacancy binding in aluminum. Acta Materialia 2007; 55(17):5867-5872.

[28] Kimura H, Hasiguti R. Interaction of vacancies with Sn atoms and the rate of GP zone formation in an Al-Cu-Sn alloy. Acta Metallurgica 1961; 9(12):1076-1078.

[29] Okle P, Lin JD, Zhu T, Dunand DC, Seidman DN. Effect of micro-additions of Ge, In or Sn on precipitation in dilute Al-Sc-Zr alloys. Materials Science and Engineering: A 2019; 739:427-436.

[30] Akopyan T, Letyagin N, Belov N, Fortuna A, Nguen X. The role of Sn trace addition in the precipitation behavior and strengthening of the wrought Al–Cu–Mn-based alloy. Journal of Materials Science 2023; 58(19):8210-8229.

[31] Akopyan TK, Belov NA, Letyagin NV. Effect of trace addition of Sn on the precipitation hardening in Al-Si-Cu eutectic alloy. Jom 2019; 71:1768-1775.

[32] Okamoto H. Supplemental Literature Review of Binary Phase Diagrams: Cd-Se, Cu-Hg, Cu-Ho, Eu-Mg, H-Sr, Hf-Si, La-Mn, Mn-Nd, Nb-Y, Ni-Y, Pb-Se, and Sc-Sr. Journal of phase equilibria and diffusion 2013; 34(5):430-436.

[33] Palenzona A, Pani M. The phase diagram of the Sr–Si system. Journal of alloys and compounds 2004; 373(1-2):214-219.

[34] Lin JD, Seidman DN, Dunand DC. Improving coarsening resistance of dilute Al-Sc-Zr-Si alloys with Sr or Zn additions. Materials Science and Engineering: A 2019; 754:447-456.

[35] Yang Z, Dong Y, Li W, Liu X, Feng H. Effect of Sr on Microstructure and Strengthening Mechanism of Al-4.6 Mg Alloy. Materials 2023; 16(15):5450.

[36] Che H, Jiang X, Qiao N, Liu X. Effects of Er/Sr/Cu additions on the microstructure and mechanical properties of Al-Mg alloy during hot extrusion. Journal of Alloys and Compounds 2017; 708:662-670.

[37] Liu T, Morales S, Karkkainen M, Nastac L, Arvikar V, Levin I et al. The combined effects of Sr additions and heat treatment on the microstructure and mechanical properties of high pressure die cast A383 alloy. Materials Science and Engineering: A 2019; 756:373-380.

[38] Ma S, Sun Y, Wang H, Lü X, Qian M, Ma Y et al. Effect of a minor Sr modifier on the microstructures and mechanical properties of 7075 T6 al alloys. Metals 2017; 7(1):13.

[39] Shi Z, He R, Chen Y, Yan H, Song H, Luo C et al. Microstructural evolution and strengthening mechanisms of a novel Al–11Si–3Cu alloy microalloyed with minor contents of Sr and Sc. Materials Science and Engineering: A 2022; 853.

[40] Andrae AS, Edler T. On global electricity usage of communication technology: trends to 2030. Challenges 2015; 6(1):117-157.

[41] Mao Q, Zhang Y, Guo Y, Zhao Y. Enhanced electrical conductivity and mechanical properties in thermally stable fine-grained copper wire. Communications Materials 2021; 2(1):46.

[42] Algendy AY, Liu K, Rometsch P, Parson N, Chen XG. Evolution of discontinuous/continuous Al3(Sc,Zr) precipitation in Al-Mg-Mn 5083 alloy during

thermomechanical process and its impact on tensile properties. Materials Characterization 2022; 192.

[43] Shao Q, Elgallad EM, Maltais A, Chen XG. Development of thermal-resistant Al–Zr based conductor alloys via microalloying with Sc and manipulating thermomechanical processing. Journal of Materials Research and Technology 2023; 25:7528-7545.

[44] Matthews S. Thermal stability of solid solution strengthened high performance alloys. Superalloys: Metallurgy and manufacture 1976:215-226.

[45] Polmear I, Pons G, Barbaux Y, Octor H, Sanchez C, Morton A et al. After concorde: evaluation of creep resistant Al–Cu–Mg–Ag alloys. Materials science and technology 1999; 15(8):861-868.

[46] Tanaka T, Kamitakahara Y. Highly heat-resistant aluminum alloy “KS2000”. KOBELCO Technol. Rev 2017; 35:28-33.

[47] Rakhmonov J, Liu K, Pan L, Breton F, Chen X-G. Enhanced mechanical properties of high-temperature-resistant Al–Cu cast alloy by microalloying with Mg. Journal of Alloys and Compounds 2020; 827:154305.

[48] Shurkin P, Letyagin N, Yakushkova A, Samoshina M, Ozherelkov DY, Akopyan T. Remarkable thermal stability of the Al-Ca-Ni-Mn alloy manufactured by laser-powder bed fusion. Materials Letters 2021; 285:129074.

[49] Su X, Lei Y, Chen Y, Qu H, Qi Z, Zheng G et al. Precipitating thermally reinforcement phase in aluminum alloys for enhanced strength at 400° C. Journal of Materials Science & Technology 2024; 172:71-82.

[50] Murashkin MY, Sabirov I, Sauvage X, Valiev R. Nanostructured Al and Cu alloys with superior strength and electrical conductivity. Journal of materials science 2016; 51(1):33-49.

[51] Blackburn JL. Symmetrical components for power systems engineering. CRC press2017.

[52] 8134-1997 JT. Al-Mg-Si alloy wire for overhead line conductor.

[53] Yuan W, Liang Z, Zhang C, Wei L. Effects of La addition on the mechanical properties and thermal-resistant properties of Al–Mg–Si–Zr alloys based on AA 6201. Materials & Design 2012; 34:788-792.

[54] Yuan W, Liang Z. Effect of Zr addition on properties of Al–Mg–Si aluminum alloy used for all aluminum alloy conductor. Materials & Design 2011; 32(8-9):4195-4200.

[55] Dorin T, Babaniaris S, Jiang L, Cassel A, Race CP, Eggeman A et al. Stability and stoichiometry of L12 Al3 (Sc, Zr) dispersoids in Al-(Si)-Sc-Zr alloys. Acta Materialia 2021; 216:117117.

[56] Wang Y, Liu H, Ma X, Wu R, Sun J, Hou L et al. Effects of Sc and Zr on microstructure and properties of 1420 aluminum alloy. Materials Characterization 2019; 154:241-247.

[57] Zhao J, Lee L, Chang K, Hung F. A novel two-stage heat treatment with medium-temperature aging influence on microstructure, Al3 (Sc, Zr) nanoprecipitation, and

application properties, enhancing selective laser melting of Al–Mg–Sc–Zr alloy. Nanomaterials 2022; 12(12):2078.

[58] Deng Y, Xu G, Yin Z, Lei X, Huang J. Effects of Sc and Zr microalloying additions on the recrystallization texture and mechanism of Al–Zn–Mg alloys. Journal of Alloys and Compounds 2013; 580:412-426.

[59] Lei Z, Wen S, Huang H, Wei W, Nie Z. Grain Refinement of Aluminum and Aluminum Alloys by Sc and Zr. Metals 2023; 13(4).

Chapter 2

Development of thermal-resistant Al-Zr based conductor alloys via microalloying with Sc and manipulating thermomechanical processing

(This article is published in: Journal of Materials Research and Technology Volume 25, July–August 2023, Pages 7528-7545)

Abstract

Thermal-resistant Al-Zr based conductor alloys were developed using microalloying with a low level of Sc (≤ 0.10 wt.%) and two thermomechanical processing routes, in which the cold wire drawing was conducted before and after the aging treatment. The mechanical properties, electrical conductivities, and thermal-resistant properties of several alloys were investigated and evaluated according to the IEC standard of thermal-resistant aluminium conductors. The evolutions of the precipitates and grain structure during processing were also studied. The microalloying with Sc resulted in the precipitation of a large number of fine $Al_3(Sc,Zr)$ precipitates, which provided substantially high strength of 188-209 MPa, representing 73-88% improvement compared to the Sc-free base alloy, while maintaining excellent electrical conductivity of 57.4-59.9% IACS. Moreover, the Sc-containing alloys exhibited outstanding thermal-resistant properties, where the maximum strength reduction was limited to ≤ 6.0% after thermal exposures at 310 and 400 ºC. The best combinations of mechanical properties and electrical conductivities of the Sc-containing alloys were obtained after aging at 350 ºC for 48 h, following solutionizing at 600 ºC for 8 h. Both processing routes yielded comparable precipitation strengthening and

strain hardening, and consequently comparable mechanical and electrical properties, where the maximum differences in the strength and electrical conductivity between both routes were 12 MPa and 1.4% IACS, respectively. The excellent combinations of mechanical, electrical, and thermal-resistant properties made the developed alloys promising candidate materials for four standard grades of thermal-resistant aluminium conductors, while taking advantage of an affordable material cost and using conventional thermomechanical processes.

Keywords: Thermal-resistant Al conductor alloys, Sc microalloying, mechanical properties, electrical conductivity, thermal-resistant properties.

2.1 Introduction

Considering the rising global demand for electricity, aluminum conductors are increasingly used as substitutes for copper conductors in long-distance overhead lines. This shift is due to the lighter weight and the lower cost of aluminum conductors [1, 2]. All-Aluminium Alloy Conductors (AAAC) are extensively used in overhead distribution and transmission lines because of their higher strength to weight ratio and better corrosion resistance compared to Aluminum Conductors Steel Reinforced (ACSR) Cables [3-5]. Al-Mg-Si 6xxx alloys are the predominant aluminum alloys utilized in the production of AAACs. These alloys can be categorised in two types: i) typical AA6021 alloys with high strength ranging from 295-315 MPa, but with relatively low electrical conductivity of 52.5% IACS; and ii) typical AA6101 alloys with moderate strength of 240 MPa, but with a high electrical conductivity of 59.0% IACS [6]. However, these alloys have poor thermal resistance due to precipitate coarsening (overaging) that occurs at elevated temperatures, which restricts their operating temperature to below 100 ºC [3, 7] and consequently their usage and current-carrying capability.

In addition to its use in the manufacture of Zr-based nanostructures, which are widely employed in numerous technological fields including gas turbines, diesel engines, electrochemical capacitor electrodes, environmental remediation, catalysts and high-temperature fuel cells [8-12], Zr is deemed effective in improving the thermal resistance of aluminum alloys [13-16]. Thermal-resistant aluminium alloy wires designed for overhead line conductors have been developed for continuous operating temperatures ranging from 150 to 230 ºC, which are significantly higher than the maximum operating temperature of Al-Mg-Si alloy wires. According to the IEC 62004 international standard [17], thermal-resistant Al-Zr based alloy wires are classified into four grades, namely AT1, AT2, AT3 and AT4, based on their strength, electrical conductivity, and thermal resistant property, as summarized in Table 2-1. The high thermal stability of Al-Zr alloys arises from the precipitation of $L1_2$-Al_3Zr nanoparticles, which are stable at elevated temperatures due to the low diffusivity of Zr in the Al matrix [13-16]. However, the low strength of Al-Zr alloys generally limits their use as electrical overhead line conductors [18, 19]. Improving the strength of these alloys via the addition of other alloying elements or cold plastic deformation could negatively affect their electrical conductivity [19, 20]. Moreover, the strain hardening resulting from cold plastic deformation is relieved upon heating, thereby degrading the enhanced strength at elevated temperatures. Microalloying Al-Zr alloys with Sc yields better mechanical properties and thermal resistance [21-23] due to the precipitation of the coherent and thermally stable $L1_2$-$Al_3(Sc,Zr)$ nanoparticles, which possess slow coarsening kinetics and can effectively pin the grain boundaries and dislocations [23, 24].

Table 2-1 Overall properties of thermal-resistant aluminium alloy wires (IEC 62004 standard [17]).

Category	Electrical conductivity (% IACS)	Tensile strength[a] (MPa)	Elongation[a] (%)	Thermal-resistant temperature[b] (°C)	
				1 h heating	400 h heating
AT1	60.0	159	2.0	230	180
AT2	55.0	225	2.0	230	180
AT3	60.0	159	2.0	280	240
AT4	58.0	159	2.0	400	310

[a] Tensile strength and elongation are based on 4.0 – 4.5 mm diameter wires.

[b] After thermal exposure, a minimum strength of 90 % of the initial tensile strength is required.

Several studies on Al-Zr, Al-Sc, and Al-Zr-Sc alloy conductors were reported in the literature. Chao et al. [25] found that the best strength-electrical conductivity combination of Al wires was 160 MPa and 64.0% IACS with a combined addition of 0.12% Sc and 0.04% Zr, compared to 49 MPa and 62.7% IACS, and 110 MPa and 63.6% IACS with separate additions of 0.16% Zr and 0.16% Sc, respectively. A novel Al-0.2Y-0.2Sc conductor alloy was developed, providing a tensile strength of 199–202 MPa and electrical conductivity of 60.8%–61.5% IACS with good thermal stability and high recrystallization resistance owing to the pinning of the dislocations and grain boundaries by $L1_2$- $Al_3(Sc_x,Y_y)$ precipitates and eutectic Al_3Y-phase particles [26]. Low-cost Al-0.05Sc-0.1Zr-0.2Fe conductor wires were manufactured by continuous rheo-extrusion process, yielding a maximum strength-electrical conductivity combination of 165.7 MPa and 60.3% IACS with thermal resistance satisfying that of the AT1 type alloy wire (Table 2-1) due to the combined precipitation of $Al_3(Sc,Zr)$ and Al_3Fe precipitates [27]. Wang et al. [28, 29] compared different properties of Al-Ce-Sc, Al-Ce-Zr, and Al-Ce-Sc-Y alloy conductors. They demonstrated that Al3Sc precipitates enriched with Y atoms in the Al-0.2Ce-0.2Sc-0.1Y alloy can optimize the trade-off between strength and electrical conductivity, and significantly improve the heat resistance and recrystallization behavior, resulting in the combinations of 200 MPa and 61.0% IACS, and 198 MPa and 61.8% IACS after cold drawing and annealing at 200 ºC for 5h, respectively. Tie et al. [30] reported that the strength of rheo-extruded Al-0.12Sc-0.04Zr alloy conductors could reach 217 MPa due to the enhanced dispersion of $Al_3(Sc,Zr)$ precipitates after cold drawing, but with a relatively low electrical conductivity of 53.8% IACS due to electron scattering by dislocations. A high Sc-content Al-0.35Sc-0.2Zr alloy could provide a strength of 210 MPa and electrical conductivity of 60.2% IACS, with only marginal strength reduction after thermal exposure at temperatures of 230 and 400 ºC [18]. Liu et al. [19] reported that a dilute Al-0.06Sc-0.23Zr alloy with optimized processing paths, exhibited a strength of 194 MPa with electrical conductivity of 61% IACS. The highest working temperature of an Al-0.2Sc-0.04Zr conductor with a good combination of strength and electrical conductivity (213 MPa and 61.7% IACS) can reach up to 345 ºC [24].

Although Al-Zr-Sc alloys have shown promising characteristics in the fabrication of high thermal-resistant aluminium conductors, the influences of Sc and the thermomechanical processing on the overall properties of the materials, including strength, electrical conductivity and thermal-resistance, have not been systematically assessed in relation to standard specifications of these conductors. The present study is undertaken to develop a series of Al-Zr-Sc alloys that could yield various combinations of mechanical, electrical and thermal-resistant properties, to satisfy the requirements of AT1, AT2, AT3 and AT4 grades of thermal resistant aluminium conductors according to the IEC 62004 standard [17]. The approach primarily focused on the cost-effectiveness by incorporating a low level of Sc addition (≤ 0.10 wt.%) and conventional thermomechanical processes. The electrical conductivity, mechanical and thermal resistant properties of several alloy wires were investigated with two thermomechanical processing routes. The evolution of the precipitate microstructure and grain structure during thermomechanical processing was investigated using transmission electron microscopy (TEM) and electron backscatter diffraction (EBSD) techniques.

2.2 Experimental procedure

2.2.1 Alloys and casting

Four experimental alloys were prepared with nominal and actual chemical compositions listed in Table 2-2. The actual chemical compositions of the alloys were determined by optical emission spectroscopy. The A alloy is the reference Sc-free Al-Zr alloy. The other three B, C, and D alloys contained both Zr and Sc, focusing on a low Sc level, namely up to a maximum of 0.10 wt.%, to reduce the raw material cost of the alloys. With this Sc level, a Zr level of 0.10 wt.% was targeted for these alloys to obtain $Al_3(Sc,Zr)$ precipitates with better coarsening resistance [31, 32], while hindering the formation of Zr-containing primary intermetallic particles. The Si and Fe levels were varied in the B, C, and D alloys to study the effects of these elements on the electrical conductivity, as undesirable impurities, and on the precipitation of $Al_3(Sc,Zr)$ precipitates, as catalysts [33, 34]. Accordingly, both elements were maintained in alloy D at their original levels in the commercially pure Al. On the other hand, Fe was increased to 0.30 wt.% in alloy C, while both Si and Fe were increased to 0.25 and 0.30 wt.%, respectively, in alloy B; such levels could improve the precipitation of $Al_3(Sc,Zr)$ precipitates [33-35] with no significant increase of Fe intermetallic particles.

Table 2-2 Nominal and actual chemical compositions of the experimental alloys (wt.%).

Alloy	Nominal composition	Actual composition				
		Si	Fe	Zr	Sc	Al
A	Al-0.25Si-0.30Fe-0.15Zr	0.26	0.27	0.14	--	Bal.
B	Al-0.25Si-0.30Fe-0.10Zr-0.10Sc	0.24	0.28	0.11	0.07	Bal.
C	Al-0.05Si-0.30Fe-0.10Zr-0.10Sc	0.03	0.27	0.08	0.07	Bal.
D	Al-0.05Si-0.07Fe-0.10Zr-0.10Sc	0.07	0.07	0.12	0.09	Bal.

The alloys were prepared using commercially pure Al (99.8 wt.%) with Al-50%Si, Al-25%Fe, Al-2%Sc, and Al-15%Zr master alloys. For each alloy composition, approximately 5 kg of materials were melted in a SiC crucible using an electrical resistance furnace. The master alloys were added at 750 ºC, *i.e.*, above the liquidus temperature of the Al-0.2%Zr alloys (720 ºC). The molten metal was degassed for 15 min using pure dry argon injected into the melt by means of a rotary graphite impeller rotating at 150 rpm. The melts were cast into a Y-shaped permanent steel mold preheated to 400 °C to obtain rectangular ingots with dimensions of 30 × 40 × 80 mm.

2.2.2 Thermomechanical processing

The thermomechanical processing of the cast ingots involved hot rolling, heat treatments, and cold wire drawing. Two processing routes referred to as R1 and R2 were applied in this study, as shown in Figure 2-1. Hot rolling was carried out on a lab-scale rolling mill with multiple passes at a temperature of 550 °C. The hot rolling was initially applied to a 26.5 mm-thick ingot to eventually obtain an 8 mm-thick strip, yielding a reduction ratio of ~70%. The strips were then cut in the rolling direction and machined into 6.7 mm square bars for subsequent processing.

Both solution and aging treatments were conducted in a programmable air circulating electric furnace. All alloys were solutionized at 600 ºC for 8 h. The aging treatment was conducted at 350 ºC for 48 h for the Sc-containing B, C, and D alloys and at 400 ºC for 48 h for the base A alloy. These aging treatments were specifically selected after evaluating the age hardening behaviors of the alloys at 350 - 450 ºC with different aging times ranging from 6 to 96 h before wire drawing was performed either in route R1 or route R2. For all aging treatments, the heating ramp rate was 100 °C/h and the aging was followed by room-temperature water quenching. Cold wire drawing was performed on a lab-scale wire drawing mill to draw the 6.7 mm square bars into 4.3 mm diameter wires (~68% reduction ratio). The wires processed with route R1 were annealed at 350 ºC for 5 h to adjust the electrical conductivity that could be decreased by wire drawing.

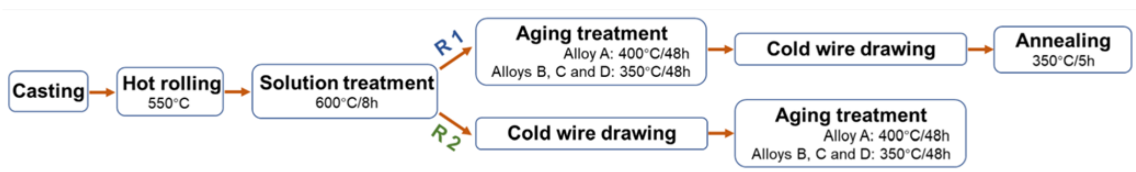

Figure 2-1 Thermomechanical processing routes used to produce aluminum alloy wires.

2.2.3 Mechanical, electrical, and thermal-resistant properties

Vickers hardness was measured using an NG-1000 CCD microhardness tester with a load of 25 g and dwell time of 15 s. The electrical conductivity (EC) was measured in terms of percentage of the international annealed copper standard (% IACS) using a Sigmascope SMP10 electrical conductivity measurement instrument based on the eddy current method. The microhardness and EC measurements were performed at ambient temperature on the polished cross sections of 4.3 mm diameter wire samples mounted in bakelite. For both microhardness and EC, at least fifteen measurements were taken and averaged per condition.

The tensile properties of all 4.3 mm diameter wires with an original gauge length of 250 mm were measured using an Instron 8801 servo-hydraulic unit with a strain rate of 25 mm/min. Three wires were tested for each condition, and the average values of ultimate tensile strength (UTS) and percentage elongation (El) were calculated.

To evaluate the thermal-resistant property according to the IEC 62004 standard [17], 4.3 mm diameter wires were subjected to two thermal exposures at 400 ºC for 1 h and 310 ºC for 400 h, respectively. The UTSs of the thermally exposed wires were determined, and then compared with those without thermal exposure. The thermal-resistant property was further examined based on the decrease of the microhardness of the wires after thermal exposure at 310 ºC with prolonged time up to 1000 h.

2.2.4 Microstructure observations

The microstructures of as-cast samples were examined using a scanning electron microscope (SEM, Jeol JSM-6480LV) equipped with an energy dispersive X-ray spectrometer (EDS). The nanosize Al_3Zr and $Al_3(Zr,Sc)$ precipitates were observed in the dark-field mode using a transmission electron microscope (TEM, Jeol JEM-2100) operated at 200 kV. The TEM samples were sliced from the cross sections of 4.3 mm diameter wires and electropolished to perforation using a twinjet electropolisher in a solution of nitric acid and methanol with a volume ratio of 1:2 at –25 ºC and a potential difference of 12 V. The precipitate characteristics, namely the number density and average diameter, were determined based on the image analysis of TEM images.

The deformed grain structure was investigated in different stages of thermomechanical processing using EBSD analysis in the SEM. The EBSD samples were sectioned parallel to the rolling or drawing direction. For an accurate comparison, the central region of the samples was examined for all conditions. Recrystallization fraction maps were plotted and quantified to reveal deformed, substructured, and recrystallized structures using HKL channel 5 software.

2.3 Results

2.3.1 As-cast microstructure

Figure 2-2 shows the as-cast microstructures of the four experimental alloys, which generally consist of α-Al matrix and Fe-rich intermetallic phases distributed along the aluminum dendrite boundaries. The types of the Fe-rich intermetallic phases were identified using SEM-EDS analysis and were dependent on the Fe and Si contents of the alloys. The SEM-EDS spectra corresponding to the intermetallic phases arrowed in Figure 2-2a-d, together with their detected atomic compositions are shown in Figure 2-3a-d, respectively. The skeleton-like α-Al_8Fe_2Si phase was formed in both alloys A and B (Figure 2-2a and b), which contained the highest levels of Fe and Si. In alloy C containing Fe with almost no Si, the feather-like Al_mFe was the dominant phase (Figure 2-2c). The microstructure of alloy D with low Fe and Si contents contained very small particles of the α-Al_8Fe_2Si phase (Figure 2-2d). Similar formations of Fe-rich intermetallic phases have also been reported in aluminum alloys with comparable levels of Fe and Si [36-38]. No primary intermetallic phases containing Zr and/or Sc were detected in the alloys, which implies that Zr and Sc solutes were highly dissolved in the α-Al matrix. Based on this observation, the solution treatment at 600 ºC for 8 h after hot rolling (Figure 2-1) is not necessary at such relatively low Zr and Sc levels in the industrial process.

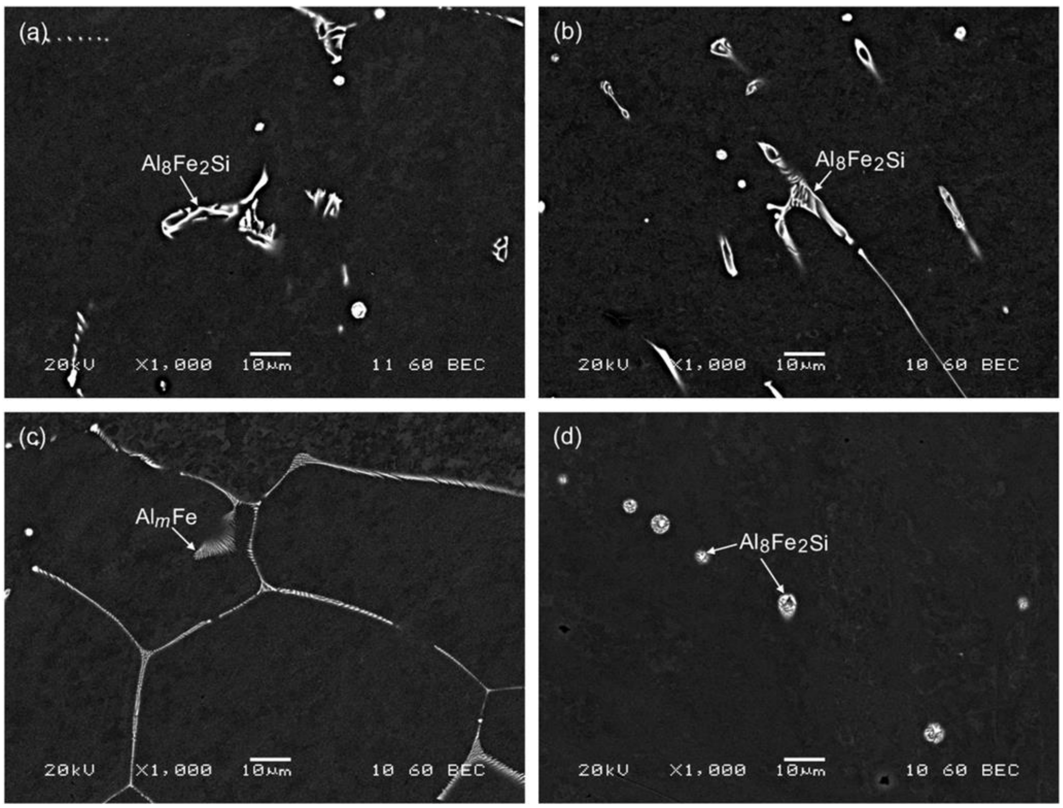

Figure 2-2 SEM backscattered images showing Fe-rich intermetallic phases formed in alloys (a) A, (b) B, (c) C, and (d) D in the as-cast condition.

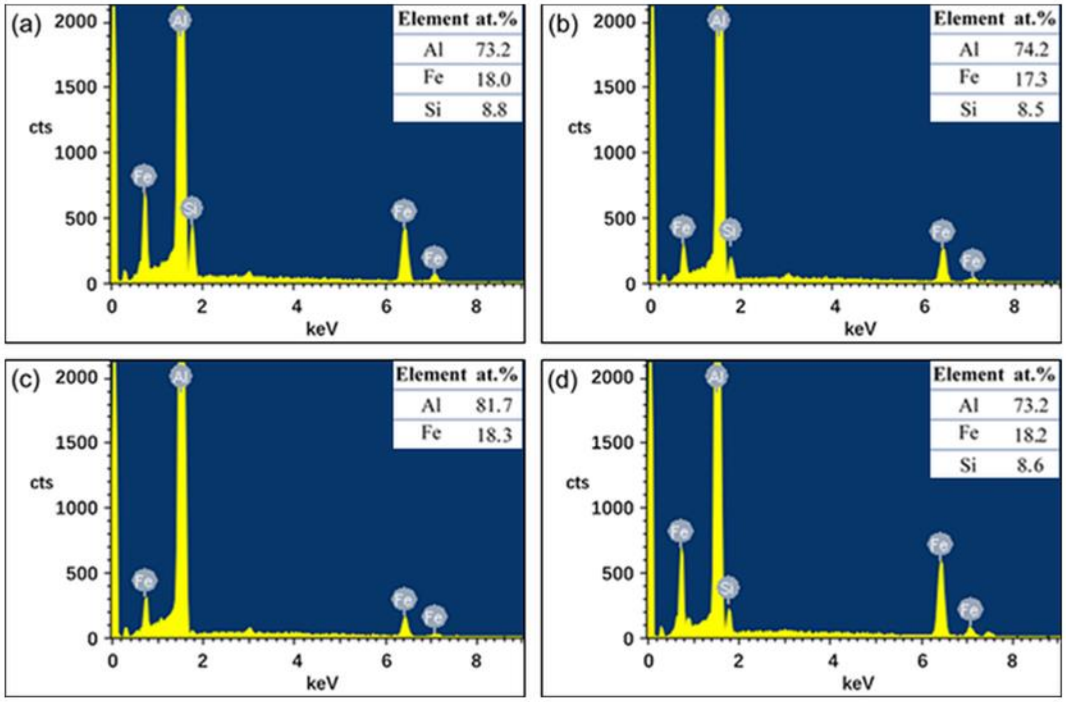

Figure 2-3 SEM-EDS spectra and atomic compositions of the Fe-rich intermetallic phases formed in alloys (a) A, (b) B, (c) C, and (d) D in the as-cast condition (Figure 2-2).

2.3.2 Effect of aging and alloying elements on the microhardness and electrical conductivity

Following rolling and solutionizing, the effect of different aging treatments on the microhardness and EC of the four alloys was preliminary examined prior to wire drawing, namely before undergoing the two typical thermomechanical processing routes (R1 and R2, Figure 2-1), and the results are shown in Figure 2-4. For all alloys, the microhardness increased in the first 24 h of aging and then nearly plateaued as the aging time increased (Figure 2-4a and c). The Sc-free base A alloy exhibited a very low aging response at both aging temperatures (Figure 2-4a), where the microhardness was increased form 35 HV in the as-solutionized condition to 45 and 41 HV in the peak-aged conditions at 400 and 450 ºC, respectively. The low aging response of Al-Zr alloys was also reported in other studies [39, 40].

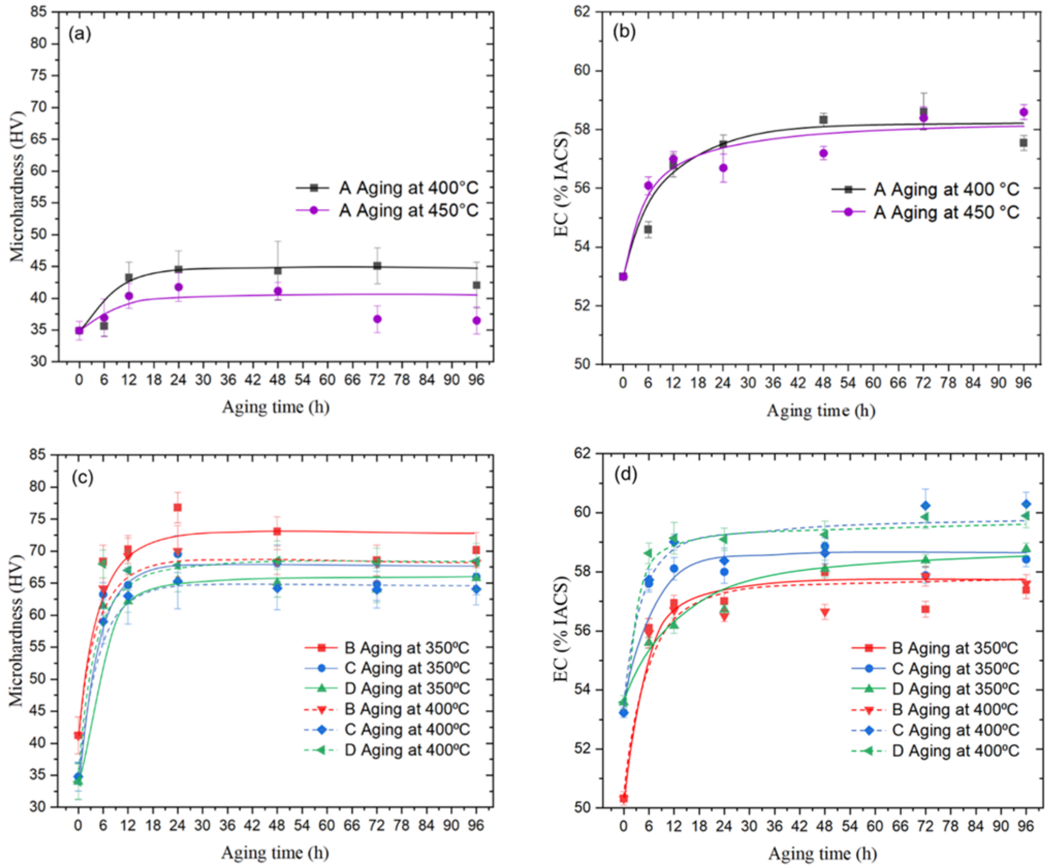

Figure 2-4 Evolution of the microhardness and EC with the aging time for (a, b) the base A alloy at 400 and 450 ºC and (c, d) the Sc-containing alloys at 350 and 400 ºC.

On the other hand, the Sc-containing B, C, and D alloys showed a strong aging response; as, for instance, the microhardness of alloy B was increased form 41 HV in the as-solutionized condition to 73 and 68 HV in the peak-aged conditions at 350 and 400 ºC, respectively. Accordingly, the Sc-containing alloys exhibited remarkably higher microhardness values compared with the base A alloy for all aging conditions with peak values of 65–73 HV. This reveals the effective strengthening effect of Sc when combined with Zr. Amongst the Sc-containing alloys, the highest microhardness was attained in alloy B (73 HV) followed by alloys C and D (68 and 65 HV, respectively) at 350 ºC, and in alloys B and D (68 HV) followed by alloy C (65 HV) at 400 ºC.

Generally, the EC increased sharply in the first 12 h of aging and then continued to increase slowly until attaining its maximum values (Figure 2-4b and d). The evolution of the EC with the aging time arose from the progressive decomposition of the α-Al solid solution and the formation of $Al_3Zr/Al_3(Zr,Sc)$ precipitates. In the solution-treated condition (0 h), the α-Al solid solution was highly supersaturated with solute atoms of alloying elements, particularly Sc and Zr, which could effectively scatter the electrons, resulting in low EC values (50.3–53.6% IACS). With increasing the aging time, the α-Al solid solution decomposed into $Al_3Zr/Al_3(Zr,Sc)$ precipitates, which nucleated rapidly in the early stages of aging and then grew slowly, leading to two different gradients of EC. The base alloy A had almost similar ECs at both 400 and 450 ºC with a maximum value of 58.0% IACS. For the Sc-containing alloys, the EC exhibited higher values at 400 ºC compared to those at 350 ºC, more specifically for alloys C and D. In both 350 and 400 ºC aging conditions, the maximum EC was reached by alloys C and D (58.6–60.0% IACS) followed by alloy B (57.6–57.9% IACS).

Based on the above results, it appears that the base A alloy reached the peak hardness after 48 h at 400 ºC with microhardness and EC values of 45 HV and 58.0% IACS, respectively. Thus, this aging condition was adopted for both R1 and R2 routes of the base A alloy. For the Sc-containing alloys, both B and C alloys attained the peak hardness after 48 h at 350 ºC with microhardness and EC values of 73 HV and 57.6% IACS, respectively, for the former and 68 HV and 58.6 %IACS, respectively, for the latter. On the other hand, the peak hardness of alloy D required higher aging temperature, as it was attained after 48 h at 400 ºC with microhardness and EC values of 68 HV and 59.2% IACS, respectively. Because these values were close to those obtained after 48 h at 350 ºC (65 HV and 58.2% IACS), aging at 350 ºC for 48 h was applied for the R1 and R2 routes of the three Sc-containing B, C, and D alloys.

2.3.3 Mechanical properties and electrical conductivity of the wires

The microhardness and EC of the wires typically produced by routes R1 and R2 are shown in Figure 2-5. The superior microhardness of the Sc-containing alloys compared to the base alloy was evidenced in both process routes. The base A alloy displayed very low microhardness (42-43.8 HV) with relatively high EC (58.1–58.7% IACS). Alloy B exhibited the highest microhardness (70.9-76.6 HV) and lowest EC (57.4–58% IACS) among the four alloy wires followed by alloys C and D, which showed almost similar microhardness and EC values in each route. Regarding the effect of the thermomechanical process routes, the microhardness and EC values in routes R1 and R2 were slightly varied, showing moderately higher hardness and lower EC in route R1 compared to route R2. For instance, alloy C with route R1 had 71.2 HV and 58.5% IACS, whereas the same alloy with route R2 had 66.8 HV and 59.5% IACS.

The UTS and El of the wires are shown in Figure 2-6 for routes R1 and R2. The variation of the UTS with the alloy composition and process route agrees well with the results of microhardness (Figure 2-5a and b). The UTS of the base A alloy was found to range between 121 and 105 MPa in R1 and R2, respectively. These values were deemed insufficient to meet the minimum specified UTS of the thermal-resistant Al alloy conductors (159 MPa, Table 2-1). In contrast, the UTSs of the three alloys microalloyed with Sc, ranged from 196 to 209 MPa in R1 and from 188 to 197 MPa in R2, which well exceeded the minimum specified UTS of AT1, AT3 and AT4 grades (159 MPa, Table 2-1). The elongations of the Sc-containing alloys ranged from 4.6% to 6.9% in R1 and from 5.2% to 9.3% in R2, greatly exceeding the minimum specified elongation of the thermal-resistant Al alloy conductors (2.0%, Table 2-1).

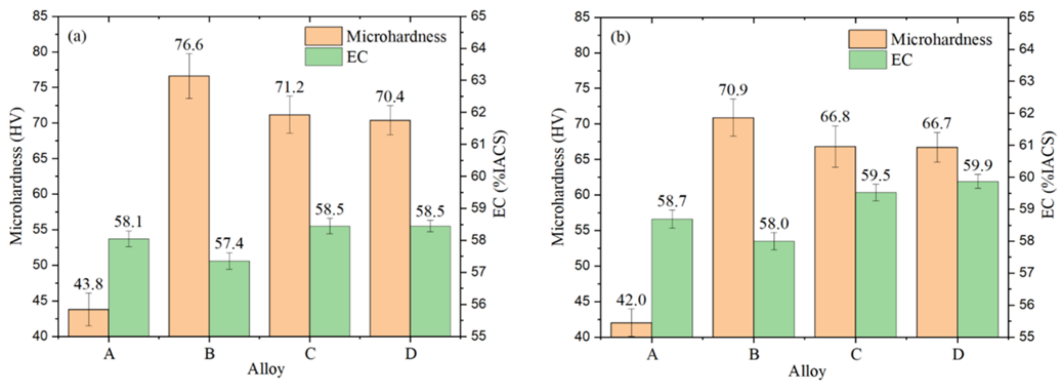

Figure 2-5 Microhardness and EC of alloy wires processed with routes R1 (a) and R2 (b).

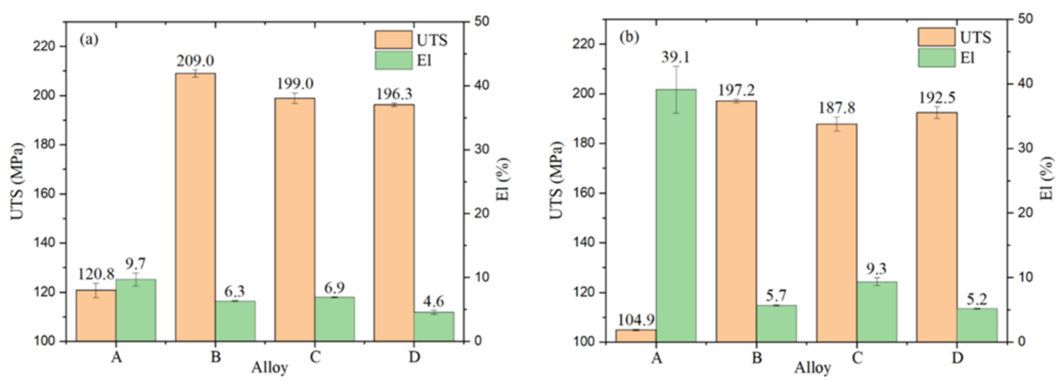

Figure 2-6 UTS and El of alloy wires processed with routes R1 (a) and R2 (b).

2.3.4 Thermal-resistant properties of the wires

The thermal-resistant properties of the Sc-containing B, C, and D alloys were evaluated after thermal exposure at 400 ºC for 1 h and 310 ºC for 400 h according to the specifications defined for the AT4 grade (Table 2-1), which represents the highest standard among the four grades. The UTSs of the three alloys before and after these exposures are compared in Figure 2-7 for routes R1 and R2. Both thermal exposures did not generate remarkable reductions in the UTSs for the three alloys. The maximum reductions were found in alloy B, which reached 6.0% and 3.4% in R1, and 3.5% and 4.0% in R2. However, these reductions are still less than 10%, implying that alloys B, C, and D can fulfill the highest thermal-resistant properties of the four grades (Table 2-1).

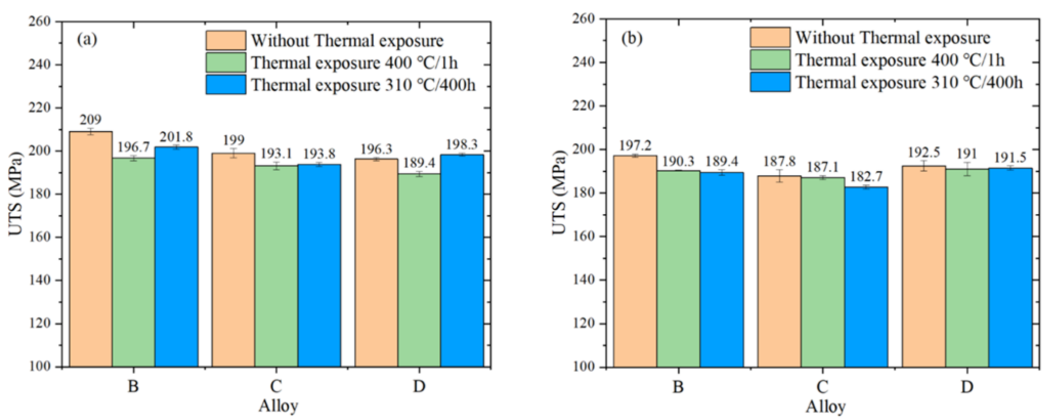

Figure 2-7 Effect of different thermal exposures on the UTS of alloy wires processed with routes R1 (a) and R2 (b).

To further confirm the thermal-resistant properties under long-term exposure at elevated temperatures, the evolution of the microhardness of the three Sc-containing alloy wires was examined during exposure at 310 ºC for up to 1000 h, and the results are shown in Figure 2-8. The three alloys highly preserved their thermal resistant properties even after the prolonged thermal exposure of 1000 h. The microhardness of alloys C and D showed only a slight decrease with the increased exposure time of 1000 h in both R1 and R2 routes. Alloy B displayed the maximum reductions of the microhardness in both R1 and R2 routes, where the microhardness values were decreased from 76.6 and 70.9 HV at 0 h to 70 and 67.5 HV at 1000 h, representing reductions of 8.6% and 4.8%, respectively.

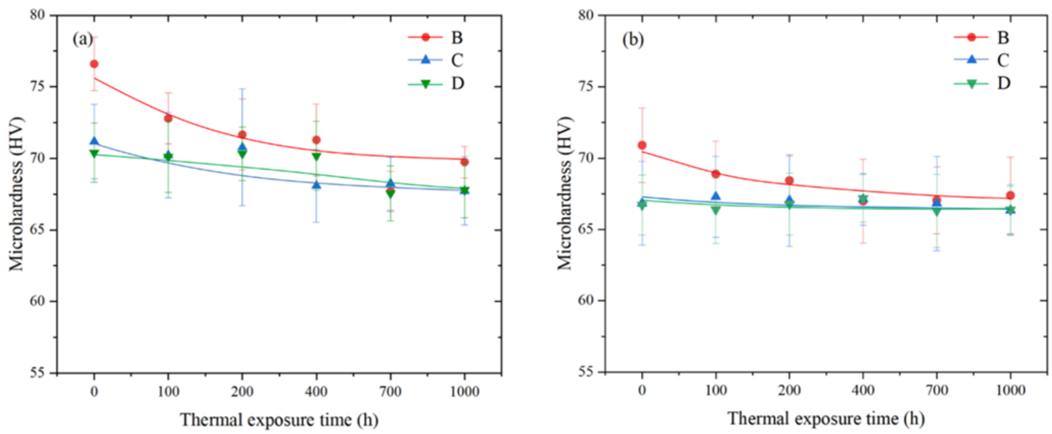

Figure 2-8 Evolution of the microhardness of alloy wires during thermal exposure at 310 ºC with different times in routes R1 (a) and R2 (b).

2.3.5 Precipitate microstructure

The dark-field TEM images in Figure 2-9a-d show the precipitate microstructures of the four alloy wires processed with route R2. Only a small number of relatively large sized Al_3Zr precipitates were found in the base A alloy (Figure 2-9a). In the Sc-containing B, C, and D alloys, fine dense $Al_3(Sc,Zr)$ precipitates were generally observed (Figure 2-9b-d). The corresponding selected area electron diffraction patterns (SAEDPs) are shown in Figure 2-9e-h, revealing faint spots from Al_3Zr and $Al_3(Sc,Zr)$ precipitates with the crystal plane indexes of these precipitates and α-Al. The orientation relationship between the precipitates and α-Al was found to be $[100]_{Al}//[100]_{precipitates}$, indicating the coherent boundaries between these $L1_2$ precipitates and α-Al [16, 18]. The quantitative results of precipitate characteristics are summarized in Table 2-3. The $Al_3(Sc,Zr)$ precipitates formed in alloys B, C, and D had higher number density (1.08×10^{22} - 1.19×10^{22} m^{-3}) and smaller size (5.3 - 5.6 nm) compared with the Al_3Zr precipitates formed in the base A alloy (0.03×10^{22} m^{-3} and 8.8 nm, respectively), explaining the large difference in the mechanical properties of the samples without and with Sc addition even at low Sc levels (Figure 2-4 to 6).

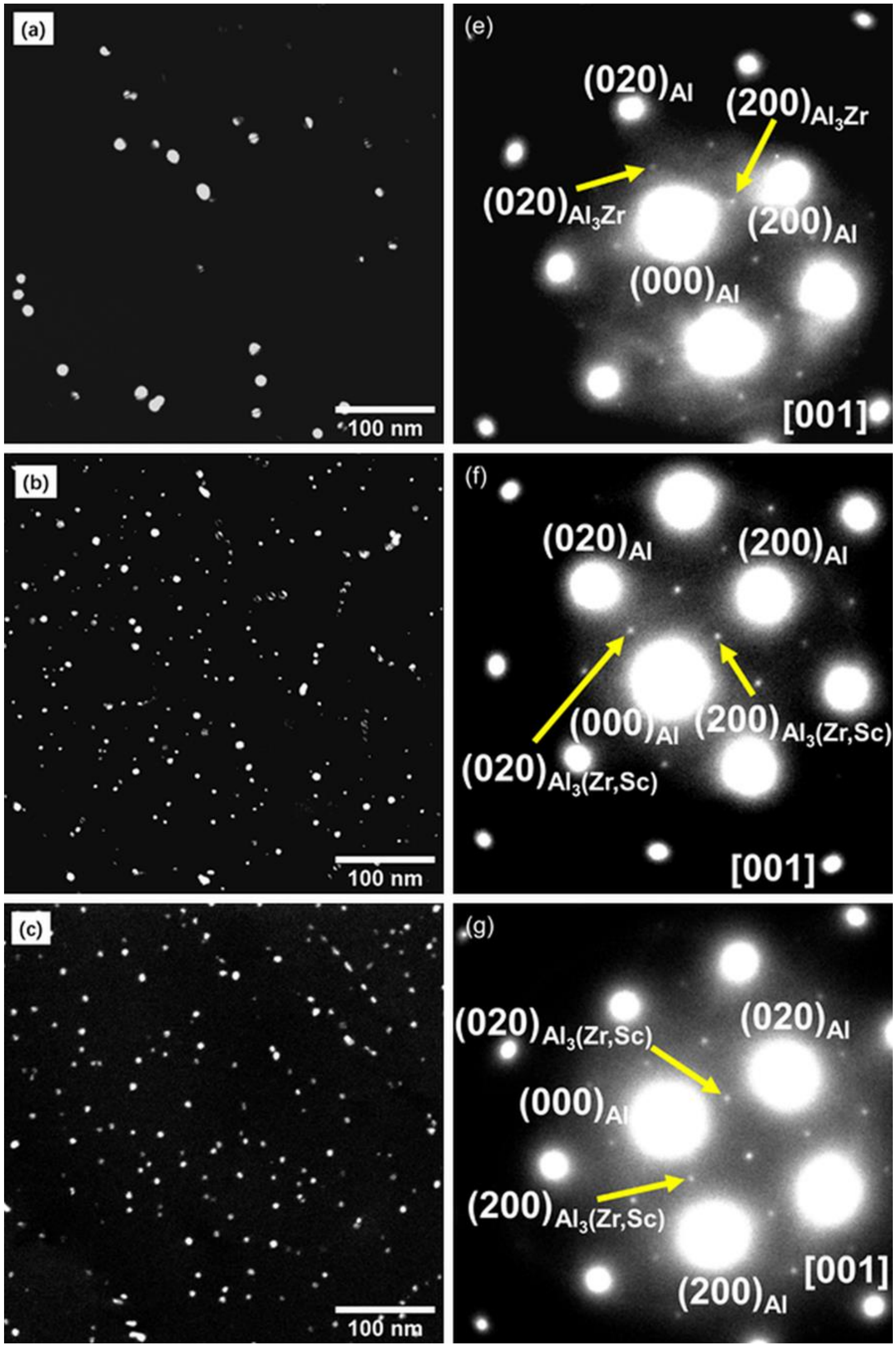

Figure 2-9 Dark-field TEM images showing precipitate microstructures of the Sc-free A alloy and the Sc-containing B, C, and D alloys processed with route R2 (a-d), and corresponding SAEDPs (e-h).

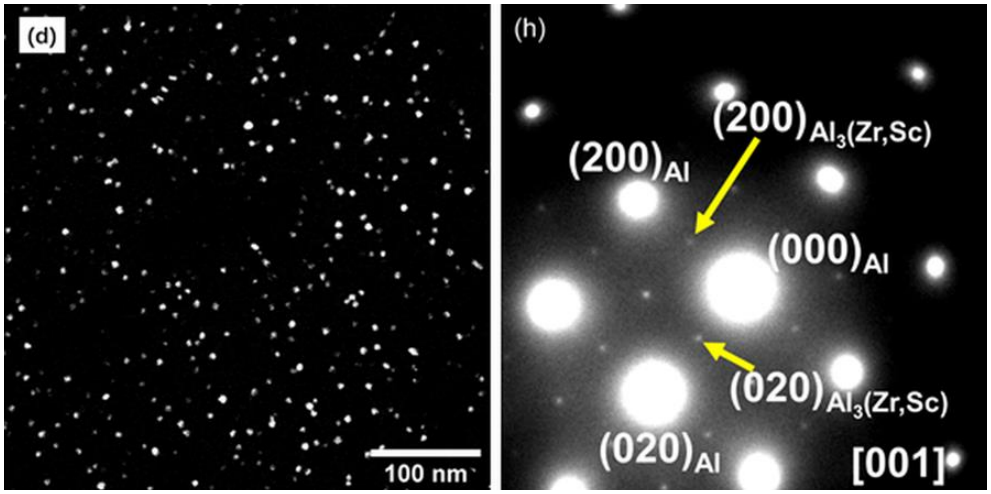

Figure 2-9 Continued. (Caption shown on the previous page).

Table 2-3 Characteristics of the precipitates in the experimental alloys.

Alloy	Number density, $\times 10^{22}$ m^{-3}	Average diameter, nm
A-R2	0.03 ± 0.04	8.8 ± 2.5
B-R2	1.19 ± 0.22	5.6 ± 1.6
C-R2	1.08 ± 0.11	5.5 ± 1.3
D-R2	1.16 ± 0.37	5.3 ± 1.1
B-NW[a]	1.28 ± 0.39	5.2 ± 1.6
B-R1	1.17 ± 0.30	5.0 ± 1.4
B-R2-TE[b]	1.03 ± 0.31	6.1 ± 1.9

[a] NW means that no wire drawing was conducted either before or after aging.
[b] TE refers to thermal exposure at 310 ºC/1000 h.

The effect of cold wire drawing on the characteristics of the Al_3(Sc,Zr) precipitates was also investigated by comparing the precipitates in alloy B, as an example, without wire drawing (B-NW) and with wire drawing either before or after aging (B-R2 and B-R1, respectively). The bright and dark field TEM images in Figure 2-10 were taken in such a way as to show coexistences of both dislocations and $Al_3(Sc,Zr)$ precipitates in the same microstructural zones for B-NW, B-R1 and B-R2 alloys. No dislocations were found in alloy B-NW (Figure 2-10a), as the solution treatment annihilated the dislocations induced by the hot rolling. The corresponding dark field TEM image (Figure 2-10b) shows that the fine $Al_3(Sc,Zr)$ precipitates were uniformly distributed in the Al matrix in this condition with a number density and an average diameter of 1.28×10^{22} m^{-3} and 5.2 nm, respectively (Table 2-3).

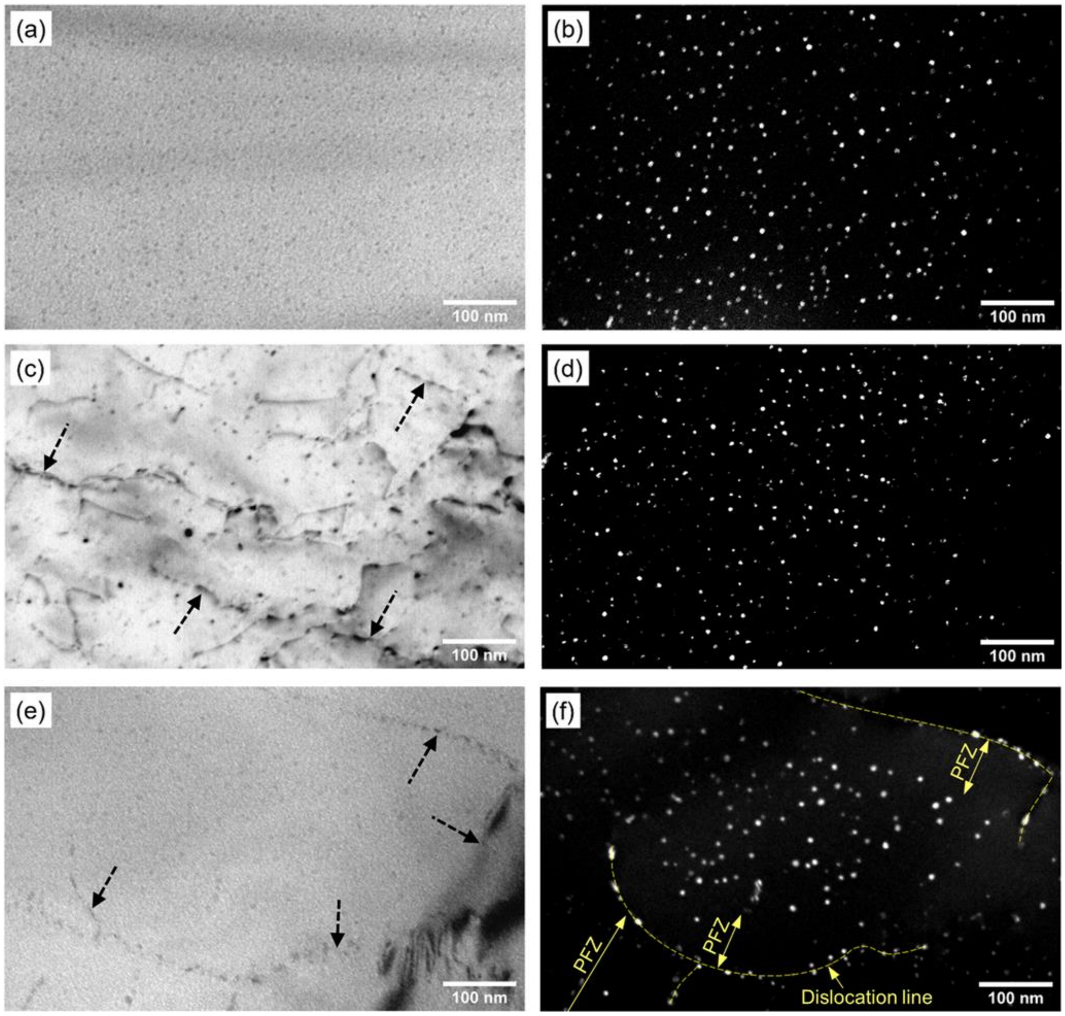

Figure 2-10 Bright and dark field TEM images taken from the same microstructural zones for alloys B-NW (a, b), B-R1 (c, d) and B-R2 (e, f). The arrows in (c) and (e) refer to dislocations.

A high-density dislocation network was found in alloy B-R1 (Figure 2-10c), even though the wires were annealed at 350 ºC for 5 h after cold wire drawing. The $Al_3(Sc,Zr)$ precipitates were distributed in the Al matrix independently on the dislocations (Figure 2-10d). As can be seen from Table 2-3, the number density of the $Al_3(Sc,Zr)$ precipitates in alloy B-R1 was slightly lower than that in alloy B-NW (1.17×10^{22} m^{-3} *vs*. 1.28×10^{22} m^{-}

^{3}). Considering the high thermal stability of the $Al_3(Sc,Zr)$ precipitates and the sluggish diffusivity of Zr and Sc in Al, these precipitates were, therefore, not supposed to redissolve into the matrix during cold wire drawing [41]. Instead, fine $Al_3(Sc,Zr)$ precipitates could be sheared by dislocations during wire drawing into fragmented precipitates [42, 43], which would be too small to be counted, resulting in a slightly lower number density of $Al_3(Sc,Zr)$ precipitates in alloy B-R1.

The dislocation density was decreased in alloy B-R2 e), which can be attributed to the post aging (350 ºC/48 h) after cold wire drawing. $Al_3(Sc,Zr)$ precipitates seemed to be heterogeneously nucleated on the dislocations, which pre-existed before aging, as can be observed from the presence of relatively large precipitates along the dislocations (Figure 2-10f). It is also interesting to observe precipitate-free zones (PFZs) adjacent to dislocation lines, where the dislocations could act as sinks for quenched-in vacancies [44, 45]. In the areas with low dislocation density, the precipitation of the $Al_3(Sc,Zr)$ precipitates was enhanced, as the strong binding energy between Sc atoms and excess vacancies created by the prior cold drawing process was reported to promote the precipitation kinetics of Al_3Sc precipitates [46, 47]. Thus, the number densities of $Al_3(Sc,Zr)$ precipitates in alloys B-R1 and B-R2 were similar despite the difference in their distribution.

The evolution of $Al_3(Sc,Zr)$ precipitates in alloy B-R2 after the prolonged 310 ºC/1000 h thermal exposure was also examined, and the corresponding TEM images are shown in Figure 2-11, while the quantitative results are listed in Table 2-3 (alloy B-R2-TE). It is interesting to observe the presence of dislocations after such long-term thermal exposure and that $Al_3(Sc,Zr)$ precipitates nucleated and grew along the dislocation lines. It is apparent that the precipitates exhibited a lower number density with a larger size compared with those without thermal exposure (B-R2-TE *vs*. B-R2, Table 2-3). The number density was decreased by 13.4% (1.03×10^{22} m^{-3} *vs*. 1.19×10^{22} m^{-3}), whereas the average diameter was increased by 8.9% (6.1 nm *vs*. 5.6 nm). Accordingly, the Al_3(Sc,Zr) precipitates were slightly coarsened after the prolonged thermal exposure, which is consistent with the marginal reduction in the microhardness of alloy B-R2 after such thermal exposure (Figure 2-8b).

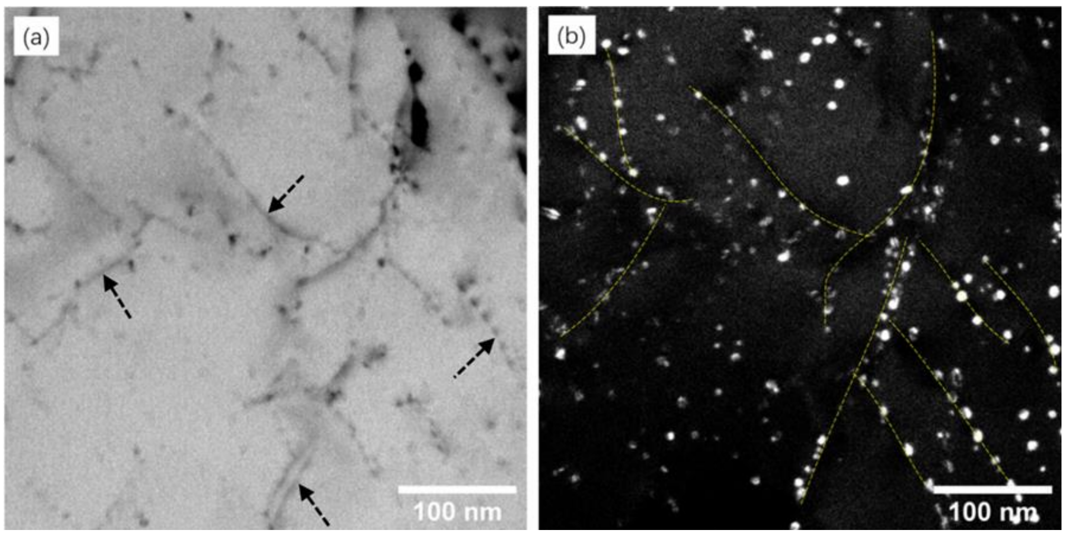

Figure 2-11 Bright and dark field TEM images showing dislocations and Al_3(Sc,Zr) precipitates in alloy B-R2-TE subjected to 310ºC/1000h thermal exposure. The arrows in (a) refer to dislocations.

2.3.6 Effect of the thermomechanical processing on the deformed microstructure

All-Euler orientation and grain orientation spread (GOS) maps of alloy B in different stages of the two thermomechanical processing routes are shown in Figure 2-12. The deformed, substructured, and recrystallized grains were indicated in the GOS maps by red, yellow, and blue colors. The statistical distribution results of these grain structures are shown in Figure 2-13. In the solution treated condition after hot rolling (Figure 2-12a and b), the microstructure was comprised of substructured grains (81%) and a recrystallized structure (19%). Subsequently, the evolution of the grain structure was varied with the processing route. In route R1, conducting aging at 350 ºC/48 h prior to the cold wire drawing (Figure 2-12c and d), increased the fraction of the recrystallized structure at the expense of the substructure relative to the solution treated condition (40% and 60% *vs*. 19% and 81%). The cold wire drawing significantly strengthened the microstructure (Figure 2-12e and f) by introducing a 96% deformed structure with fibrous grains along the drawing direction and decreasing the substructure and recrystallized structure to 2.5% and 1.5%, respectively. Subsequent annealing at 350 ºC for 5 h slightly decreased the strain hardening effect of the cold wire drawing (Figure 2-12g and h), decreasing the deformed structure from 96% to 93%, while increasing the substructure from 2.5% to 6% with almost no change in the recrystallized structure.

In route R2, conducting cold wire drawing directly after the solution treatment, remarkably strengthened the microstructure Figure 2-12, resulting in a 98% deformed structure, thereby decreasing the substructure and the recrystallized structure to 0.7% and 1.3%, respectively. The elongated fibrous grains were observed along the drawing direction. The post-aging of the cold-drawn wire at 350 ºC for 48 h partially relieved the work hardening of the cold drawing (Figure 2-12k and l); the deformed structure was decreased from 98% to 85%, whereas the substructure and the recrystallized structure were increased from 0.7% and 1.3% to 12% and 3%, respectively. Accordingly, the wire materials had a higher fraction of deformed structure in route R1 than that in route R2 (93% *vs*. 85%).

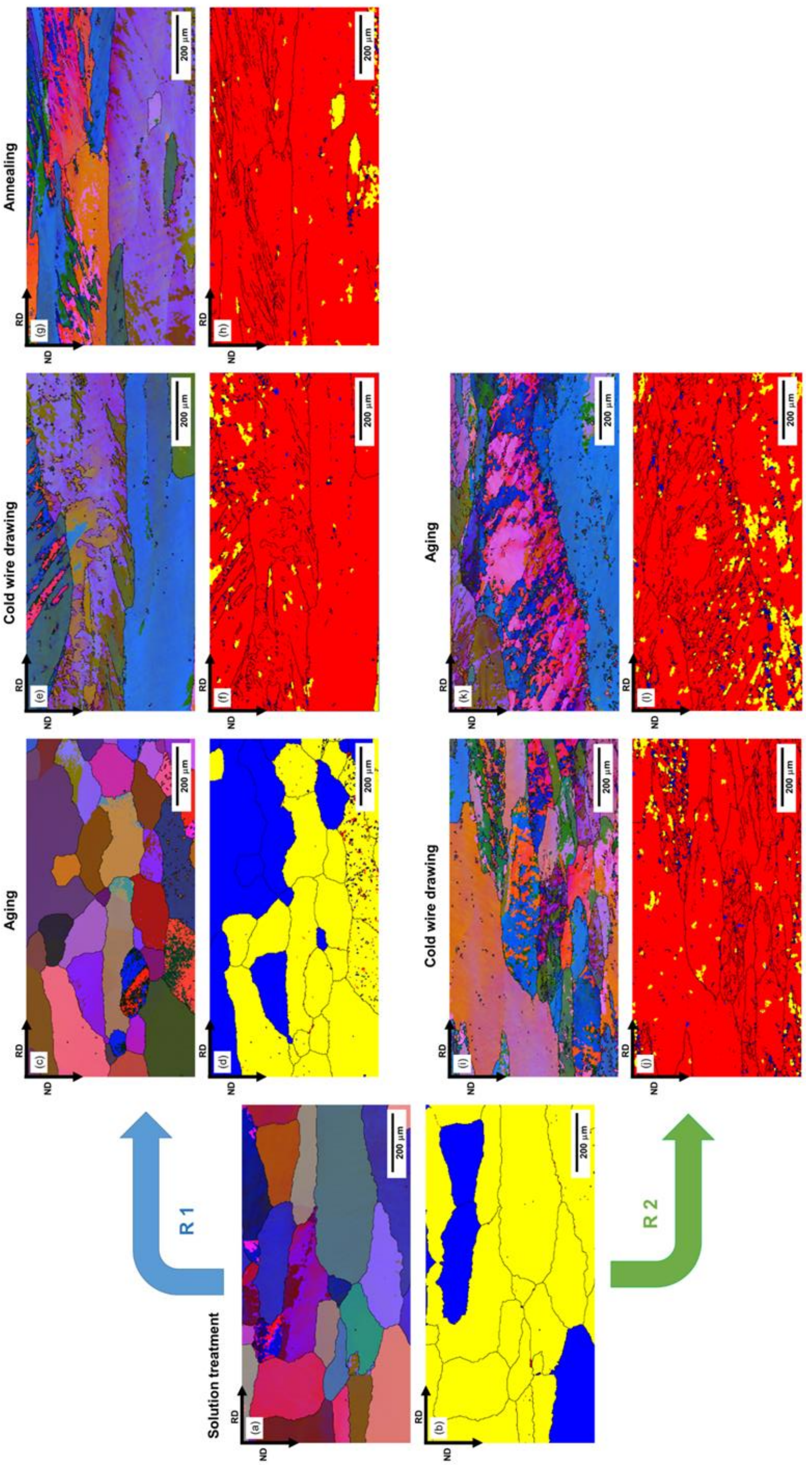

Figure 2-12 All-Euler orientation and grain orientation spread (GOS) maps of alloy B in different stages of the processing routes R1 and R2: (a, b) solution treatment after rolling; in R1 (c, d) aging, (e, f) cold wire drawing, and (g, h) annealing; in R2 (i, j) cold wire drawing, and (k, l) aging.

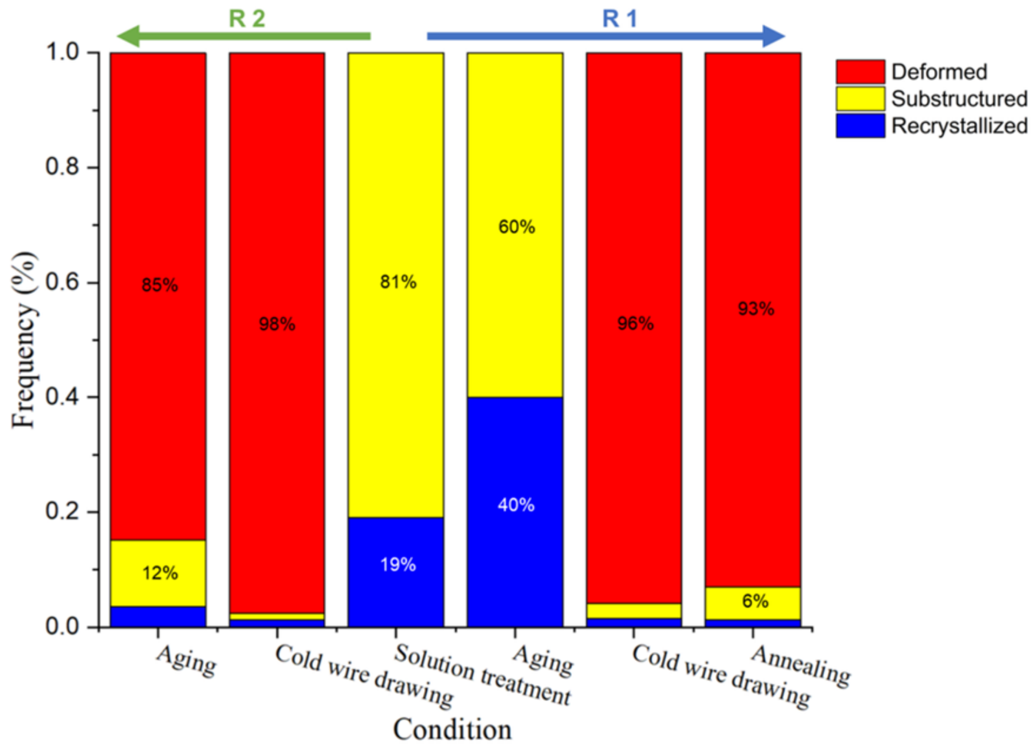

Figure 2-13 Statistical distribution of the fractions of the structures revealed by the GOS maps in Figure 2-12.

2.4 Discussion

2.4.1 Effect of alloying elements and aging treatment on the mechanical properties and electrical conductivity

The results obtained above reveal that the Al-Zr base alloy could hardly achieve the required strength for the thermal-resistant aluminium conductors (121 *vs*. 159 MPa) owing to the weak aging response and insufficient strengthening of the Al_3Zr precipitates (Figure 2-4a). Increasing the Zr level (> 0.14 wt. %) is not expected to bring a significant improvement in terms of strength, because the solubility of Zr in Al at the liquidus temperature is limited to approximately 0.12 wt. %, which in turn limits the amount of Zr solutes in the solid Al. On the other hand, microalloying with Sc even at a low level (< 0.1 wt. %), namely alloys B, C, and D, produced a substantial increase in the UTS of 73% in route R1 and 88% in route R2 relative to the base alloy (Figure 2-6). Accordingly, the UTSs of the Sc-containing alloys exceeded the minimum specified UTS for AT1, AT3, and AT4 grades (188-209 *vs*. 159 MPa). The strength improvement can undoubtedly be attributed to the precipitation of a large amount of nanosized $Al_3(Sc,Zr)$ precipitates (Table 2-3). Considering the higher diffusivity of the Sc in Al relative to Zr [48], Sc-rich clusters and fine Al_3Sc particles can be formed in Al-Zr-Sc alloys during the early stages of aging [49-51] With increasing aging temperature and time, Zr diffuses to form Zr-rich shells around these precipitates, resulting in uniformly distributed core-shell $L1_2$-$Al_3(Sc,Zr)$ precipitates [31, 52-54]. Simultaneously with the high strength, the Sc-containing alloys also provided high electrical conductivities of 57.4-59.9% IACS (Figure 2-5), which were either close to or higher than the requirements of the four grades (55.0–60.0% IACS). These results indicate that the applied aging treatment at 350 ºC/48 h effectively decomposed the α-Al solid solution, decreasing the solute concentration while increasing the $Al_3(Sc,Zr)$ precipitates, which resulted in mutual improvement in the strength and electrical conductivity.

The additions of Fe and Si affected the mechanical properties and electrical conductivity of the alloys to some extent (Figure 2-4 to 2-6). The higher mechanical properties and lower electrical conductivity of alloy B could be related to its higher content of Si relative to alloys C and D (0.24% *vs*. 0.03% and 0.07%). Solute atoms of Si in the Al matrix could increase the strength via solid solution strengthening, but decrease the electrical conductivity [20, 41]. Iron seems to have a less significant effect on the solute supersaturation, where both alloy C containing 0.27% Fe and alloy D with 0.07% Fe, attained more or less similar mechanical properties and electrical conductivities. It is worthwhile to note that the decomposition of the α-Al solid solution was much faster in alloys B and C compared to alloy D, where the electrical conductivity attained its maximum values much earlier in the former two alloys, particularly when aging at 350 ºC (Figure 2-4d). This can possibly be due to the higher levels of Si and Fe in alloy B (0.24% and 0.28% *vs*. 0.07% and 0.07% present in alloy D) and the higher level of Fe in alloy C (0.27% *vs*. 0.07% present in alloy D), where both elements were reported to accelerate the precipitation kinetics of Al_3Zr, Al_3Sc, and $Al_3(Zr,Sc)$ precipitates [33, 34, 55-57].

When comparing both 350 and 400 ºC aging treatments, aging at 400 ºC increased the electrical conductivity of alloys C and D to some extent (1.5% IACS after 96 h for alloy C and 3% IACS after 12 h for alloy D, as shown in Figure 2-4d). On the other hand, increasing the aging temperature from 350 to 400 ºC decreased the peak microhardness for alloys B and C from 73 and 68 HV to 68 and 65 HV, respectively, but increased that of alloy D from 65 to 68 HV. The observed increases in microhardness and electrical conductivity of alloy D indicate that the slow precipitation kinetics of $Al_3(Sc,Zr)$ precipitates in this alloy relative to alloys B and C, which was attributed above to its lower Si and Fe contents, could be enhanced when increasing the aging temperature to 400 ºC.

2.4.2 Effect of thermomechanical processing on the mechanical properties and electrical conductivity

Figure 2-14 shows the evolution of the microhardness and EC of alloy B, as an example, during the thermomechanical processing with routes R1 and R2. The microhardness was 41 HV in the solution treated condition and increased to 73 HV after aging (350 ºC/48 h) in route R1 and to 52.5 HV after cold wire drawing in route R2. The increase in hardness from the aging process, which occurred via the precipitation hardening of the $Al_3(Sc,Zr)$ precipitates, was significantly higher than that from the strain hardening of the cold wire drawing (32 HV *vs*. 11.5 HV). These increases represent the hardening effects of the aging treatment and the cold wire drawing independently of each other. However, the combined hardening effect of both processes after thermomechanical processing was determined by their sequence in routes R1 and R2.

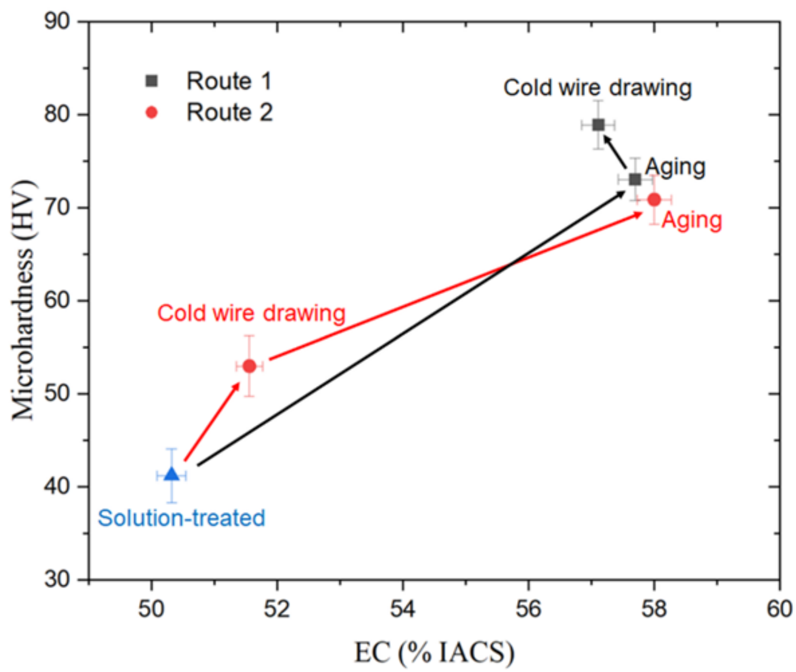

Figure 2-14 Evolution of the microhardness and EC of alloy B during thermomechanical processing in routes R1 and R2.

In route R1, the cold wire drawing increased the microhardness from 73 to 79 HV through the strain hardening effect, which was confirmed by the increase of the deformed structure according to EBSD analysis (Figure 2-12e and f). On the other hand, the electrical conductivity was slightly decreased from 57.7% IACS to 57.1% IACS. The electrical conductivity was reported to decrease after cold deformation due to the scattering of conduction electrons by dislocations [20, 41, 56]; however it could also be improved through the closure of microvoids during cold deformation [24, 58]. This can explain the slight reduction of the electrical conductivity after cold wire drawing (0.6% IACS), which was similarly reported by Guan *et al*. [58]. Annealing at 350 ºC for 5 h after cold wire drawing slightly decreased the strain hardening effect (Figure 2-12g and h); the microhardness decreased from 79 to 76.6 HV but the electrical conductivity increased from 57.1% IACS to 57.4% IACS.

In route R2, the aging process was conducted after the cold wire drawing and resulted in a slightly lower microhardness than that attained after the aging in route R1 (70.9 *vs*. 73 HV). This can be attributed to the role played by the wire-drawing-induced dislocations in creating PFZs and nucleating relatively large $Al_3(Sc,Zr)$ precipitates (Figure 2-10f and Table 2-3). In addition, the post aging partially relieved the strain hardening effect of the wire drawing, as evidenced by the EBSD results (Figure 2-12k and l). The electrical conductivity was slightly increased when compared to that attained after aging only (58.0% IACS *vs*. 57.6% IACS). The increase of the electrical conductivity in route R2 was more pronounced for alloys C and D (58.5% and 58% IACS with aging only (Figure 2-4d) *vs*. 59.5% and 59.9% IACS with R2 (Figure 2-5b)), in which the precipitation kinetics of $Al_3(Sc,Zr)$ precipitates was lower than that of alloy B, due to their lower levels of Fe and Si. It is important to mention that conducting aging treatment after cold wire drawing in route R2 did not substantially relieve the strain hardening, where a high fraction of the deformed structure remained in the wire material after aging (85%, Figure 2-13). Jones *et al*. [59] found that the recrystallization was severely prevented in a pre-deformed Al-0.12 wt. % Sc alloy after annealing below 370 ºC, because the precipitation of Al_3Sc precipitates started before the recrystallization could take place.

After thermomechanical processing, the final mechanical properties and electrical conductivities of the alloy wires were determined by the precipitation of $Al_3(Sc,Zr)$ precipitates and the cold working of the wire drawing. However, there were no significant differences in the UTS and EC values between routes R1 and R2. When comparing the two routes, the former produced a maximum UTS increase of 12 MPa (Figure 2-6, alloy B-R1 *vs*. alloy B-R2), while the later resulted in a maximum EC increase of 1.4% IACS (Figure 2-5, alloy D-R2 *vs*. alloy D-R1). In terms of the microstructure, the $Al_3(Sc,Zr)$ precipitates exhibited almost similar characteristics (size and number density) in routes R1 and R2 (Table 2-3, alloy B-R1 *vs*. alloy B-R2), and thereby resulted in comparable precipitation strengthening. In addition, there were close fractions of the deformed structures in routes R1 and R2 (93% *vs*. 85%, Figure 2-12), which would, in turn, exert comparable strain hardening in both routes. In the industrial practice, both processing routes can be used for fine-tuning the trade-off between strength and EC.

2.4.3 Thermal-resistant property

All of three Sc-containing alloys satisfied the thermal-resistant properties of the four grades. The maximum strength reduction was ≤ 6.0% after thermal exposure at 310 ºC for 400 h and 400 ºC for 1 h (Figure 2-7). The outstanding thermal resistance properties of the Sc-containing alloys can be attributed to the role of the coarsening-resistant core-shell $Al_3(Sc,Zr)$ precipitates not only in maintaining the precipitation strengthening after thermal exposure, but also in increasing the recrystallization resistance through the pinning of dislocations. Even after the long-term thermal exposure at 310 ºC for 1000 h, the pinning of dislocations by $Al_3(Sc,Zr)$ precipitates was still well preserved (Figure 2-11).

Although the reductions in the strength and microhardness of the three Sc-containing B, C, and D alloys after all thermal exposures were generally marginal, they were more observable in alloy B and route R1 (Figure 2-7 and 8). The high Si content of alloy B exerted an additional strengthening via the solid solution effect and accelerated the precipitation of $Al_3(Sc,Zr)$ precipitates; these effects would decrease with thermal exposure. The strain hardening of the post wire drawing in route R1 could also be gradually diminished with increasing exposure temperatures and time (Figure 2-8a). On the other hand, in route R2, the aging treatment at 350 ºC for 48 h after cold wire drawing already decreased the strain strengthening to some extent prior to the thermal exposure (Figure 2-13). Thus, both routes highly satisfied the thermal-resistant properties, but route R2 showed better thermal-resistant stability, particularly under long-term thermal exposure conditions (Figure 2-8b).

2.4.4 Evaluation of the material properties of the developed alloys

Based on the results obtained, the three Sc-containing B, C, and D alloys developed in this study showed a significant potential for producing thermal-resistant aluminium conductor wires according to the IEC 62004 standard [17]. Because the thermal resistant-properties and elongations of all three alloys fulfilled the particular requirements of AT1, AT2, AT3, and AT4 grades, the possible assignment of the alloys to those four grades can be made based on the UTS and EC values (Table 2-1). Figure 2-15 shows the comparison of UTS and EC values for alloys B, C, and D with the specified values for AT1, AT2, AT3, and AT4 grades. The AT4 grade is fully achievable by alloys B-R2, C-R1, and D-R1 with higher strengths (196-199 MPa *vs*. 159 MPa of AT4) and similar or even higher ECs (58.0-58.5% *vs*. 58% IACS). The strengths of the three alloys were approximately 25% superior to the standard ones. AT1 and AT3 grades with extra high EC are almost achievable by alloys C-R2 and D-R2. Considering their higher strengths relative to the specified strength (188-193 MPa *vs*. 159 MPa), a slight increase in the EC of these alloys is required to satisfy entirely the specifications of the AT1 and AT3 grades (59.5-59.9% *vs*. 60.0% IACS of AT1 and AT3). The increase in the EC could be easily attained by: i) increasing the aging time beyond 48 h; and ii) by the Boron-treatment of the melt [60-62]. The AT2 grade requires the higher strength (225 MPa) among the four grades, but a relatively low EC (55.0% IACS). In general, the mechanical strength and EC are mutually exclusive [20]. Fortunately, all three Sc-containing alloys possessed relatively higher ECs (57.4-59.9% *vs*. 55.0% IACS), and therefore, there is enough room for the trade-off between the EC and strength, which could be adjusted by i) a moderate increase of other alloying elements, such as Si and Fe; and ii) by optimizing the aging treatment. Alloys B-R1 (57.4% IACS and 209 MPa), B-R2 (58% IACS and 197 MPa) and C-R1 (58.5% IACS and 199 MPa) are all suitable candidates to achieve the goal of AT2 grade.

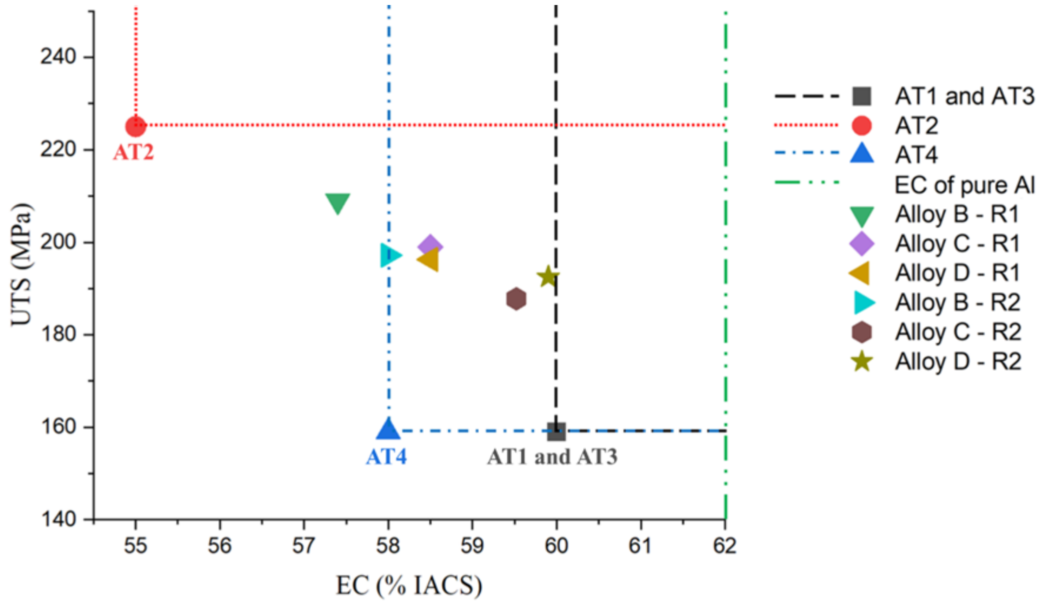

Figure 2-15 Comparison of the UTS and EC of the developed Sc-containing alloys with the standard values of four thermal-resistant conductor grades [17].

Table 2-4 Comparison of properties of alloys developed in this study and previous works.

Alloy composition (wt.%)	Tensile strength (MPa)	Electrical conductivity (% IACS)	Thermal-resistant temperature (ºC)		Possible IEC grade	Reference
			1 h heating	400 h heating		
Al-**0.07Sc**-0.11Zr-0.24Si-0.28Fe	197-209	57.4-58.0	400	310	AT2[a] and AT4	This work
Al-**0.07Sc**-0.08Zr-0.03Si-0.27Fe	188-199	58.5-59.5	400	310	AT1[b], AT2[a], AT3[b] and AT4	This work
Al-**0.09Sc**-0.12Zr-0.07Si-0.07Fe	193-196	58.5-59.9	400	310	AT1[b], AT3[b] and AT4	This work
Al-**0.35Sc**-0.20Zr-0.20Si-0.25Fe	210	60.2	230 and 400	Not verified	Not assessed	18
Al-**0.06Sc**-0.23Zr	194	61.0	Not verified at all		Not assessed	19
Al-**0.12Sc**-0.04Zr	160	64.0	Not verified at all		Not assessed	25
Al-**0.20Sc**-0.20Y	199-202	60.8-61.5	Not verified at all		Not assessed	26
Al-**0.05Sc**-0.10Zr-0.20Fe	166	60.3	230 and 400	Not verified	AT1[c]	27
Al-**0.12Sc**-0.04Zr	217	53.8	Not verified at all		Not assessed	30

Sc level is bolded to highlight the raw material cost of the alloys.

[a] Tensile strength to be adjusted to satisfy entirely the specifications of the AT2 grade.

[b] A slight increase in the electrical conductivity is required to satisfy entirely the specifications of the AT1 and AT3 grades.

[c] 180ºC/400h thermal exposure to be made to affirm the thermal-resistant property of the AT1 grade.

The alloys developed in this study were also compared to other Sc-containing conductor alloys in the literature, as summarised in Table 2-4. Evidently, the present alloys are distinct from the others as high thermal-resistant aluminium conductor materials balancing between the low material cost with the relatively low Sc levels and the satisfaction of overall standard specifications, including strength, electrical conductivity and thermal resistance.

2.5 Conclusions

The development of Al-Zr-Sc alloys for high thermal-resistant aluminium conductors was achieved in this work based on the targeted approach that focused on minimizing the material cost by a low level of Sc and on using conventional thermomechanical processes, while satisfying IEC standard properties for thermal-resistant aluminium conductors. Based on the results obtained, the following conclusions can be drawn.

1. The addition of a relatively low level of Sc ($\leq$ 0.10 wt.%) to the Al-Zr based alloy produced significantly higher strength of 188-209 MPa, representing 73-88% improvement relative to the base alloy, while maintaining excellent electrical conductivity of 57.4-59.9% IACS.

2. The significant strength increases in the Al-Zr-Sc alloys were attributed to better characteristics of the $Al_3(Sc,Zr)$ precipitates compared to the Al_3Zr precipitates formed in the Al-Zr base alloy; the number density and average size were, respectively, 1.08×10^{22} -

1.19×10^{22} m^{-3} and 5.3 - 5.6 nm for the former, and 0.03×10^{22} m^{-3} and 8.8 nm for the latter.

3. The outstanding thermal-resistant properties of the Sc-containing alloys limited the maximum strength reduction to ≤ 6.0% after thermal exposures at 310 ^{o}C for 400 h and 400 ^{o}C for 1 h due to the high coarsening resistance of $Al_3(Sc,Zr)$ precipitates, which not only maintained the precipitation strengthening, but also increased the recrystallization resistance.

4. Both processing routes R1 and R2 yielded comparable mechanical and electrical properties, providing flexibility for the industrial processing of aluminum conductors; the maximum differences in the strength and electrical conductivity between both routes were 12 MPa and 1.4% IACS, respectively.

5. The excellent combinations of mechanical, electrical, and thermal-resistant properties of the Sc-containing alloys made them promising low-cost materials for manufacturing different IEC standard grades of thermal-resistant aluminium conductors with conventional thermomechanical processes.

References

[1] Murashkin MY, Sabirov I, Sauvage X, Valiev R. Nanostructured Al and Cu alloys with superior strength and electrical conductivity. Journal of materials science 2016; 51(1):33-49.

[2] Blackburn JL. Symmetrical components for power systems engineering. CRC press2017.

[3] Yuan W, Liang Z. Effect of Zr addition on properties of Al–Mg–Si aluminum alloy used for all aluminum alloy conductor. Materials & Design 2011; 32(8-9):4195-4200.

[4] Kalombo R, Araújo J, Ferreira J, Da Silva C, Alencar R, Capra A. Assessment of the fatigue failure of an All Aluminium Alloy Cable (AAAC) for a 230 kV transmission line in the Center-West of Brazil. Engineering Failure Analysis 2016; 61:77-87.

[5] Adriano V, Martínez J, Ferreira J, Araújo J, Da Silva C. The influence of the fatigue process zone size on fatigue life estimations performed on aluminum wires containing geometric discontinuities using the Theory of Critical Distances. Theoretical and Applied Fracture Mechanics 2018; 97:265-278.

[6] 8134-1997 JT. Al-Mg-Si alloy wire for overhead line conductor.

[7] Yuan W, Liang Z, Zhang C, Wei L. Effects of La addition on the mechanical properties and thermal-resistant properties of Al–Mg–Si–Zr alloys based on AA 6201. Materials & Design 2012; 34:788-792.

[8] Zinatloo-Ajabshir S, Ghasemian N, Mousavi-Kamazani M, Salavati-Niasari M. Effect of zirconia on improving NOx reduction efficiency of Nd2Zr2O7 nanostructure fabricated by a new, facile and green sonochemical approach. Ultrasonics sonochemistry 2021; 71:105376.

[9] Zinatloo-Ajabshir S, Salavati-Niasari M. Facile synthesis of nanocrystalline neodymium zirconate for highly efficient photodegradation of organic dyes. Journal of Molecular Liquids 2017; 243:219-226.

[10] Zinatloo-Ajabshir S, Zinatloo-Ajabshir Z, Salavati-Niasari M, Bagheri S, Abd Hamid SB. Facile preparation of Nd2Zr2O7–ZrO2 nanocomposites as an effective photocatalyst via a new route. Journal of energy chemistry 2017; 26(2):315-323.

[11] Zinatloo-Ajabshir S, Salavati-Niasari M. Preparation of nanocrystalline cubic ZrO 2 with different shapes via a simple precipitation approach. Journal of Materials Science: Materials in Electronics 2016; 27:3918-3928.

[12] Zinatloo-Ajabshir S, Salavati-Niasari M. Facile route to synthesize zirconium dioxide (ZrO2) nanostructures: structural, optical and photocatalytic studies. Journal of Molecular Liquids 2016; 216:545-551.

[13] Li H, Bin J, Liu J, Gao Z, Lu X. Precipitation evolution and coarsening resistance at 400 C of Al microalloyed with Zr and Er. Scripta Materialia 2012; 67(1):73-76.

[14] Muthaiah VS, Mula S. Effect of zirconium on thermal stability of nanocrystalline aluminium alloy prepared by mechanical alloying. Journal of Alloys and Compounds 2016; 688:571-580.

[15] Robson J, Prangnell P. Dispersoid precipitation and process modelling in zirconium containing commercial aluminium alloys. Acta Materialia 2001; 49(4):599-613.

[16] Knipling KE, Dunand DC, Seidman DN. Precipitation evolution in Al–Zr and Al–Zr–Ti alloys during isothermal aging at 375–425 C. Acta Materialia 2008; 56(1):114-127.

[17] Thermal-resistant aluminium alloy wire for overhead line conductor. International Standard IEC 62004 2007.

[18] Guan R, Shen Y, Zhao Z, Wang X. A high-strength, ductile Al-0.35Sc-0.2Zr alloy with good electrical conductivity strengthened by coherent nanosized-precipitates. Journal of Materials Science & Technology 2017; 33(3):215-223.

[19] Li Liu J-TJ, Bo Zhang, Wen-Zhu Shao, Liang Zhen. Enhancement of strength and electrical conductivity for a dilute Al-Sc-Zr alloy via heat treatments and cold drawing. J. Mater. Sci. Technol. 2019; 35(6):962-971.

[20] Khangholi SN, Javidani M, Maltais A, Chen XG. Review on recent progress in Al–Mg–Si 6xxx conductor alloys. Journal of Materials Research 2022; 37(3):670-691.

[21] Fuller CB, Seidman DN, Dunand DC. Mechanical properties of Al(Sc,Zr) alloys at ambient and elevated temperatures. Acta Materialia 2003; 51(16):4803-4814.

[22] Knipling KE, Karnesky RA, Lee CP, Dunand DC, Seidman DN. Precipitation evolution in Al–0.1 Sc, Al–0.1 Zr and Al–0.1 Sc–0.1 Zr (at.%) alloys during isochronal aging. Acta Materialia 2010; 58(15):5184-5195.

[23] Knipling KE, Seidman DN, Dunand DC. Ambient-and high-temperature mechanical properties of isochronally aged Al–0.06 Sc, Al–0.06 Zr and Al–0.06 Sc–0.06 Zr (at.%) alloys. Acta Materialia 2011; 59(3):943-954.

[24] Zhou W, Cai B, Li W-J, Liu Z-X, Yang S. Heat-resistant Al–0.2 Sc–0.04 Zr electrical conductor. Materials Science and Engineering: A 2012; 552:353-358.

[25] Chao R-z, Guan X-h, Guan R-g, Di T, Chao L, Xiang W et al. Effect of Zr and Sc on mechanical properties and electrical conductivities of Al wires. Transactions of Nonferrous Metals Society of China 2014; 24(10):3164-3169.

[26] Pozdniakov AV, Barkov RY. Microstructure and mechanical properties of novel Al-Y-Sc alloys with high thermal stability and electrical conductivity. Journal of Materials Science & Technology 2020; 36:1-6.

[27] Tie D, Wang Y, Wang X, Guan R, Yan L, Zhang J et al. Microstructure Evolution and Properties Tailoring of Rheo-Extruded Al-Sc-Zr-Fe Conductor via Thermo-Mechanical Treatment. Materials 2020; 13(4):845.

[28] Wang W, Pan Q, Lin G, Wang X, Sun Y, Wang X et al. Microstructure and properties of novel Al-Ce-Sc, Al-Ce-Y, Al-Ce-Zr and Al-Ce-Sc-Y alloy conductors processed by die casting, hot extrusion and cold drawing. Journal of Materials Science & Technology 2020; 58:155-170.

[29] Wang W, Pan Q, Lin G, Yu Y, Wang X, Liu Y et al. Internal friction and heat resistance of Al, Al–Ce, Al–Ce–Zr and Al–Ce–(Sc)–(Y) aluminum alloys with high strength and high electrical conductivity. Journal of Materials Research and Technology 2021; 14:1255-1274.

[30] Tie D, Zhang B, Chen M, Liu H, Wang Y, Liu L et al. Tailored Mechanical and Conductive Properties of Continuous Rheo-Extruded Al–Sc–Zr Alloy Conductors by Thermomechanical Treatment. MATERIALS TRANSACTIONS 2020; 61(2):412-415.

[31] Fuller C, Seidman D. Temporal evolution of the nanostructure of Al(Sc,Zr) alloys: Part II-coarsening of Al(ScZr) precipitates. Acta Materialia 2005; 53(20):5415-5428.

[32] Forbord B, Hallem H, Røyset J, Marthinsen K. Thermal stability of Al3 (Scx, Zr1− x)-dispersoids in extruded aluminium alloys. Materials Science and Engineering: A 2008; 475(1-2):241-248.

[33] Michi RA, De Luca A, Seidman DN, Dunand DC. Effects of Si and Fe micro-additions on the aging response of a dilute Al-0.08 Zr-0.08 Hf-0.045 Er at.% alloy. Materials Characterization 2019; 147:72-83.

[34] Dorin T, Babaniaris S, Jiang L, Cassel A, Race CP, Eggeman A et al. Stability and stoichiometry of L12 Al3 (Sc, Zr) dispersoids in Al-(Si)-Sc-Zr alloys. Acta Materialia 2021; 216:117117.

[35] Alabin AN, Belov NA, Effect of Iron and Silicon on Strength and Electrical Resistivity of Al-Zr Wire Alloys, Springer International Publishing, Cham, 2012, pp. 1539-1544.

[36] Shakiba M, Parson N, Chen XG. Effect of homogenization treatment and silicon content on the microstructure and hot workability of dilute Al–Fe–Si alloys. Materials Science and Engineering: A 2014; 619:180-189.

[37] Zhang Z, Li G, Chen X. Effect of nickel and vanadium on iron bearing intermetallic phases in AA 5657 simulated DC castings. Materials Science and Technology 2014; 30(8):951-961.

[38] Morozova A, Mogucheva A, Bukin D, Lukianova O, Korotkova N, Belov N et al. Effect of Si and Zr on the microstructure and properties of Al-Fe-Si-Zr alloys. Metals 2017; 7(11):495.

[39] Belov NA, Alabin AN, Eskin DG, Istomin-Kastrovskii VV. Optimization of hardening of Al–Zr–Sc cast alloys. Journal of Materials Science 2006; 41(18):5890-5899.

[40] Zhang Y, Gu J, Tian Y, Gao H, Wang J, Sun B. Microstructural evolution and mechanical property of Al–Zr and Al–Zr–Y alloys. Materials Science and Engineering: A 2014; 616:132-140.

[41] Khangholi SN, Javidani M, Maltais A, Chen X-G. Effects of natural aging and pre-aging on the strength and electrical conductivity in Al-Mg-Si AA6201 conductor alloys. Materials Science and Engineering: A 2021; 820:141538.

[42] Sauvage X, Murashkin MY, Valiev R. Atomic scale investigation of dynamic precipitation and grain boundary segregation in a 6061 aluminium alloy nanostructured by ECAP. Kovove Mater 2011; 49(1):11.

[43] Murayama M, Horita Z, Hono K. Microstructure of two-phase Al–1.7 at% Cu alloy deformed by equal-channel angular pressing. Acta Materialia 2001; 49(1):21-29.

[44] Fischer FD, Svoboda J, Appel F, Kozeschnik E. Modeling of excess vacancy annihilation at different types of sinks. Acta Materialia 2011; 59(9):3463-3472.

[45] Chen X, Kim D, Marioara CD, Andersen SJ, Lervik A, Holmestad R et al. Effect of pre-deformation on age-hardening behaviors in an Al-Mg-Cu alloy. Materials Science and Engineering: A 2021; 820:141557.

[46] Fazeli F, Sinclair C, Bastow T. The role of excess vacancies on precipitation kinetics in an Al-Mg-Sc alloy. Metallurgical and Materials Transactions A 2008; 39:2297-2305.

[47] Yang C, Cheng P, Chen B, Zhang J, Liu G, Sun J. Solute clusters-promoted strength-ductility synergy in Al-Sc alloy. Journal of Materials Science & Technology 2022; 96:325-331.

[48] Knipling KE, Dunand DC, Seidman DN. Criteria for developing castable, creep-resistant aluminum-based alloys–A review. International Journal of Materials Research 2022; 97(3):246-265.

[49] Vlach M, Stulíková I, Smola B, Kekule T, Kudrnova H, Kodetova V et al. Annealing effects in hot-deformed Al-Mn-Sc-Zr alloys. Kovove Mater 2015; 53:295-304.

[50] Lefebvre W, Danoix F, Hallem H, Forbord B, Bostel A, Marthinsen K. Precipitation kinetic of Al3 (Sc, Zr) dispersoids in aluminium. Journal of Alloys and Compounds 2009; 470(1-2):107-110.

[51] Vlach M, Cizek J, Melikhova O, Stulikova I, Smola B, Kekule T et al. Early stages of precipitation process in Al-(Mn-) Sc-Zr alloy characterized by positron annihilation. Metallurgical and Materials Transactions A 2015; 46:1556-1564.

[52] Forbord B, Lefebvre W, Danoix F, Hallem H, Marthinsen K. Three dimensional atom probe investigation on the formation of Al3 (Sc, Zr)-dispersoids in aluminium alloys. Scripta materialia 2004; 51(4):333-337.

[53] Tolley A, Radmilovic V, Dahmen U. Segregation in Al3(Sc,Zr) precipitates in Al–Sc–Zr alloys. Scripta Materialia 2005; 52(7):621-625.

[54] Fuller C, Murray J, Seidman D. Temporal evolution of the nanostructure of Al(Sc,Zr) alloys: Part I – Chemical compositions of Al(ScZr) precipitates. Acta Materialia 2005; 53(20):5401-5413.

[55] Du G, Deng J, Wang Y, Yan D, Rong L. Precipitation of (Al, Si) 3Sc in an Al–Sc–Si alloy. Scripta Materialia 2009; 61(5):532-535.

[56] Beeri O, Dunand DC, Seidman DN. Roles of impurities on precipitation kinetics of dilute Al–Sc alloys. Materials Science and Engineering: A 2010; 527(15):3501-3509.

[57] Booth-Morrison C, Mao Z, Diaz M, Dunand D, Wolverton C, Seidman D. Role of silicon in accelerating the nucleation of Al3 (Sc, Zr) precipitates in dilute Al–Sc–Zr alloys. Acta Materialia 2012; 60(12):4740-4752.

[58] Guan R-g, Jin H-m, Jiang W, Wang X, Wang Y-x, Li Z et al. Quantitative contributions of solution atoms, precipitates and deformation to microstructures and properties of Al–Sc–Zr alloys. Transactions of Nonferrous Metals Society of China 2019; 29(5):907-918.

[59] Jones M, Humphreys F. Interaction of recrystallization and precipitation: The effect of Al3Sc on the recrystallization behaviour of deformed aluminium. Acta materialia 2003; 51(8):2149-2159.

[60] Zhang Q, Guo F, Li Z. Influence of boronization treatment on the contents of Ti and V and properties of electrical aluminum. Foundry Technology 2007; 28(10):1338.

[61] Cui X, Wu Y, Liu X, Zhao Q, Zhang G. Effects of grain refinement and boron treatment on electrical conductivity and mechanical properties of AA1070 aluminum. Materials & Design 2015; 86:397-403.

[62] Ye H, Cui X, Cui H, Li X, Zhu Z, Pan Y et al. Study about improving mechanism of electrical conductivity of AA1070Al treated by a novel composite boron treatment with trace Ti. Journal of Alloys and Compounds 2021; 870:159416.

Chapter 3

Thermal stability of Al-Zr-Sc conductor alloys during long-term elevated-temperature exposures

(This article is published in: Journal of Materials Research and Technology
Volume 35, March–April 2025, Pages 164-175)

Abstract

Four Al-Zr-Sc conductor alloys with 0.1–0.18 wt.% Zr and 0.1–0.15 wt.% Sc were processed through casting, hot rolling, heat treatments, and cold wire drawing. The mechanical properties and electrical conductivities of the alloy wires were evaluated, and the microstructures were characterized using scanning electron microscopy, transmission electron microscopy, and electron backscattering diffraction techniques. The thermal stabilities of these alloys were systematically assessed during thermal exposures at 310, 350, and 400 °C for up to 1000 h. The ultimate tensile strengths (UTSs) of four Al-Zr-Sc alloy wires reached 206–214 MPa, while the electrical conductivities were 57%–57.5% IACS. All four alloy wires were strengthened by a large number of $Al_3(Sc,Zr)$ nanoprecipitates. With the increase in Zr or Sc content, the UTS only slightly increased, which shows a low impact of the Zr and Sc levels on the tensile strength and electrical conductivity. Notably, remarkable reduction in tensile strength and change in the deformed grain structure were not observed for the four alloy wires during thermal exposure at 310 °C for up to 1000 h. After thermal exposure at 350 °C for 200 h, all four wires still exhibited excellent thermal stabilities. With prolonged exposures at 350 and 400 °C, the alloy wires became unstable. The high-Zr-content Al-0.18Zr-0.1Sc and Al-0.18Zr-0.15Sc alloys exhibited better thermal

stabilities after long-term thermal exposures at 350 and 400 °C. This study on the thermal stability of Al-Zr-Sc conductor alloys under extreme conditions provides a valuable reference for industrial applications of thermally resistant Al conductor wires.

Keywords: Al-Zr-Sc alloys, thermal stability, $Al_3(Sc,Zr)$ nanoprecipitates, mechanical properties, electrical conductivity..

3.1 Introduction

With the rapid increase in the global demand for electricity in recent years [1], the current load capacity of long-distance power transmission lines has to be significantly increased. The current load significantly affects the arc-erosion behavior of electrical contact materials [2] which could be enhanced by adding metal oxides and optimizing the fabrication parameters [3, 4]. The increased temperature of aluminum conductor wires can lead to recrystallization, which degrades their mechanical properties and deteriorates the overall performance and reliability of transmission lines [5-7]. Thermal stability refers to a material's ability to maintain its properties and resist degradation upon a prolonged exposure at elevated temperatures [8]. The thermal stability of aluminum alloys can be divided into three categories based on the service temperature. Stability at moderate temperatures typically refers to conditions up to 100 °C. For example, Al-Cu-Mg-Ag alloys with excellent creep properties are used for the fuselage of supersonic transport aircrafts for the temperature range of 70 to 85 °C [9]. The medium temperature range, which necessitates thermal stability, encompasses temperatures up to 200 °C. This includes impellers used in generators and turbochargers operating within a service temperature range of 150 to 180 °C. For example, Al-Cu-Mg-Fe-Ni alloys exhibit excellent heat resistances under such conditions [10]. On the other hand, it is challenging to achieve thermal stability of aluminum alloys for high-temperature exposures up to 400 °C [11-14].

Al-Mg-Si conductor alloys are widely used in overhead transmission lines owing to their high strength, excellent electrical conductivity, and good corrosion resistance. The high strength is primarily derived from the precipitation of hardening particles from supersaturated solid solutions during aging, which act as obstacles to dislocation movement [15]. However, Al-Mg-Si conductors typically lose the strength at elevated temperatures above 200 °C owing to a significant precipitation coarsening [16]. Al-Mg-Si alloys retain only approximately 75% of their initial hardness after exposure at 230 °C for only 3 h [17]. Therefore, their insufficient thermal stability limits their application at elevated temperatures. Alloying elements with low diffusivities and low solubilities in the Al matrix are advantageous as long as their addition can introduce anti-coarsening strengthening nanoparticles [18-20]. Al-Zr and Al-Sc alloys can generate nanoscale Al_3Zr and Al_3Sc precipitates, which have a high coarsening resistance to enhance the strength at high temperatures. Some researchers have focused on development of Al-Zr and Al-Sc alloys with good thermal resistances [21]. Owing to the low diffusivity of Zr in the Al matrix, Al_3Zr particles are very stable at high temperatures. For example, an Al-0.25 wt.% Zr alloy does not exhibit significant decrease in the hardness even after 150 h at 400 °C [22]. The introduction of 0.4–0.6% Zr in aluminum not only maintains the strain hardening but also improves the mechanical properties through secondary precipitates of $L1_2$-Al_3Zr with an average size of 10 nm [23]. The combination of Zr and Sc in Al-Zr-Sc alloys is crucial for high-temperature applications owing to their high strength and good creep resistance at elevated temperatures [24, 25]. The strength and thermal stability of Al-Zr-Sc alloys are significantly higher than those of alloys with an individual addition of Zr and Sc. Compared to pure Al, the ultimate tensile strengths (UTSs) of Al-0.16Zr, Al-0.16Sc, and Al-0.12Sc-0.04Zr alloys increased by 16.7%, 161.9%, and 281%, respectively [26]. The strength of an Al-0.35Sc-0.2Zr alloy decreases very slowly, even after 100 h of exposure at 400 °C [27]. The excellent thermal stability of Al-Zr-Sc alloys is attributed to the precipitation of Al_3(Sc, Zr) nanoparticles, which have a core–shell structure with a Sc-enriched core surrounded by a Zr-enriched shell [24, 28-30]. The specific structure of Al_3(Sc, Zr) nanoparticles provides a high coarsening resistance and exceptional stability at high temperatures [31-33].

The purpose of this study was to systematically investigate the thermal stability of Al-Zr-Sc alloys with varying Zr and Sc contents during long-term thermal exposures at three different temperatures (310, 350, and 400 °C) for up to 1000 h. The evolutions of mechanical strength and electrical conductivity during thermal exposures were evaluated. Additionally, the precipitation microstructures and grain structures under different thermal exposure conditions were studied using transmission electron microscopy (TEM) and electron backscatter diffraction (EBSD) analyses.

3.2 Experimental procedure

3.2.1 Materials preparation

Four alloys with different Zr and Sc contents were prepared using a commercially pure 99.85% Al with Al-2%Sc, Al-15%Zr, Al-25%Fe, and Al-50%Si master alloys. All chemical compositions of the alloys are indicated in wt.% in this paper. For each alloy, 5 kg of materials was melted in a SiC crucible using an electrical resistance furnace at 750 °C. The addition of the master alloys was then kept for 3 h at this temperature to ensure a complete dissolution. The liquid metal was poured into a Y-shaped permanent steel mold preheated to 400 °C to obtain rectangular cast ingots with dimensions of 30 × 40 × 80 mm^3. To examine the effect of Zr, alloys E, F, and G were designed with a fixed low Sc content of 0.10% but with different Zr contents of 0.10, 0.13, and 0.18%, respectively. Alloy H, with the same Zr content as alloy G (0.18%), included a higher Sc content of 0.15% to assess the influence of Sc on the thermal stability of Al-Zr-Sc alloys. The actual chemical compositions of the alloys analyzed by optical emission spectroscopy are listed in Table 3-1.

Table 3-1 Nominal and actual chemical compositions of the alloys (wt.%).

Alloy	Nominal composition	Actual chemical composition				
		Si	Fe	Zr	Sc	Al
E	Al-0.1Zr-0.1Sc	0.26	0.32	0.10	0.09	Bal.
F	Al-0.13Zr-0.1Sc	0.27	0.3	0.13	0.11	Bal.
G	Al-0.18Zr-0.1Sc	0.25	0.31	0.18	0.10	Bal.
H	Al-0.18Zr-0.15Sc	0.27	0.29	0.18	0.15	Bal.

The thermomechanical processing route of all Al-Zr-Sc alloys included hot rolling, heat treatments, cold wire drawing, and annealing, as shown in Figure 3-1. Hot rolling was performed using a laboratory-scale mill for multiple passes at 550 °C. The rolling process started with a 26.5-mm-thick ingot and ended with an 8-mm-thick strip, with a reduction of ~68%. Subsequently, the rolled strips were cut and machined into square bars with dimensions of 6.7 mm × 6.7 mm for further processing. All heat treatments were conducted in an electric furnace, with a ramping rate of 100 °C/h. The samples after hot rolling were subjected to a solution treatment at 600 °C for 8 h, followed by quenching in water to achieve the supersaturated solid solution and aging treatment at 375 °C for 24 h to form the thermally stable $Al_3(Sc,Zr)$ precipitates. Cold wire drawing was conducted using a laboratory-scale mill to transfer the square bars to round wires with a diameter of 4.3 mm by several passes with a reduction of 68%. Subsequently, the wires were annealed at 350°C for 5 h to improve the electrical conductivity.

Figure 3-1 Thermomechanical processing route to produce aluminum wires.

All finished wires, which met the AT4 grade as specified by the international standard IEC 62004 [34], were subjected to long-term thermal exposures at 310 and 350 °C for up to 1000 h, and 400 °C for up to 400 h to evaluate the material thermal stabilities (Table 3-2). The mechanical properties after thermal exposures were evaluated by measuring the microhardness and tensile strength of the wires.

Table 3-2 Thermal exposure conditions.

Thermal exposure temperature (ºC)	Thermal exposure time (h)
310	100, 200, 400, 700, 1000
350	100, 200, 400, 700, 1000
400	10, 50, 100, 200, 400

3.2.2 Mechanical and electrical properties

Vickers microhardness was assessed using an NG-1000 CCD microhardness tester by applying a 25-g load for 15 s. Electrical conductivity (EC) was determined as a percentage of the international annealed copper standard (% IACS) using a Sigmascope SMP350 instrument based on the eddy current method. At least 15 measurements per sample condition were performed, and the average value was employed. Room-temperature tensile tests were conducted on wires with a diameter of 4.3 mm with a gauge length of 250 mm and strain rate of 25 mm/min using an Instron 8801 servo-hydraulic unit at room temperature. The results were obtained from three samples per condition.

3.2.3 Microstructures

The as-cast microstructures were examined using scanning electron microscopy (SEM, JEOL-6480LV). EBSD images were acquired with a scanning electron microscope (Hitachi, SU-70) equipped with a Symmetry S3 CMOS detector (Oxford Instruments). The EBSD samples were scanned at a tilt angle of 70° with a step size of 1 μm. All samples were sectioned parallel to the wire drawing direction, and the central region of the samples was observed. A post-EBSD analysis was conducted using the HKL Channel 5 software.

Bright-field and dark-field TEM images were obtained along the [001]Al zone axis using a transmission electron microscope (Jeol JEM-2100) operated at 200 kV. The TEM samples were prepared from the center of the cross sections of the wires. The characteristics of the precipitates were analyzed using the ImageJ image analysis software based on TEM images from three different microstructural fields, with four images per field. The number density N_V of $Al_3(Sc,Zr)$ precipitates was calculated by [35, 36]:

$$N_V = \frac{N}{A(D+t)} \qquad \text{Equation 1}$$

where N is the number of precipitates in the area, A is the total area, D is the average diameter of precipitates, and t is the thickness of the TEM foil of the local area. The foil thickness of each field was determined by the convergent electron beam diffraction method [37].

3.3 Results and discussion

3.3.1 As-cast microstructure

Figure 3-2 shows the distributions of intermetallic phases of the four alloys in the as-cast state. The as-cast microstructures of the four alloys were similar, and primarily consisted of an α-Al matrix with dispersed intermetallic phases (Figure 3-2a–d). The dominant intermetallic phases were Fe-rich intermetallics, including the skeleton-like α-Al_8Fe_2Si phase and, to a smaller extent, feather-like Al_mFe phase [7, 38], distributed along the dendrite boundaries. A small amount of spherical Sc-rich intermetallic particles randomly appeared in the α-Al matrix (Figure 3-2e). In alloys E, F, and G, the numbers of Sc-containing particles were small, but their number increased in alloy H. The diameter of such Sc-containing intermetallic particles ranges from 3 to 5 μm. Sc-containing intermetallic particles in the as-cast microstructures of Al-Zr-Sc alloys have been also previously reported [38, 39], with diffraction peaks corresponding to the Al_3Sc and Al_3Zr phases.

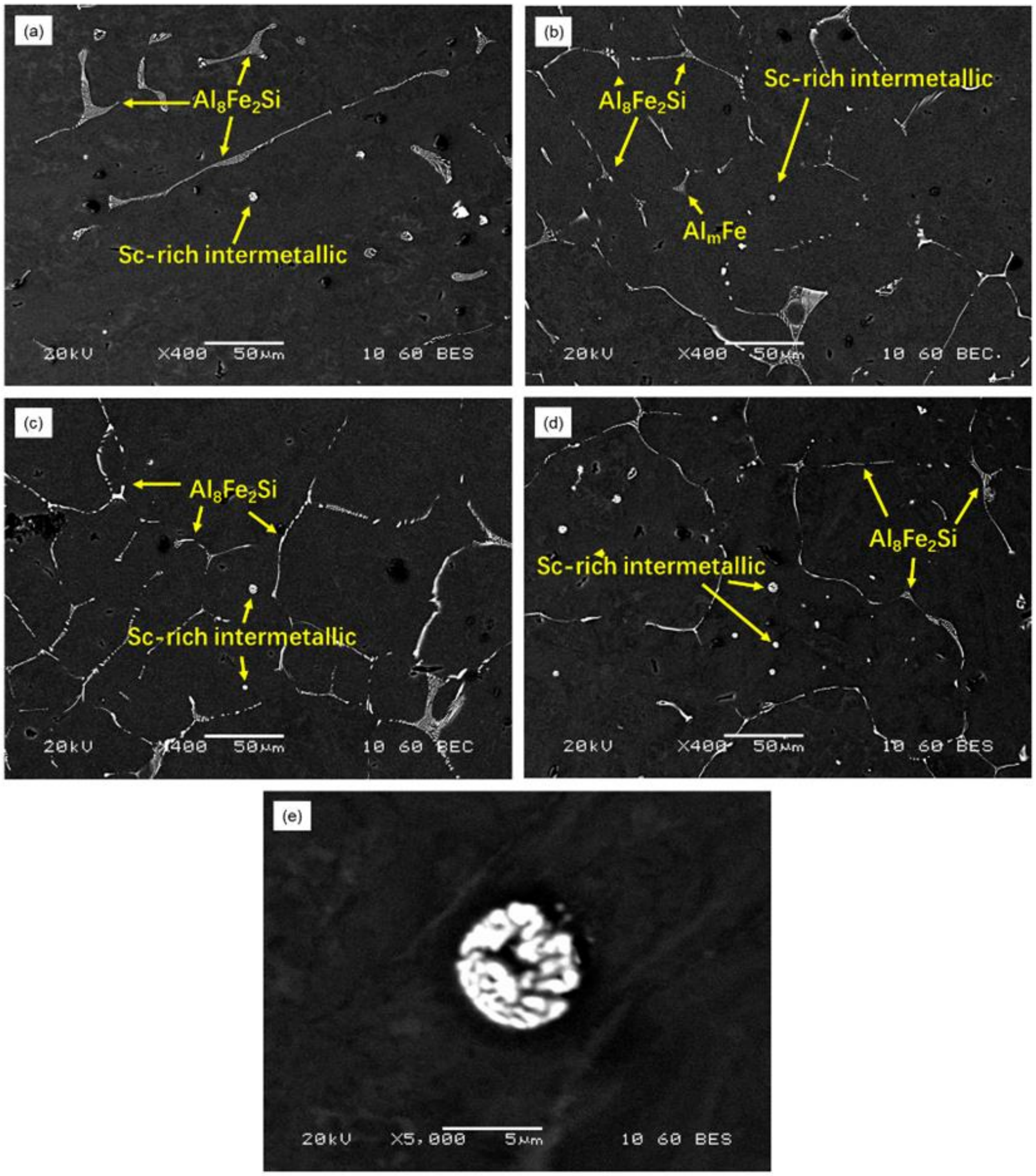

Figure 3-2 SEM images showing the as-cast microstructures of alloys (a) E, (b) F, (c) G, and (d) H alloys, and (e) enlarged image of a Sc-containing intermetallic particle in alloy H.

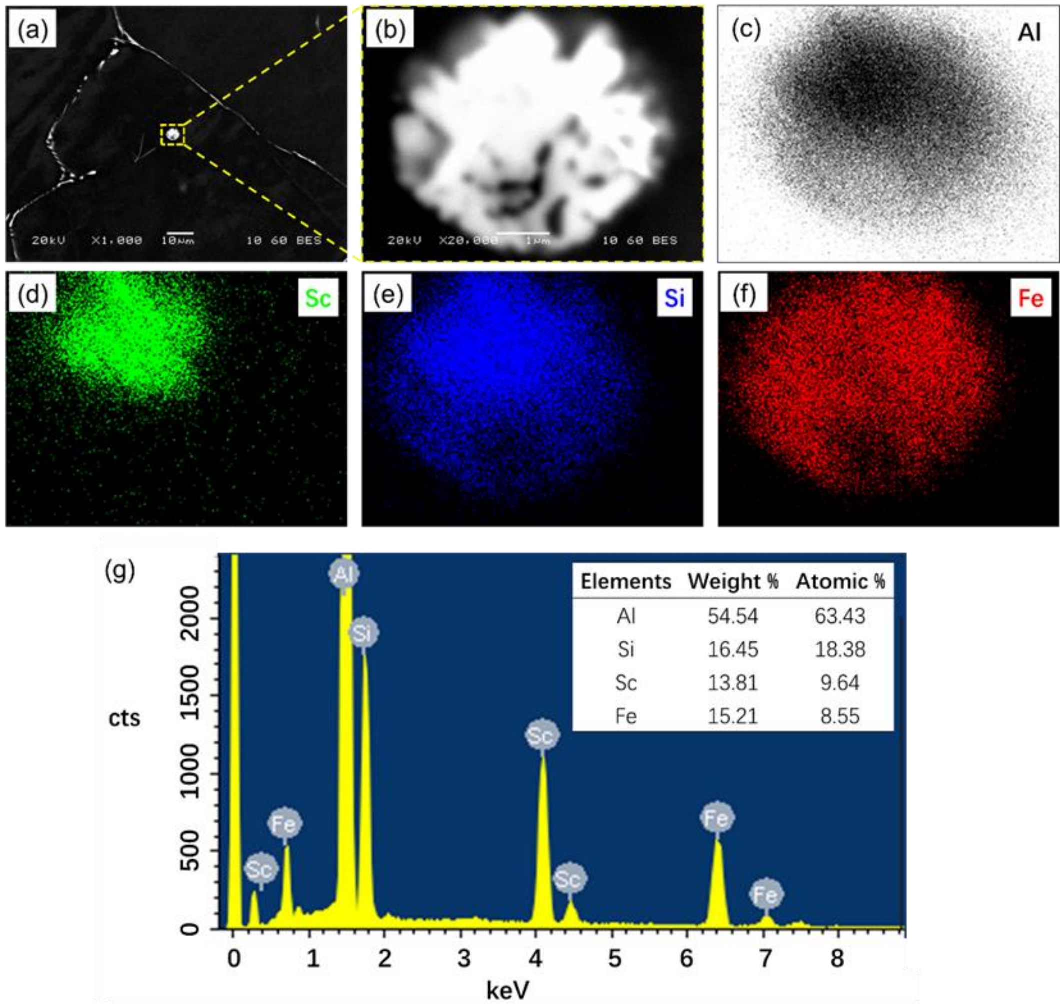

Figure 3-3 Characterization of the Sc-containing intermetallic phase: (a–f) SEM–EDS elemental mapping of a Sc-containing intermetallic particle and (g) corresponding EDS spectrum with the weight and atomic percentages of various elements.

The SEM-energy-dispersive spectroscopy (EDS) elemental mapping of a Sc-containing intermetallic particle and area EDS analysis are presented in Figure 3-3. The particle contained high levels of Sc, Si, and Fe (Figure 3-3d–f). The EDS analysis shows that the weight and atomic percentages of Sc in the spherical intermetallic particle were 13.8% and 9.6%, respectively (Figure 3-3g). This indicates the consumption of Sc atoms by forming such intermetallic particles during casting. To quantify the amount of Sc-rich intermetallic particles in the alloys, the area fraction of Sc-containing compounds was calculated by:

$$R_A = \frac{Area_{\text{Sc−rich intermetallic}}}{Area_{\text{All detection areas}}} \qquad \text{Equation 2}$$

The quantitative results of R_A for the four alloys are presented in Table 3-3 based on 10 images per alloy. The R_A values of alloys E, F, and G were almost at the same level, ranging from 2.32×10^{-4} to 2.82×10^{-4}. However, R_A of alloy H was higher, being 5.38×10^{-4}, roughly twice those of the other three alloys. This suggests that the higher Sc content in alloy H (0.15% *vs* 0.1% in the other three alloys) promoted the formation of the Sc-containing intermetallic particles in the as-cast microstructure, in which Sc cannot be fully used in the precipitation during aging.

Table 3-3 Area fraction of the Sc-containing intermetallic particles in four alloys.

Alloys	R_A ($\times 10^{-4}$)
E	2.32 ± 0.81
F	2.82 ± 0.59
G	2.45 ± 0.94
H	5.38 ± 1.05

3.3.2 Aging treatment

Figure 3-4 presents the evolutions of microhardness and EC as a function of the aging time at two temperatures for the four experimental alloys. Generally, the microhardness and EC increased after hot rolling relative to the as-cast state owing to the precipitation of some Sc/Zr-containing particles during hot rolling. This necessitated the solution heat treatment (SHT) before aging to dissolve Zr and Sc atoms into the aluminum matrix. The SHT resulted in large decreases in microhardness and EC compared to those after hot rolling. During aging at 350 °C (Figure 3-4a and b), both microhardness and EC significantly increased in the first 24 h, and then slowly increased from 24 to 96 h. Alloys G and H exhibited slightly higher HV values than alloys E and F with the increase in aging time up to 96 h (72.2 and 70.6 HV for alloys G and H vs 69.2 and 70 HV for alloys A and B, respectively). The ECs of all alloys were comparable after the aging for 48 h (57.2–57.4% IACS).

For the aging at 375 °C, the microhardness increased rapidly during the first 24 h, reaching its peak value. The microhardness then decreased gradually with the increase in the aging time up to 96 h (Figure 3-4c). The peak microhardness values of alloys E, F, G, and H were 71, 71.7, 72.9, and 73.8 HV, respectively, approximately 2.5 HV higher than those of the samples aged at 350 °C. The ECs of the alloys also increased during the first 24 h, and then reached a plateau (Figure 3-4d). The peak ECs after aging for 24 h were 57.5, 57.3, 57.4, and 57.6% IACS for alloys E, F, G, and H, respectively. Considering the benefits in terms of microhardness and EC at 375 °C, the aging at 375 °C for 24 h was selected as optimal for further thermal processing of cold wire drawing, as shown in Figure 3-1.

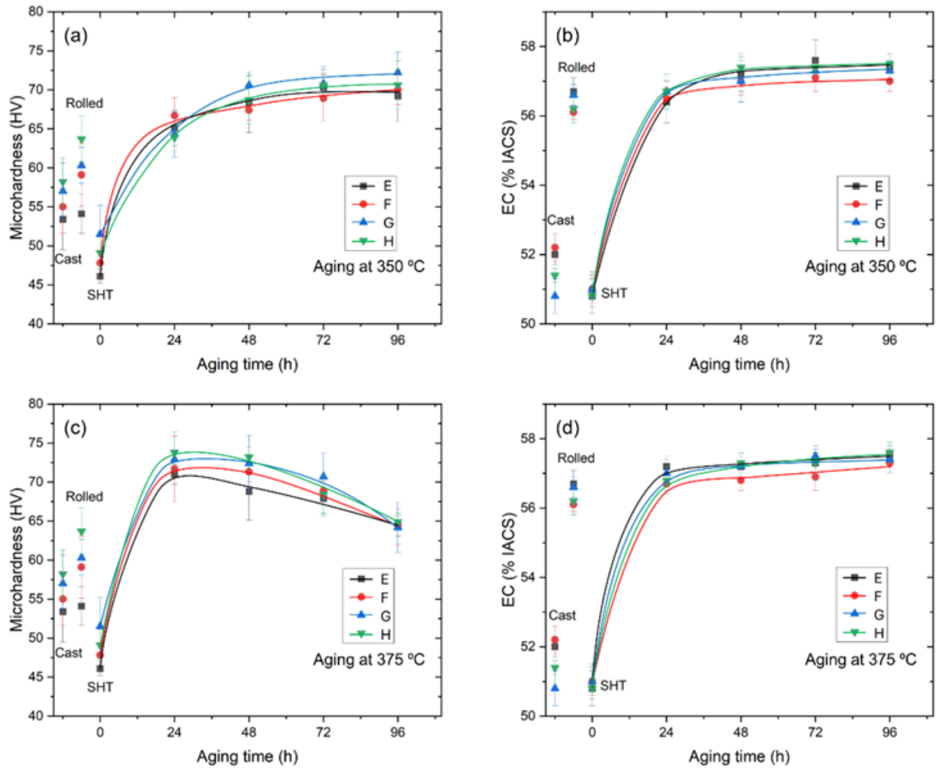

Figure 3-4 Effects of aging temperature and time on the microhardness and EC for the four alloys: (a, b) aging at 350 °C, (c, d) aging at 375 °C.

3.3.3 Mechanical properties and EC

Figure 3-5 presents the mechanical properties and EC of finished wires with a diameter of 4.3 mm after cold drawing and annealing. Alloys E, F, G, and H exhibited UTSs of 206, 208, 209, and 214 MPa, respectively, and ECs of 57.5, 57.2, 57.3, and 57.1% IACS, respectively. The elongations of the alloys ranged from 4.6% to 6.4%. In the three 0.1%Sc containing alloys, the Zr content increased from 0.1% in alloy E to 0.18% in alloy G. However, the UTS only slightly increased from 206 MPa in alloy E to 209 MPa in alloy G. This indicates that almost all Sc and Zr solutes in alloy E precipitated to form $Al_3(Sc,Zr)$

precipitates after aging and annealing treatments, which contributed to the precipitation strengthening. With the further increase in Zr content in alloys F and G, a very small strengthening effect was observed. Zr atoms facilitate the nucleation of $Al_3Sc(L1_2)$ precipitates, with Sc-Sc, Zr-Zr, and Sc-Zr dimers or larger clusters serving as nucleation sites for the formation of $L1_2$-$Al_3(Sc,Zr)$ precipitates [32, 40]. However, it seems that the higher Zr contents in alloys F and G did not bring further $Al_3(Sc,Zr)$ precipitation strengthening.

Alloy H with the highest Zr and Sc contents (Al-0.18Zr-0.15Sc) exhibited the highest UTS among the four alloys (214 MPa). However, this UTS was only slightly higher than that of alloy G (209 MPa), which contained the same amount of Zr but lower Sc level (Al-0.18Zr-0.10Sc). This suggests that the higher consumption of Sc in the primary Sc-rich intermetallic phase in alloy H (Table 3-3) decreased the usefulness of Sc in the precipitation strengthening of $Al_3(Sc,Zr)$ precipitates.

The ECs of the four alloys significantly exceeded the requirement of AT2 grade specified in the international standard IEC 62004 (55% IACS) [34], while the UTS of alloy H almost reached the AT2 grade (225 MPa). Additionally, the ECs of the four alloys almost approached the AT4 grade (58% IACS) with UTSs substantially surpassing the AT4 requirement (159 MPa) [4, 28]. The elongations of the four alloys also far exceeded the minimum requirements for both AT2 and AT4 grades (2%) [34]. These results demonstrate that the minor Sc addition in Al-Zr conductor alloys provided strong mechanical properties with excellent electrical conductivities, making them among the top-performing aluminum conductor alloys in this category.

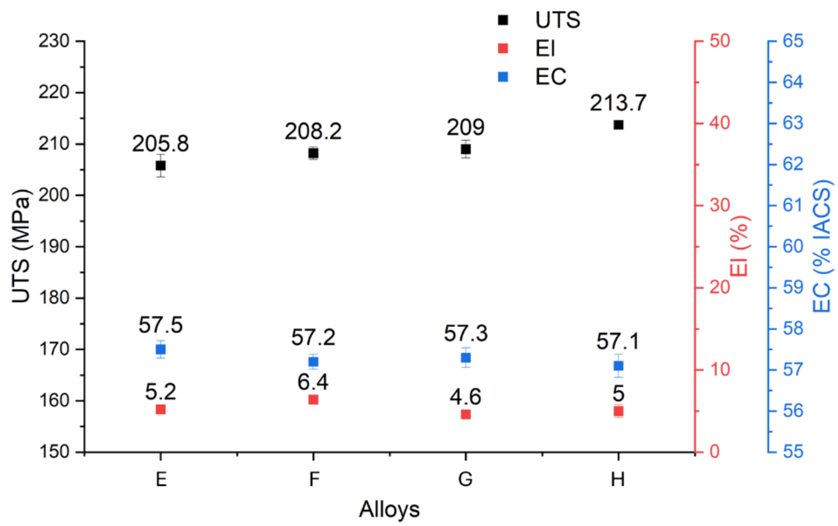

Figure 3-5 UTSs, elongations, and ECs of the four alloys.

3.3.4 Thermal stability

The thermal stabilities of the alloys were evaluated using microhardness measurements after long-term thermal exposures at three temperatures; the results are shown in Figure 3-6. Notably, no significant reductions in HV were observed for all alloys after thermal exposure at 310 °C for up to 1000 h. The reductions were only 4.4, 4.6, 1.9, and 2.7 HV for alloys E to H, respectively (Figure 3-6a). During the thermal exposure at 350 °C (Figure 3-6b), there was a slow gradual decrease in HV for all four alloys with the increase in exposure time. The reductions were slower for alloys G and H than for alloys E and F. After 1000 h of exposure, the reductions were 22.6 and 22.1 HV for alloys E and F, respectively, but 12.7 and 13.1 HV for alloys G and H, respectively. Under the extreme condition during the thermal exposure at 400 °C, the HV values of all four alloys rapidly decreased within the first 50 h (Figure 3-6c). Beyond 50 h, alloys G and H exhibited slower decreases in HV up to 400 h than alloys E and F. The maximum reductions after 400 h of exposure were 28 and 29.6 HV for alloys E and F, respectively, compared to 25 and 23.2 HV for alloys G and H, respectively.

The thermal stabilities of the alloys were further investigated by tensile tests after thermal exposures at the three abovementioned temperatures for selected times (Figure 3-7). The results are consistent with the microhardness measurements. During the thermal exposure at 310 °C (Figure 3-7a), almost no changes occurred in the UTSs of all four alloys. The reductions in UTSs even after 1000 h were below 2%, which shows the excellent thermal stability at 310 °C for all four alloys, which is in line with previous studies [7, 29]. During the initial 200 h of exposure at 350 °C, only slight decreases in the UTSs ranging from 4 to 10 MPa were observed for the four alloys (Figure 3-7b). The reductions in UTSs were within 5%, which shows the excellent thermal stability during a medium-term thermal exposure at 350 °C. With prolonged exposures to 400 and 1000 h, the reductions in UTS rapidly increased above 20% (Figure 3-7d), resulting in a deteriorated thermal stability during a long-term exposure. Alloys G and H exhibited better thermal stabilities after the long-term thermal exposure (400–1000 h) at 350 °C than alloys E and F. The reduction rates of UTSs of alloys G and H were lower than those for alloys E and F. Upon the exposure at 400 °C, the tensile strengths of all four alloys became unstable. During the first 50 h of exposure, the reductions in UTSs already reached approximately 30–40% (Figure 3-7e). The reductions continuously increased with the exposure time to 200 h, but slowed when the exposure time further increased from 200 to 400 h.

As shown in Figure 3-7d and e, alloys G and H with a high Zr content (0.18%) exhibited better thermal stabilities after the long-term thermal exposures at 350 and 400 °C than alloys E and F with lower Zr contents (0.1% and 0.13%, respectively). For example, the reductions in UTSs were 24% for alloys G and H, and 36% for alloys E and F after the thermal exposure at 350 °C for 1000 h. However, at the same high level of Zr, alloy H with a higher Sc content (0.15%) was not advantageous in terms of thermal stability over alloy G with a lower Sc content (0.1%). For example, the reductions in UTSs after thermal exposures at 350 °C for 400 h and 400 °C for 200 h were ~ 20% and ~ 32% for alloys G and H, respectively, which were almost equal for both alloys under two different exposure conditions (Figure 3-7d and e).

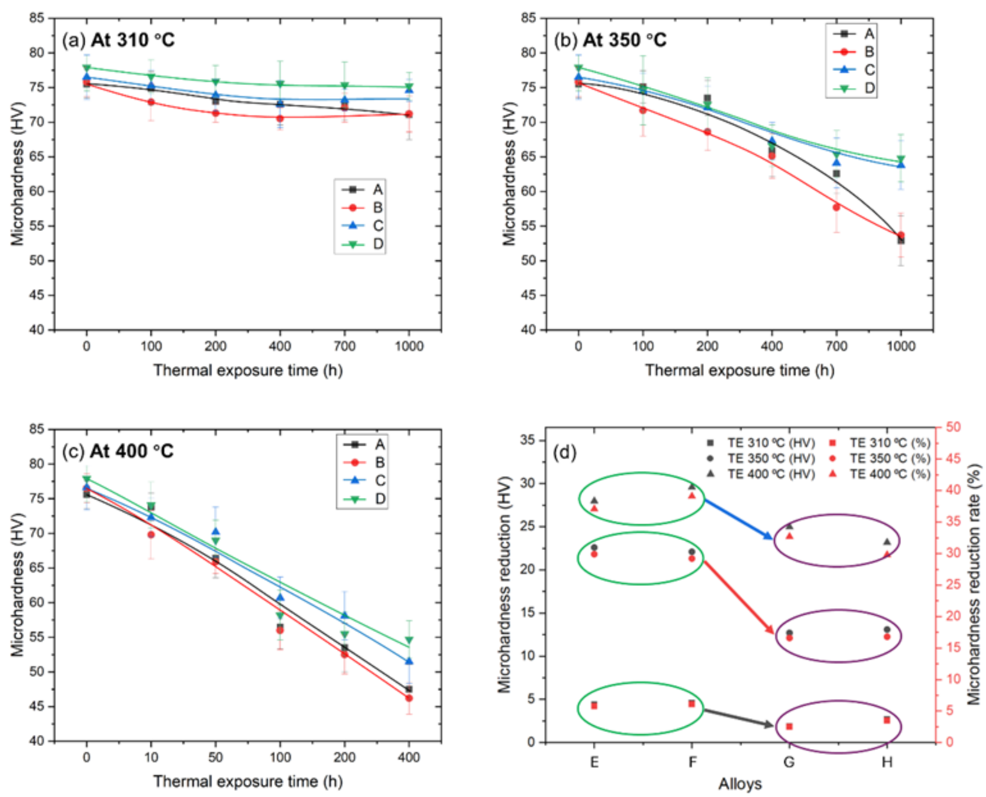

Figure 3-6 Evolution of the microhardness of alloy wires during thermal exposures as a function of the exposure time at (a) 310, (b) 350, and (c) 400 °C. (d) Microhardness reductions after the longest thermal exposure.

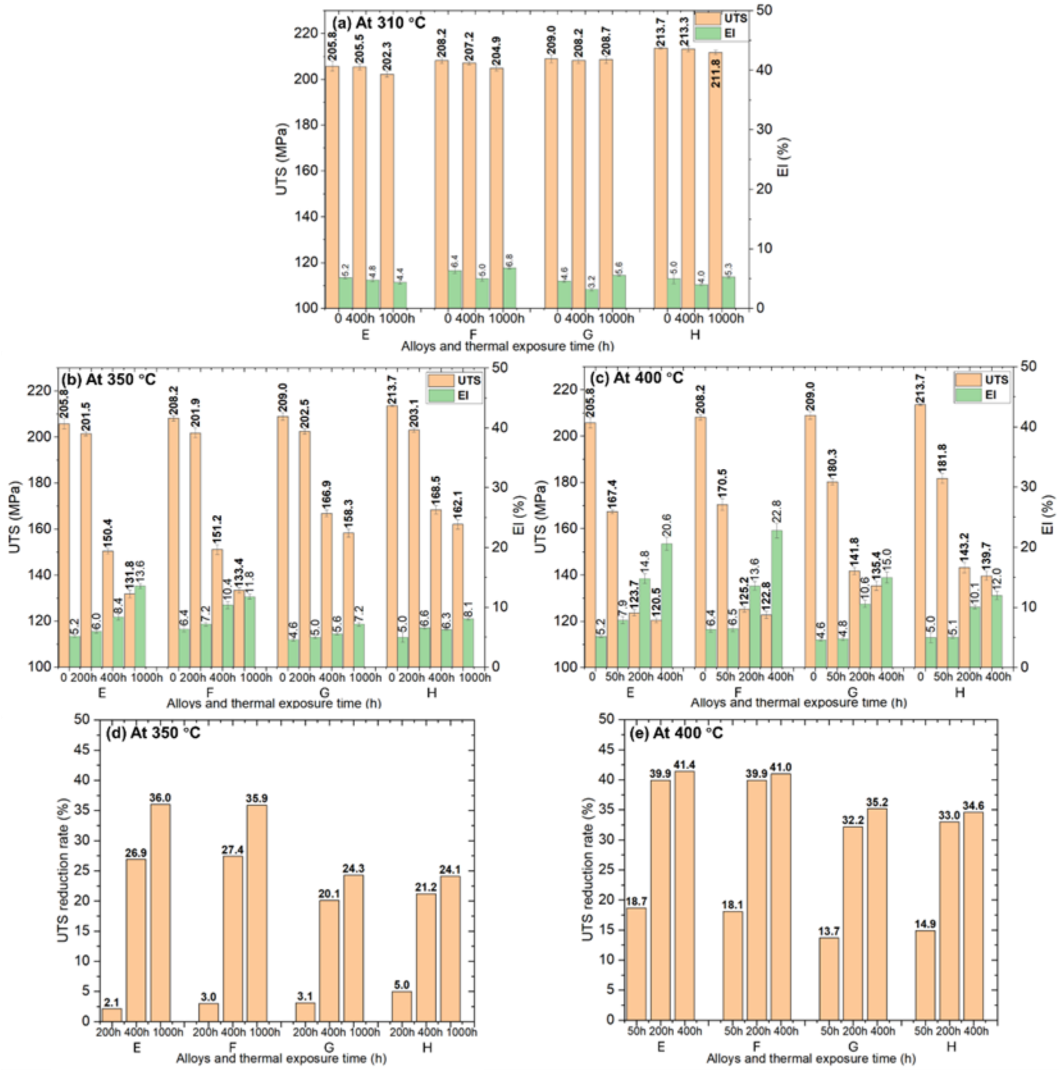

Figure 3-7 Evolutions of UTS and elongation of alloy wires during thermal exposures as a function of the exposure time at (a) 310, (b) 350, and (c) 400 °C. Reductions in UTSs at (d) 350 and (e) 400 °C.

3.4.5 Microstructure evolution during thermal exposure

TEM observations of the four alloy wires before thermal exposure are shown in Figure 3-8. After the cold wire drawing and annealing, a large number of $Al_3(Sc,Zr)$ nanoprecipitates were uniformly distributed in the Al matrix in all four alloys, as shown in the dark-field images (Figure 3-8a, d, g, and j). Figure 3-8b, e, h, and k present the corresponding selected-area electron diffraction patterns (SAEDPs) along the [001]Al zone axis, showing reflections from $Al_3(Sc,Zr)$ precipitates [7, 41, 42]. The quantitative results of the precipitate characteristics are presented in Table 3-4. With the increase in Zr content from 0.1% to 0.18% in the three 0.1%Sc-containing alloys E to H, the number density of $Al_3(Sc,Zr)$ precipitates only slightly increased from 1.15×10^{22} to 1.25×10^{22} m^{-3}, and the precipitate diameters remained similar in the three alloys (5.2–5.5 nm), which explains the almost negligible strengthening effect of Zr on the tensile strength, where the UTS slightly increased from 205.8 MPa for alloy E to 208.2 MPa for alloy F, and further to 209 MPa for alloy G (Figure 3-5).

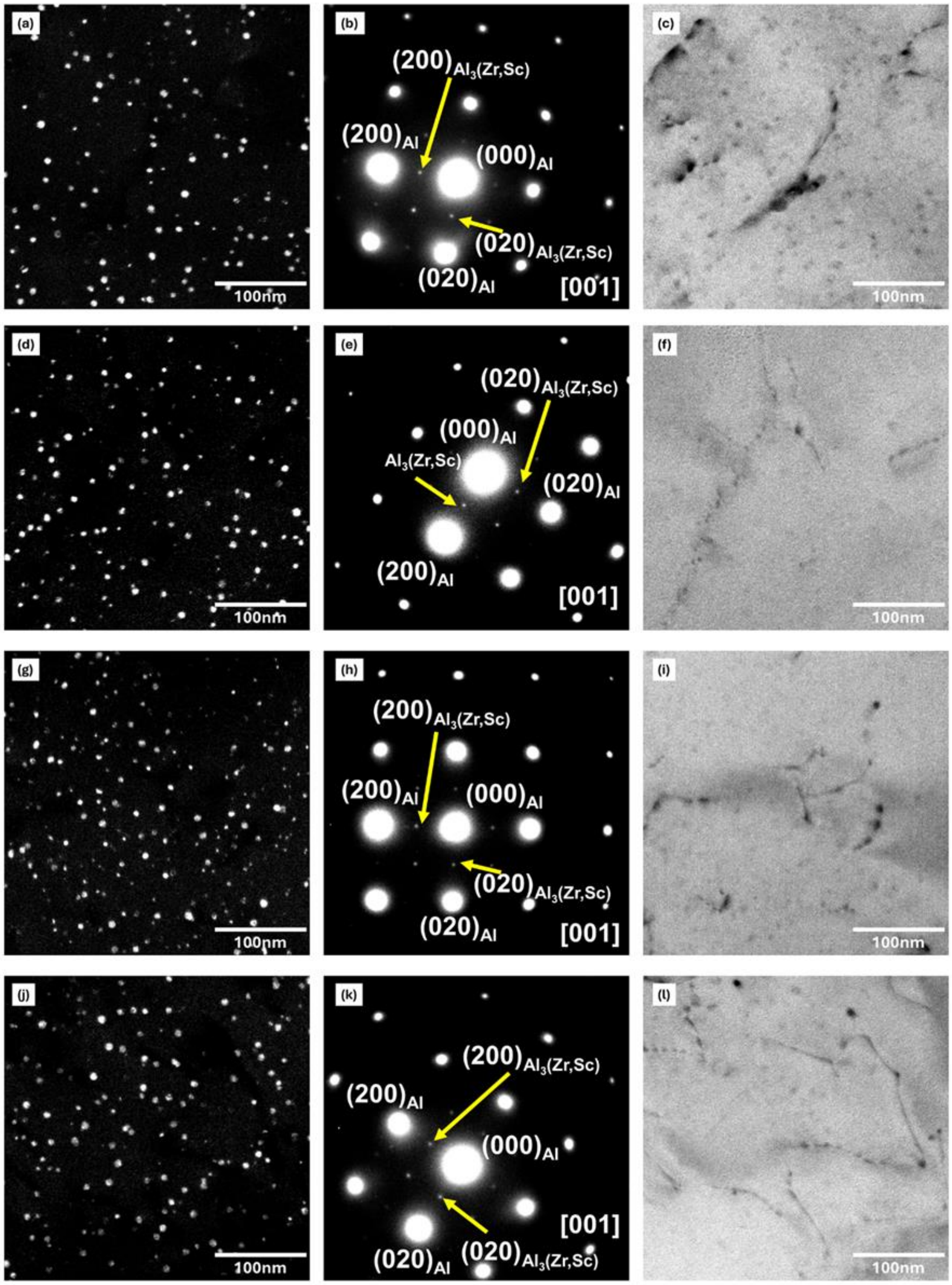

Figure 3-8 Dark-field TEM images of the four alloy wires before thermal exposure, showing the $Al_3(Sc,Zr)$ precipitates and their corresponding SAEDPs: (a, b) alloy E, (d, e) alloy F, (g, h) alloy G, and (j, k) alloy H. Bright-field TEM images showing the dislocations pinned and tangled by $Al_3(Sc,Zr)$ precipitates: (c) alloy E, (f) alloy F, (i) alloy G, and (l) alloy H.

Although the Sc content was increased to 0.15% in alloy H (Al-0.18%Zr-0.15%Sc), the number density of $Al_3(Sc,Zr)$ precipitates was only slightly higher compared to that of its counterpart alloy G (Al-0.18%Zr-0.10%Sc, 1.36×10^{22} m^{-3} vs 1.25×10^{22} m^{-3}, Table 3-4). This suggests that the high Sc content in alloy H does not largely increase the amount of $Al_3(Sc,Zr)$ precipitates, owing to the consumption of Sc in the primary Sc-rich intermetallic phase during casting. This explains the slight increase in the tensile strength for alloy H relative to alloy G (UTS: 214 MPa vs 209 MPa, Figure 3-5). The bright-field images in Figure 3-8c, f, i, and l were captured at the same locations as the corresponding dark-field images. Owing to the $Al_3(Sc,Zr)$ nanoprecipitates, several dislocations were pinned and tangled during the cold wire drawing and annealing.

Figure 3-9 shows the precipitation microstructures of alloys E and G, as examples, after the long-term thermal exposures at 310, 350, and 400 °C. The characteristics of the precipitates are listed in Table 3-4. After the thermal exposure at 310 ºC for 1000 h (Figure 3-9a and d), the large number of fine $Al_3(Sc,Zr)$ precipitates remained almost unchanged in both alloys E and G. As shown in Table 3-4, the number densities of the precipitates of alloys E and G after the thermal exposure were 1.04×10^{22} and 1.19×10^{22} m^{-3}, respectively, slightly decreased compared to those before the thermal exposure (1.15×10^{22} and 1.25×10^{22} m^{-3}, respectively). The diameters of the precipitates before and after the thermal exposure were similar.

After the thermal exposure at 350 ºC for 1000 h (Figure 3-9b and e), the precipitates became coarsened in alloys E and G. For example, the number density and diameter of the precipitates in alloy E were 1.15×10^{22} m^{-3} and 5.2 nm before the thermal exposure, and became 0.84×10^{22} m^{-3} and 6.8 nm after the thermal exposure, respectively. However, alloy

G contained a higher number density of precipitates (0.96×10^{22} m^{-3}) with a smaller diameter (6 nm) than alloy E.

Under the severe thermal exposure conditions at 400 °C for 400 h, the precipitates in both alloys remarkably coarsened (Figure 3-9c and f), and thereby had lower number densities and larger diameters of $0.41–0.46 \times 10^{22}$ m^{-3} and 8.8–9.7 nm compared to $1.15–1.25 \times 10^{22}$ m^{-3} and 5.2–5.4 nm before the thermal exposure in alloys E and G, respectively (Table 3-4). Alloy G still had a higher number density and smaller diameter of precipitates than alloy E after the thermal exposure. The high-Zr-content alloy G (Al-0.18%Zr-0.10%Sc) exhibited a better thermal stability than the low-Zr-content alloy E (Al-0.10%Zr-0.10%Sc) in terms of the resistance of the precipitate coarsening after the long-term thermal exposures at 350 and 400 °C. Additionally, the evolution and coarsening of precipitates under different thermal exposure conditions are consistent with the changes in the microhardness and UTS (Figure 3-6 and 7).

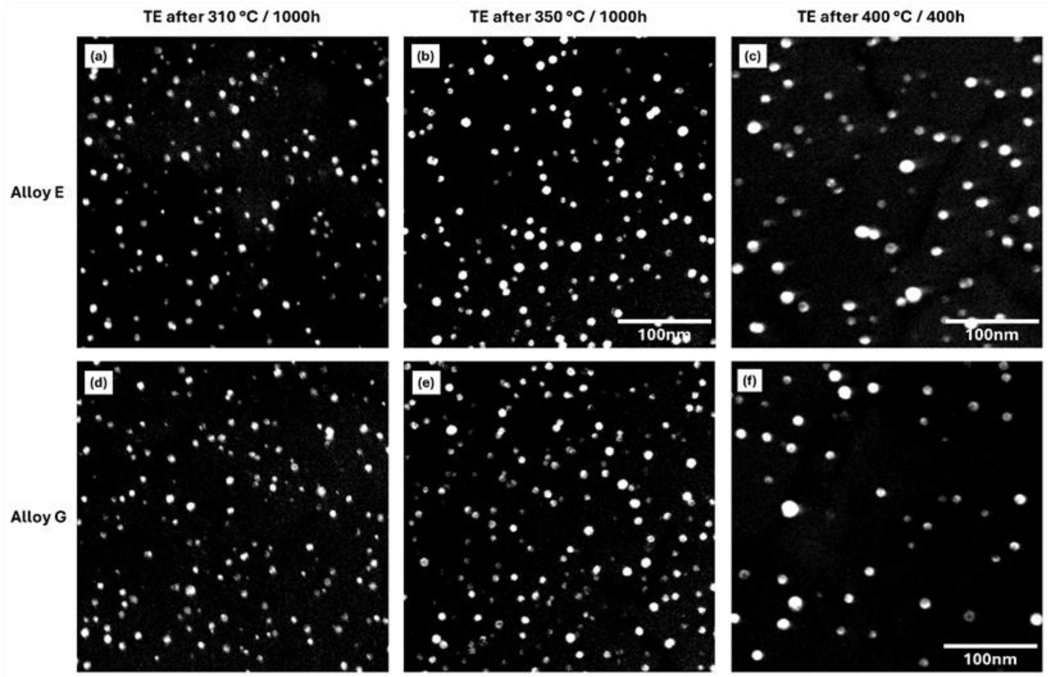

Figure 3-9 Dark-field TEM images of alloys E and G after long-term thermal exposures: (a, b, c) alloy E after 310 ºC/1000 h, 350 ºC/1000 h, and 400 ºC/400 h, respectively, (d, e f) alloy G after 310 ºC/1000 h, 350 ºC/1000 h, and 400 ºC/400 h, respectively.

Table 3-4 Characteristics of the precipitates in the experimental alloys.

	Alloys	N_v (× 10^{22} m^{-3})	D (nm)
Before TE	E	1.15 ± 0.13	5.2 ± 1.3
	F	1.18 ± 0.21	5.5 ± 0.9
	G	1.25 ± 0.09	5.4 ± 1.1
	H	1.36 ± 0.15	5.5 ± 1.2
TE after 310 °C / 1000h	E	1.04 ± 0.18	5.4 ± 0.9
	G	1.19 ± 0.11	5.5 ± 1.2
TE after 350 °C / 1000h	E	0.84 ± 0.15	6.8 ± 1.5
	G	0.96 ± 0.26	6 ± 1.3
TE after 400 °C / 400h	E	0.46 ± 0.13	9.7 ± 2.1
	G	0.41 ± 0.09	8.8 ± 1.9

Note: TE refers to thermal exposure.

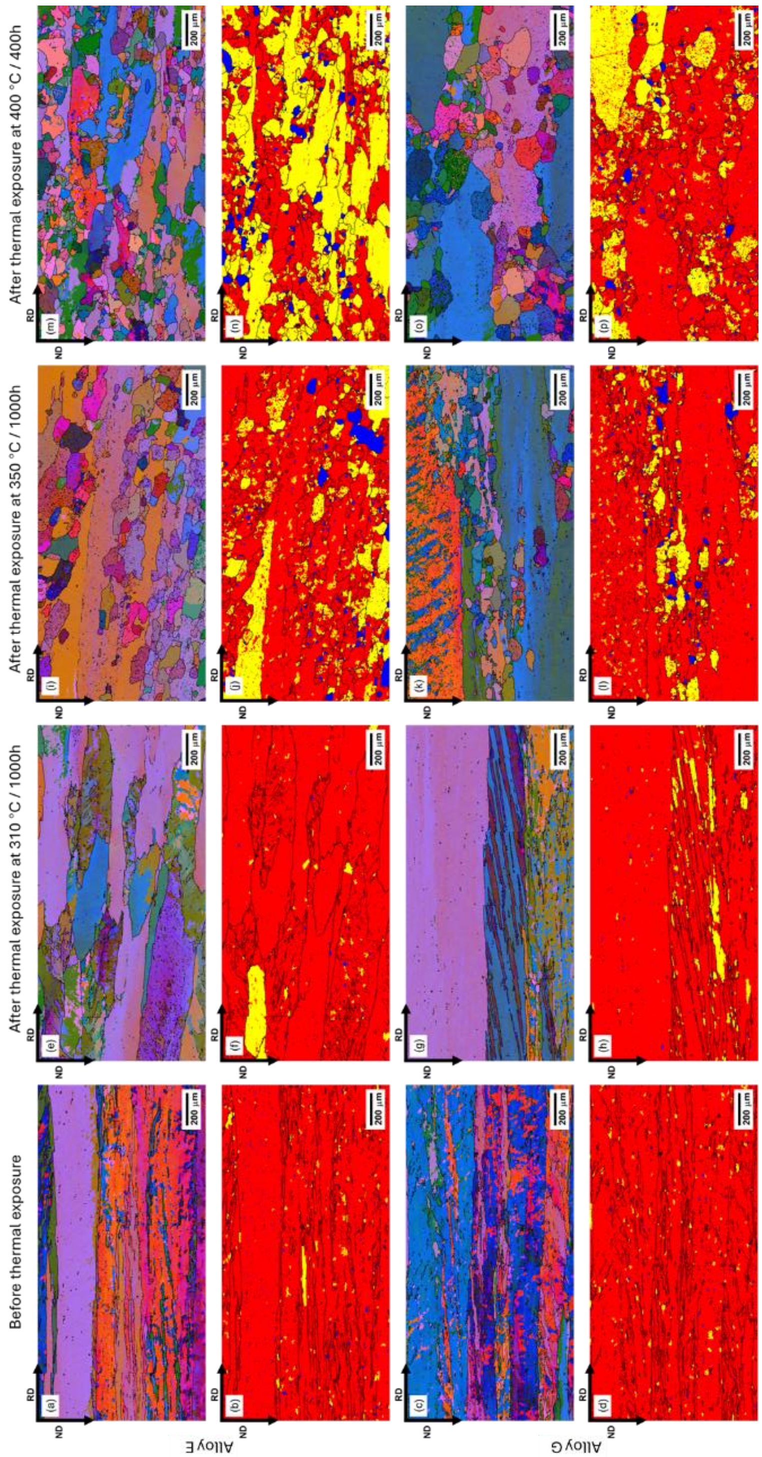

Figure 3-10 All-Euler orientation and GOS maps under different thermal exposure conditions: (a, b) and (c, d) before the thermal exposure of alloys E and G, (e, f) and (g, h) after the thermal exposure at 310 ºC/1000 h for alloys E and G, (i, j) and (k, l) after the thermal exposure at 350 ºC/1000 h for alloys E and G, and (m, n) and (o, p) after the thermal exposure at 400 ºC/400 h for alloys E and G, respectively.

All-Euler orientation and grain orientation spread (GOS) maps of alloys E and G under various thermal exposure conditions are presented in Figure 3-10. The deformed, substructured, and recrystallized grains in the GOS maps are shown in red, yellow, and blue, respectively. The statistical distribution of different grain structures, as determined by the GOS maps, is presented in Figure 3-11. Before the thermal exposure, the fibrous grains were aligned along the rolling direction, which significantly strengthened the alloys (Figure 3-10a–d). Deformed grains were predominant in the alloys, accounting for 95% of alloy E and 97% of alloy G (Figure 3-11) with the presence of few substructured grains.

After the thermal exposure at 310 ºC for 1000 h, the percentages of deformed grains in alloys E and G remained almost unchanged, 95% and 96%, respectively, relative to their structures before thermal exposure. After the thermal exposure at 350 ºC for 1000 h, the deformed grain percentage decreased to 77% in alloy E and 87% in alloy G, accompanied by increases in contents of substructured and recrystallized grains in both alloys to different extents (19% and 4% in alloy E vs 10% and 2% in alloy G, respectively), showing a slow static recovery. Under the exposure at 400 °C for 400 h, the deformed grain percentage decreased to 47% in alloy E and 72% in alloy G, but they still contained inferior fractions of recrystallized grains (5% and 3%, respectively). However, the substructured grain percentage noticeably increased to 48% in alloy E and 25% in alloy G, which shows that the static recovery of the grain structure accelerated during the thermal exposure at 400 °C. Relevant studies have shown that Al-Zr-Sc alloys did not exhibit significant recrystallization after thermal exposure at 400 °C or even after thermal exposure at 600 °C for 1 h [43, 44], which is in line with the results of this study.

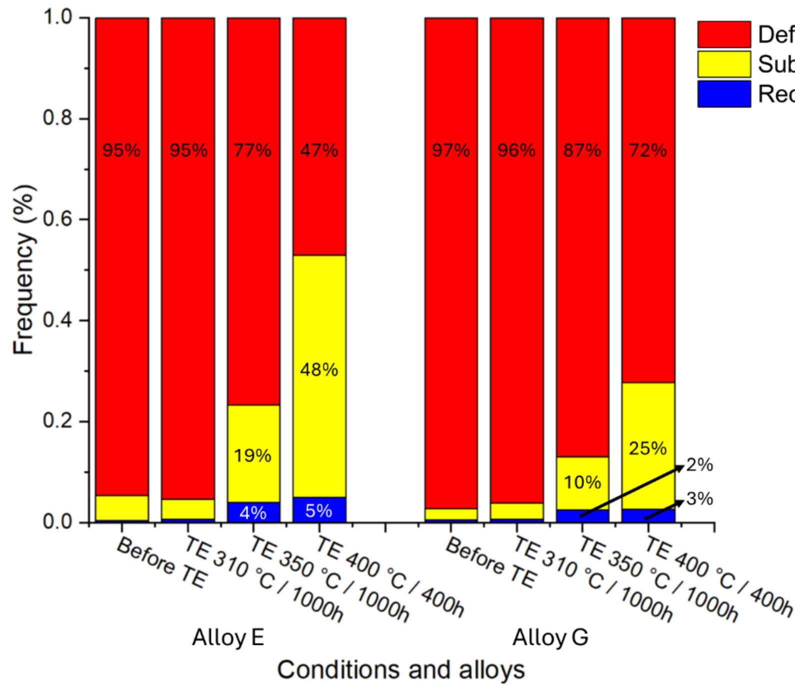

Figure 3-11 Statistical distribution of the fractions of different grain structures based on the GOS maps Figure 3-10.

Thus, all four Al-Zr-Sc conductor alloys generally exhibited excellent recrystallization resistances during thermal exposures at 310–400 ºC. However, the high-Zr-content alloys G and H exhibited higher contents of deformed grain structures after long-term thermal exposures at 350 and 400 ºC than the low-Zr-content alloys E to G, which is attributed to the higher resistances of the precipitate coarsening and thereby higher resistance to the static recovery. The low reductions in the tensile strengths of alloys G and H during thermal exposures at 350 and 400 ºC resulted from the combination of a low precipitate coarsening and slow static recovery of the grain structure.

3.5 Conclusions

Four Al-Zr-Sc conductor alloys with 0.1–0.18% Zr and 0.1–0.15% Sc were processed by the wire drawing route. Their mechanical properties, ECs, and precipitation microstructures were systematically investigated. Furthermore, the thermal stabilities of the alloy wires during long-term thermal exposures at three different temperatures were evaluated. The conclusions can be summarized as follows.

1. After cold wire drawing and annealing, the UTSs of the four Al-Zr-Sc alloy wires reached 206-214 MPa, while the ECs were 57-57.5% IACS. All four alloy wires were strengthened by a large number of $Al_3(Sc,Zr)$ nanoprecipitates, with only a minor impact on the EC. With the increase in Zr or Sc content, the UTS only slightly increased, which shows the weaker dependence on the Zr and Sc levels.

2. All four alloys exhibited excellent thermal stabilities during thermal exposure at 310 °C for up to 1000 h without remarkable reductions in mechanical properties and changes in deformed grain structure.

3. All four alloys still exhibited excellent thermal stabilities after thermal exposure at 350 °C for 200 h, where the reductions in UTS were controlled within 5%. With the prolonged exposure, the thermal stabilities of the wires deteriorated with increased reductions in UTS. During the thermal exposure at 400 °C, the alloy wires became unstable, and the reductions in UTS rapidly increased with the exposure time, accompanied by precipitate coarsening and accelerated static recovery of the grain structure.

4. The Al-0.18Zr-0.1Sc and Al-0.18Zr-0.15Sc alloys with high Zr contents exhibited better thermal stabilities after the long-term thermal exposures at 350 and 400 °C than their Al-

0.1Zr-0.1Sc and Al-0.13Zr-0.1Sc alloy counterparts, with smaller reductions in UTSs, lower precipitate coarsening, and higher resistances to static recovery.

References

[1] Andrae AS, Edler T. On global electricity usage of communication technology: trends to 2030. Challenges 2015; 6(1):117-157.

[2] Biyik S, Aydin M. Investigation of the effect of different current loads on the arc-erosion performance of electrical contacts. Acta Physica Polonica A 2016; 129(4):656-660.

[3] Biyik S, Arslan F, Aydin M. Arc-erosion behavior of boric oxide-reinforced silver-based electrical contact materials produced by mechanical alloying. Journal of Electronic Materials 2015; 44:457-466.

[4] Biyik S. Effect of Y2O3 addition and milling time on the synthesis of nanocrystalline Ag–ZnO composite powder via mechanical alloying. Journal of Radiation Research and Applied Sciences 2024; 17(2):100867.

[5] Mao Q, Zhang Y, Guo Y, Zhao Y. Enhanced electrical conductivity and mechanical properties in thermally stable fine-grained copper wire. Communications Materials 2021; 2(1):46.

[6] Algendy AY, Liu K, Rometsch P, Parson N, Chen XG. Evolution of discontinuous/continuous Al3(Sc,Zr) precipitation in Al-Mg-Mn 5083 alloy during thermomechanical process and its impact on tensile properties. Materials Characterization 2022; 192.

[7] Shao Q, Elgallad EM, Maltais A, Chen XG. Development of thermal-resistant Al–Zr based conductor alloys via microalloying with Sc and manipulating thermomechanical processing. Journal of Materials Research and Technology 2023; 25:7528-7545.

[8] Matthews S. Thermal stability of solid solution strengthened high performance alloys. Superalloys: Metallurgy and manufacture 1976:215-226.

[9] Polmear I, Pons G, Barbaux Y, Octor H, Sanchez C, Morton A et al. After concorde: evaluation of creep resistant Al–Cu–Mg–Ag alloys. Materials science and technology 1999; 15(8):861-868.

[10] Tanaka T, Kamitakahara Y. Highly heat-resistant aluminum alloy “KS2000”. KOBELCO Technol. Rev 2017; 35:28-33.

[11] Rakhmonov J, Liu K, Pan L, Breton F, Chen X-G. Enhanced mechanical properties of high-temperature-resistant Al–Cu cast alloy by microalloying with Mg. Journal of Alloys and Compounds 2020; 827:154305.

[12] Shurkin P, Letyagin N, Yakushkova A, Samoshina M, Ozherelkov DY, Akopyan T. Remarkable thermal stability of the Al-Ca-Ni-Mn alloy manufactured by laser-powder bed fusion. Materials Letters 2021; 285:129074.

[13] Pozdniakov AV, Barkov RY. Microstructure and mechanical properties of novel Al-Y-Sc alloys with high thermal stability and electrical conductivity. Journal of Materials Science & Technology 2020; 36:1-6.

[14] Su X, Lei Y, Chen Y, Qu H, Qi Z, Zheng G et al. Precipitating thermally reinforcement phase in aluminum alloys for enhanced strength at 400° C. Journal of Materials Science & Technology 2024; 172:71-82.

[15] Han Y, Shao D, Chen B, Peng Z, Zhu Z, Zhang Q et al. Effect of Mg/Si ratio on the microstructure and hardness–conductivity relationship of ultrafine-grained Al–Mg–Si alloys. Journal of Materials Science 2017; 52(8):4445-4459.

[16] Khelfa T, Lachhab R, Azzeddine H, Li F, Muñoz-Bolaños J, Cabrera-Marrero J et al. Thermal Stability of an Al-Mg-Si alloy after Equal Channel Angular Pressing. 2020.

[17] Yuan W, Liang Z. Effect of Zr addition on properties of Al–Mg–Si aluminum alloy used for all aluminum alloy conductor. Materials & Design 2011; 32(8-9):4195-4200.

[18] Zhang J-Y, Gao Y-H, Yang C, Zhang P, Kuang J, Liu G et al. Microalloying Al alloys with Sc: a review. Rare Metals 2020; 39:636-650.

[19] Hu K, Zou C, Wang H, Wei Z. Influence of Ti elements on the evolution of microstructure, mechanical properties and thermal stability of Al-Cu alloy. Journal of Alloys and Compounds 2023; 952:169860.

[20] Lv H, Peng P, Feng T, Gao H, Wang Y, Wang J. Phase transformation and thermal stability of the laser powder bed fused high-strength and heat-resistant Al–Ce–Mg alloy. Journal of Materials Research and Technology 2024; 28:4577-4584.

[21] Mohammadi A, Enikeev NA, Murashkin MY, Arita M, Edalati K. Developing age-hardenable Al-Zr alloy by ultra-severe plastic deformation: Significance of supersaturation, segregation and precipitation on hardening and electrical conductivity. Acta Materialia 2021; 203:116503.

[22] Çadırlı E, Tecer H, Şahin M, Yılmaz E, Kırındı T, Gündüz M. Effect of heat treatments on the microhardness and tensile strength of Al–0.25 wt.% Zr alloy. Journal of Alloys and Compounds 2015; 632:229-237.

[23] Belov N, Alabin A, Prokhorov AY. The influence that a zirconium additive has on the strength and electrical resistance of cold-rolled aluminum sheets. Russian Journal of Non-Ferrous Metals 2009; 50(4):357-362.

[24] Knipling KE, Karnesky RA, Lee CP, Dunand DC, Seidman DN. Precipitation evolution in Al–0.1 Sc, Al–0.1 Zr and Al–0.1 Sc–0.1 Zr (at.%) alloys during isochronal aging. Acta Materialia 2010; 58(15):5184-5195.

[25] Vo N, Dunand D, Seidman D. Improving aging and creep resistance in a dilute Al–Sc alloy by microalloying with Si, Zr and Er. Acta Materialia 2014; 63:73-85.

[26] Chao R-z, Guan X-h, Guan R-g, Di T, Chao L, Xiang W et al. Effect of Zr and Sc on mechanical properties and electrical conductivities of Al wires. Transactions of Nonferrous Metals Society of China 2014; 24(10):3164-3169.

[27] Guan R, Shen Y, Zhao Z, Wang X. A high-strength, ductile Al-0.35Sc-0.2Zr alloy with good electrical conductivity strengthened by coherent nanosized-precipitates. Journal of Materials Science & Technology 2017; 33(3):215-223.

[28] Zhang C, Jiang Y, Cao F, Hu T, Wang Y, Yin D. Formation of coherent, core-shelled nano-particles in dilute Al-Sc-Zr alloys from the first-principles. Journal of Materials Science & Technology 2019; 35(5):930-938.

[29] Shao Q, Elgallad E, Maltais A, Chen XG. Developing Al-Zr-Sc Alloys as High-Temperature-Resistant Conductors for Electric Overhead Line Applications. Light Metals 20232023, pp. 1266-1272.

[30] Wu S, Xue H, Yang C, Cheng P, Zhang P, Kuang J et al. Effect of Si addition on the precipitation and mechanical/electrical properties of dilute Al–Zr-Sc alloys. Materials Science and Engineering: A 2021; 812:141150.

[31] De Luca A, Dunand DC, Seidman DN. Scandium-Enriched Nanoprecipitates in Aluminum Providing Enhanced Coarsening and Creep Resistance. Light Metals 20182018, pp. 1589-1594.

[32] Fuller C, Seidman D. Temporal evolution of the nanostructure of Al(Sc,Zr) alloys: Part II-coarsening of Al(ScZr) precipitates. Acta Materialia 2005; 53(20):5415-5428.

[33] Lin JD, Seidman DN, Dunand DC. Improving coarsening resistance of dilute Al-Sc-Zr-Si alloys with Sr or Zn additions. Materials Science and Engineering: A 2019; 754:447-456.

[34] Thermal-resistant aluminium alloy wire for overhead line conductor. International Standard IEC 62004 2007.

[35] Li Liu J-TJ, Bo Zhang, Wen-Zhu Shao, Liang Zhen. Enhancement of strength and electrical conductivity for a dilute Al-Sc-Zr alloy via heat treatments and cold drawing. J. Mater. Sci. Technol. 2019; 35(6):962-971.

[36] Qian F, Jin S, Sha G, Li Y. Enhanced dispersoid precipitation and dispersion strengthening in an Al alloy by microalloying with Cd. Acta Materialia 2018; 157:114-125.

[37] Kelly P, Jostsons A, Blake R, Napier J. The determination of foil thickness by scanning transmission electron microscopy. Physica status solidi (a) 1975; 31(2):771-780.

[38] Dai K, Ye J, Wang Z, Gao M, Chen J, Guan R. Effects of Sc and Zr addition on the solidification and mechanical properties of Al–Fe alloys. Journal of Materials Research and Technology 2022; 18:112-121.

[39] Dumbre J, Kairy SK, Anber E, Langan T, Taheri ML, Dorin T et al. Understanding the formation of (Al, Si) 3Sc and V-phase (AlSc2Si2) in Al-Si-Sc alloys via ex situ heat treatments and in situ transmission electron microscopy studies. Journal of Alloys and Compounds 2021; 861:158511.

[40] Deschamps A, Lae L, Guyot P. In situ small-angle scattering study of the precipitation kinetics in an Al–Zr–Sc alloy. Acta Materialia 2007; 55(8):2775-2783.

[41] Ning Z, Guo S, Zhang M, Cao F, Jia Y, Sun J. Characterization of the secondary phases in spray formed Al-Zn-Mg-Cu-Sc-Zr alloy during hot compression. Journal of Materials Research 2016; 31:2465-2472.

[42] Sun F, Nash GL, Li Q, Liu E, He C, Shi C et al. Effect of Sc and Zr additions on microstructures and corrosion behavior of Al-Cu-Mg-Sc-Zr alloys. Journal of materials science & technology 2017; 33(9):1015-1022.

[43] Forbord B, Hallem H, Ryum N, Marthinsen K. Precipitation and recrystallisation in Al–Mn–Zr with and without Sc. Materials Science and Engineering: A 2004; 387:936-939.

[44] Hallem H, Rittel W, Forbord B, Marthinsen K, Recrystallisation resistance of extruded and cold rolled aluminium alloys with additions of Hf, Sc and Zr, Materials science forum, Trans Tech Publ, 2006, pp. 525-530.

Chapter 4

Enhancing strength and electrical conductivity in Al-Zr-Sc conductor alloys through Sn and Sr microalloying and two-step aging treatment

(This article is under internal review)

Abstract

Trace additions of Sn (0.05 and 0.15 wt.%) and Sr (0.006 and 0.013 wt%) combined with a novel two-step aging treatment were introduced into Al–Zr–Sc conductor alloys to investigate their effects on microstructure and mechanical properties. The additions of Sn or Sr, together with two-step aging, significantly improved the mechanical strength and electrical conductivity (EC) of the alloys. In the Sn15 alloy, two-step aging enhanced microhardness, ultimate tensile strength, and EC to 78.3 HV, 216 MPa, and 58.3% IACS, respectively, compared with 74.2 HV, 206 MPa, and 57.5% IACS after conventional one-step aging. Similarly, the Sr13 alloy exhibited improved properties, with 83.2 HV, 227 MPa, and 58.0% IACS after two-step aging, versus 78.3 HV, 215 MPa, and 57.5% IACS with one-step aging. These improvements—5.5 HV, 10 MPa, and 0.8% IACS for the Sn15 alloy; 5.2 HV, 12 MPa, and 0.7% IACS for the Sr13 alloy—are primarily attributed to the precipitation of a larger number of fine $Al_3(Sc,Zr)$ strengthening precipitates. Early-stage $Al_3(Sc,Zr)$ precipitation was observed in the Sn15 alloy after the first-step aging at 300 °C for 4 h. In the Sr-containing alloys, enhanced strengthening was also associated with increased dislocation resistance in the presence of stacking faults. The trace addition of Sn or Sr

combined with two-step aging offers a cost-effective strategy for developing the next generation of thermally stable, high-performance conductor alloys.

Keywords: Al-Zr-Sc alloys, mechanical properties, electrical conductivity, Sn addition, Sr microalloying.

4.1 Introduction

The global push toward decarbonization and the electrification of transportation and infrastructure has placed increasing demands on the efficiency and performance of overhead transmission lines [1, 2]. Therefore, developing lightweight, high-strength, and thermally stable aluminum conductor alloys has become a critical area of materials research. Conventional aluminum alloys used in conductors—commonly Al–Mg–Si 6xxx series—offer a balance of conductivity, formability, and moderate strength [3]. However, their thermal stability and mechanical performance at elevated service temperatures remain limited, posing challenges for long-term reliability in harsh operating environments [4]. The residual strength of Al–Mg–Si alloys after thermal exposure is significantly influenced by both temperature and duration, primarily due to the thermal behavior of strengthening precipitates such as β″ and β′ phases [5]. At elevated temperatures, these precipitates tend to coarsen or dissolve, reducing mechanical strength. For instance, exposure to 230 °C for 3 h can reduce the residual strength to approximately 74.6% of its original value [4]. The inherent limitations of Al–Mg–Si conductor alloys, particularly their susceptibility to thermal degradation, significantly constrain their applicability in high-temperature environments. Consequently, advanced aluminum-based conductors that exhibit enhanced mechanical strength and thermal stability are necessary to meet the demands of modern electrical and structural applications. Al–Zr–Sc alloys have emerged as promising candidates for high-performance conductors owing to their exceptional thermal stability, electrical conductivity, and mechanical properties [6-10]. These attributes are primarily attributed to forming coherent, nanoscale $L1_2$–$Al_3(Sc,Zr)$ precipitates [11]. The combination of Sc and Zr in Al–Zr–Sc alloys significantly enhances the thermal stability of these precipitates by forming a core–shell structure, in which the Sc-rich core is surrounded by a Zr-rich shell [12]. This configuration effectively impedes grain boundary movement and dislocation motion, maintaining strength and resisting recrystallization during prolonged exposure to elevated temperatures [13]. An Al–0.35Sc–0.2Zr alloy reportedly achieved a strength of 210 MPa and an electrical conductivity of 60.2% IACS, with minimal strength loss after exposure to 230–400 °C [14]. Our recent studies have also demonstrated that microalloying Sc (0.07–0.15 wt%) in Al–(0.10–0.18)Zr alloys promoted the precipitation of a large number of $Al_3(Sc,Zr)$ nanoparticles, which remained stable and resisted coarsening at temperatures up to 400 °C, thereby providing outstanding thermal resistance and making Al–Zr–Sc alloys suitable for applications requiring high thermal resistance [15].

Incorporating trace amounts of tin (Sn) and strontium (Sr) into aluminum alloys has significantly enhanced their mechanical properties and precipitation behavior. In Al–Cu–Mn alloys, a 0.1 wt.% addition of Sn increased the peak hardness by approximately 43% compared to Sn-free counterparts [16]. This improvement is attributed to Sn's role in refining the precipitation structure and stabilizing strengthening phases such as θ″ and θ′, leading to a finer and more uniform distribution of precipitates [17]. Similarly, in Al–Mg–Si alloys, Sn additions have been found to suppress natural aging and promote artificial aging by enhancing the nucleation and growth of β″ precipitates, increasing yield and tensile strengths [18]. Regarding Sr, its addition to Al–Mg alloys has been demonstrated to improve mechanical properties through multiple mechanisms [19]. Adding Sr contributed to grain refinement [20], solid solution strengthening, and increased dislocation density, which enhanced mechanical properties [19]. Sr also influenced the precipitation behavior in Al-Si alloys by modifying the morphology of eutectic Si, improving ductility and strength [21]. In EN AC 46000 alloy, adding ~276 ppm of Sr increased the ultimate tensile strength from 300 MPa to 350 MPa and improved elongation from 3% to 6% [22]. Sr also enhances Sc diffusivity by strongly binding with Al vacancies, accelerating $Al_3(Sc,Zr)$ nucleation and increasing hardness [10]. Adding a small amount of Sr to the Al–Si–Cu alloy enhanced the strength, primarily due to the formation of numerous interacting stacking faults that impeded dislocation motion [23]. These findings highlight the Sr addition in various Al alloys to enhance mechanical performance through microstructural refinement and optimizing precipitation behavior, suggesting potential applications in Al–Zr–Sc alloy systems.

Previous studies have demonstrated that two-step aging treatments can significantly enhance precipitation behavior in Al–Zr–Sc alloys. For instance, Zhao et al. [24] reported that a novel two-stage heat treatment involving medium-temperature aging improved the microstructure and mechanical properties of Al–Mg–Sc–Zr alloys by promoting the formation of fine $Al_3(Sc,Zr)$ nanoprecipitates. Similarly, a two-step aging process was applied to optimize the nucleation and growth of $Al_3(Sc,Zr)$ precipitates, showing that sequential aging at lower and higher temperatures can significantly enhance precipitate uniformity and mechanical strength in Al-Zr-Sc alloys [11]. Research by Zhang et al. indicated that two-step homogenization treatments effectively influenced the precipitation behavior of Al_3Zr dispersoids, improving mechanical properties in aluminum alloys [25]. Two-step aging can improve the aging response of an AlFeNi–0.2Sc–0.2Zr alloy compared with single-step methods [26]. These findings underscore the efficacy of two-step aging processes in refining precipitate structures and enhancing the performance of Al–Zr–Sc alloys.

In this study, novel two-step aging treatments were investigated to optimize the strengthening effects of trace Sn and Sr additions in Al–Zr–Sc conductor alloys. The underlying strengthening mechanisms were examined through detailed microstructural characterization. Mechanical properties were evaluated using microhardness and ultimate tensile strength (UTS) measurements, whereas electrical conductivity was assessed via the eddy current method. Transmission electron microscopy (TEM) and electron backscatter diffraction (EBSD) were used to analyze precipitate characteristics and grain structures.

4.2 Materials and methods

4.2.1 Materials preparation

Six experimental alloys were prepared, and their nominal and actual chemical compositions, as determined by optical emission spectroscopy, are listed in Table 4-1. The Zr and Sc levels were selected from our previous studies to balance electrical conductivity and mechanical properties [6, 13, 15]. All alloys were designed with a low Sc content (≤0.10 wt.%) to reduce material costs. To investigate the effect of Sn additions, two alloys, designated Sn5 and Sn15, containing 0.05 and 0.15 wt.% Sn, respectively, were compared with the Sn-free base alloy (Sn0). Similarly, to study the influence of Sr, two alloys, Sr6 and Sr13, with 0.006 and 0.013 wt.% Sr, respectively, were compared with the Sr-free base alloy

(Sr0). The alloys were produced by melting commercially pure aluminum (99.85% purity) together with Al–2 wt.% Sc, Al–15 wt.% Zr, Al–25 wt.% Fe, Al–50 wt.% Si, and Al–10 wt.% Sr master alloys, as well as Sn powder. Melting was conducted in a SiC crucible using an electrical resistance furnace at 750 °C, with a holding time of 3 h to ensure chemical homogeneity. The molten alloys were stirred and poured into a Y-shaped permanent steel mold preheated to 400 °C, yielding rectangular ingots with dimensions of 30 mm × 40 mm × 80 mm.

Table 4-1 Nominal and actual chemical compositions of the alloys (wt.%).

Alloy	Nominal composition	Actual chemical composition						
		Si	Fe	Zr	Sc	Sn	Sr	Al
Sn0	Al-0.1Zr-0.09Sc	0.26	0.32	0.10	0.09	0	--	Bal.
Sn5	Al-0.1Zr-0.09Sc-0.05Sn	0.26	0.29	0.10	0.07	0.05	--	Bal.
Sn15	Al-0.1Zr-0.09Sc-0.15Sn	0.28	0.31	0.10	0.10	0.15	--	Bal.
Sr0	Al-0.17Zr-0.07Sc	0.26	0.27	0.18	0.05	--	0	Bal.
Sr6	Al-0.17Zr-0.07Sc-0.006Sr	0.25	0.29	0.17	0.07	--	0.006	Bal.
Sr13	Al-0.17Zr-0.07Sc-0.012Sr	0.25	0.29	0.17	0.07	--	0.013	Bal.

4.2.2 Thermomechanical processing

The thermomechanical processing of the experimental alloys began with the casting of rectangular ingots, followed by hot rolling, heat treatments, cold wire drawing, and annealing, as illustrated in Figure 4-1. Hot rolling was performed on 26.5 mm-thick rectangular ingots using a laboratory-scale rolling mill. The ingots were rolled at 550 °C through multiple passes to produce plates with a thickness of 8 mm, corresponding to a total thickness reduction of 70%. The rolled plates were subsequently cut and machined into square bars with cross-sectional dimensions of 6.7 mm × 6.7 mm, which were then used for subsequent heat treatments and cold wire drawing.

After hot rolling, a solution heat treatment (SHT) was applied at 600 °C for 8 h to promote the formation of a supersaturated solid solution in all rolled plates. A two-step aging process was investigated and compared with the traditional one-step aging process to examine the effect of aging treatments. The one-step aging was conducted at 350 °C for up to 96 h to promote the precipitation of nanoscale $Al_3(Sc,Zr)$ particles (Figure 4-1b), whereas the two-step aging consisted of a first step at 300 °C for up to 24 h, followed by a second step at 350 °C for up to 96 h (Figure 4-1c). In Al–Zr–Sc alloys, clustering of Sn atoms has been observed at the cores of $Al_3(Sc,Zr)$ precipitates after aging at 300 °C for 24 h [27]. Furthermore, prior studies have shown that Sr significantly reduces the stacking fault energy in aluminum and improves ultimate tensile strength by enhancing the interaction between dislocations and stacking faults after aging at 300 °C for 4 h [10, 23, 28]. Two-step aging parameters were separately optimized for Sn- and Sr-containing alloys based on microhardness and electrical conductivity evolution.

Cold wire drawing was subsequently performed using a laboratory-scale wire drawing mill. The 6.7 mm square bars were drawn to wires with a final diameter of 4.3 mm through multiple passes, achieving an overall area reduction of approximately 68%. After cold wire drawing, an annealing treatment at 350 °C for 5 h was applied to all alloys to relieve internal stresses induced by cold deformation and to enhance electrical conductivity for conductor applications.

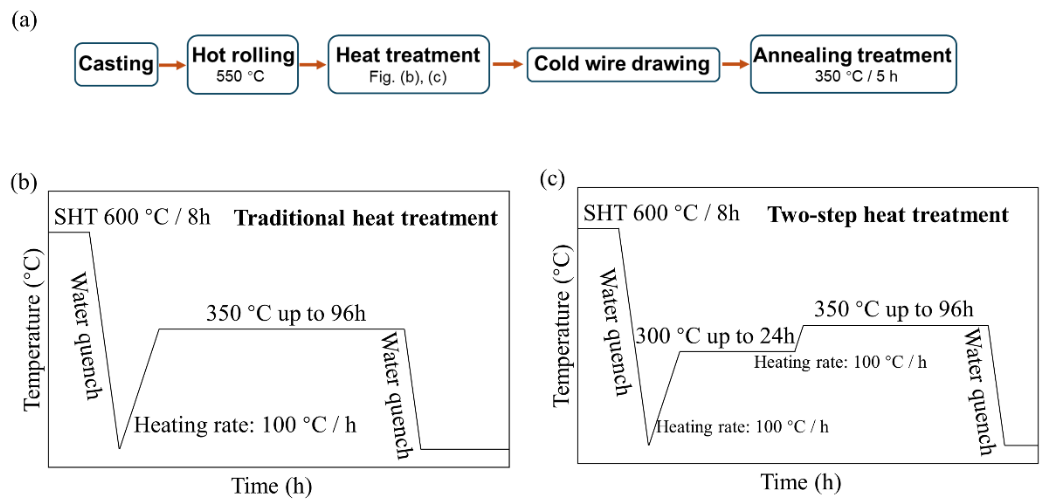

Figure 4-1 Thermomechanical processing of experimental alloys, (a) thermomechanical processing route, (b) traditional one-step aging treatment, and (c) two-step aging treatment.

4.2.3 Electrical and mechanical properties testing

Vickers microhardness measurements were performed using an NG-1000 CCD microhardness tester under a load of 25 g and a dwell time of 15 s. Electrical conductivity was evaluated using a Sigmascope SMP10 device based on the eddy current method, with results expressed as a percentage of the International Annealed Copper Standard (% IACS). For each condition, fifteen measurements were taken on well-polished cross sections of the 4.3-mm-diameter wires to ensure the statistical reliability of the microhardness and electrical conductivity data.

The ultimate tensile strength (UTS) and percentage elongation (El) were determined using an Instron 8801 servo-hydraulic testing machine at a 25 mm/min strain rate. Tensile tests were conducted on the 4.3-mm-diameter wires with an initial gauge length of 250 mm.

For each condition, three tensile specimens were tested, and the average values of UTS and El were calculated to represent the mechanical properties of the alloys.

4.2.4 Microstructure characterization

Transmission electron microscopy (TEM, JEOL JEM-2100) in dark-field mode, operated at an accelerating voltage of 200 kV, was used to observe the $Al_3(Sc,Zr)$ precipitates. TEM specimens were sliced from the cross sections of the 4.3-mm-diameter wires and subsequently thinned using a twin-jet electro-polisher. The precipitate characteristics, including number density and average diameter, were quantified from nine TEM images for each experimental condition.

Electron backscatter diffraction (EBSD) analyses were performed on the central regions of the samples, parallel to the cold wire drawing direction. EBSD maps were acquired with a step size of 1 μm and a sample tilt angle of 70°, using a Symmetry S3 CMOS detector (Oxford Instruments, UK). Grain structure features, including deformed, substructured, and recrystallized regions, were characterized using HKL Channel 5 software.

4.3 Results and discussion

4.3.1 Effect of aging treatment and Sn/Sr microalloying on the microhardness and EC

The two-step aging process (first step at 300 °C for x h followed by a second step at 350 °C for 48 h) was first investigated to optimize the first-step aging time (Figure 4-2). With increasing aging time to 4 h, the microhardness of Sn-containing alloys increased from 67.5 HV to 69.5 HV in Sn5 and to 71.2 HV in Sn 15, whereas the EC increased from 57.8% IACS to 58.1% IACS in Sn5 and from 57.6% IACS to 58.0% IACS in Sn15, respectively (Figure 4-2a). Further increasing the first-step aging time to 24 h resulted in a plateau in both microhardness and EC, indicating that the nucleation and growth of early-stage $Al_3(Sc,Zr)$ precipitates reached a maximum within 4 h. The microhardness and electrical conductivity of Sn15 after two-step aging were higher than those of Sn5, indicating that higher Sn content promotes the formation of more refined and uniformly distributed $Al_3(Sc,Zr)$ precipitates, enhancing both mechanical strength and EC. These results align with previous findings [29] that Sn microalloying accelerates the nucleation of $L1_2$ Al_3Zr precipitates at low temperature, leading to a rapid age-hardening response in Al–Zr alloys. The observed plateau suggests that Sn enhances the kinetics of precipitation during the early aging stage, making a 4 h treatment at 300 °C sufficient to achieve peak hardening.

In Sr-containing alloys, both microhardness and EC increased slowly but steadily with increasing first-step aging time (Figure 4-2b). After 24 h aging, the microhardness increased from 73.0 HV to 77.1 HV in Sr6 and to 77.8 HV in Sr13, whereas the EC increased from 57.4% IACS to 57.5% IACS in Sr6 and to 57.8% IACS in Sr13, respectively. This enhancement can be attributed to the strong binding between Sr atoms and aluminum vacancies in the solid solution, which has been reported to promote the nucleation rate of $Al_3(Sc,Zr)$ precipitates in the temperature range of 250–300 °C [10]. The microhardness and electrical conductivity of Sr13 after two-step aging were slightly higher than those of Sr6, suggesting that a higher Sr content further enhances the nucleation rate of $Al_3(Sc,Zr)$ precipitates. These results are consistent with the findings [10] that the strong interaction between Sr atoms and Al vacancies in the matrix accelerates the nucleation rate of $Al_3(Sc,Zr)$ precipitates by enhancing Sc diffusivity, as reflected by the continuous increase in hardness with prolonged aging time.

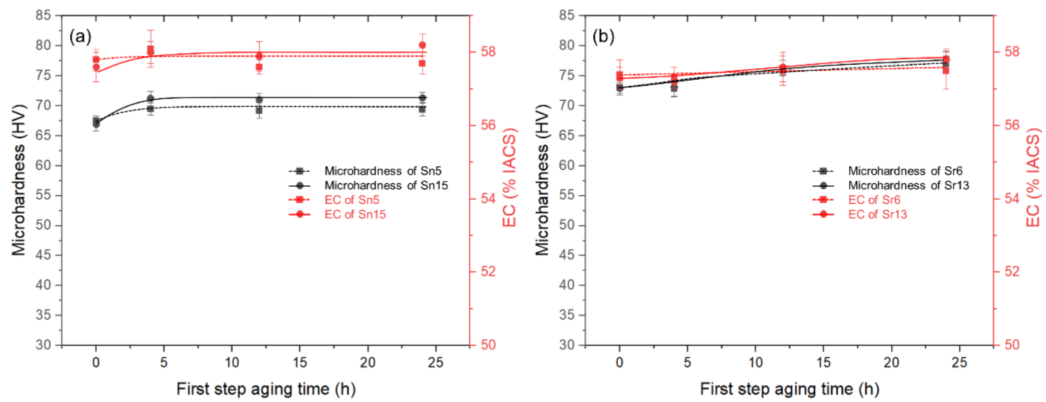

Figure 4-2 Evolution of microhardness and electrical conductivity during the first-step aging in the two-step aging process (300 °C for x h + 350 °C for 48 h): (a) Sn5 and Sn15 alloys, and (b) Sr6 and Sr13 alloys.

From the above results, the first-step aging times for the two-step aging process were fixed at 300 °C for 4 h for the Sn-containing alloys and 24 h for the Sr-containing alloys. The second-step aging treatment was then examined by tracking the evolution of microhardness and EC (Figure 4-3). In Figure 4-3a and b, the microhardness and EC curves of the Sn0 alloy after one-step and two-step aging were nearly identical, with no significant improvement from the two-step process. The peak values for Sn0 were achieved after one-step aging at 350 °C for 72 h, reaching 70.3 HV and 57.6% IACS, respectively. In comparison, the peak microhardness values of Sn5 and Sn15 alloys after one-step aging for 72 h were 67.1 HV and 67.6 HV, respectively—both lower than that of Sn0. In contrast, after two-step aging (300 °C for 4 h followed by 350 °C for 96 h), the peak microhardness of Sn5 and Sn15 increased to 71.2 HV and 73.1 HV, respectively (Figure 4-3a). These results indicate that the two-step aging treatment significantly improves the microhardness of Sn-containing alloys. The peak EC values of Sn5 and Sn15 alloys after one-step aging for 72 h were 57.2% IACS and 57.5% IACS, respectively, both lower than that of Sn0. During two-step aging, the EC of Sn5 and Sn15 increased rapidly within the first 24 h and continued to rise up to 96 h (Figure 4-3b). The peak EC values after two-step aging reached 58.1% IACS and 58.3% IACS, respectively. The microhardness and EC of Sn5 and Sn15 after two-step aging were significantly higher than their respective peak values from one-step aging and exceeded those of Sn0. These findings confirm that the two-step aging process effectively enhances the performance of Sn-containing alloys.

For the Sr series alloys (Figure 4-3c and d), a noticeable improvement in microhardness and EC was observed during the initial 24 h of one- and two-step aging. Beyond 48 h, the additional increase in these properties was marginal. During one-step aging, the peak microhardness and EC of Sr0 were obtained after 96 h, reaching 72.9 HV and 57.5% IACS, respectively. After two-step aging, the microhardness of Sr0 slightly increased to 73.7 HV. As shown in Figure 4-3c, the microhardness values of the Sr6 and Sr13 alloys after one-step aging were comparable to those of the Sn0 alloy, reaching 71.9 HV and 73.0 HV after 96 h, respectively. However, after the second step of aging for 96 h in the two-step process, the microhardness of Sr6 and Sr13 significantly increased to 76.6 HV and 78.2 HV, respectively. These results demonstrate that the two-step aging considerably enhanced the mechanical properties of the Sr-containing alloys. In Figure 4-3d, the EC of Sr0 after the second step of aging for 96 h in the two-step process reached 57.7% IACS, which was similar to that achieved through the one-step aging. For the Sr6 and Sr13 alloys, the EC values after the one-step aging for 96 h were 57.4% IACS and 57.3% IACS, respectively, both slightly lower than that of Sr0. However, the two-step aging led to further improvements in EC for the Sr-containing alloys, with Sr6 and Sr13 reaching 57.9% IACS and 58.0% IACS after 96 h in the second step of aging, respectively. Overall, the two-step aging treatment significantly improved the mechanical and electrical properties of the Sr-containing alloys.

The microhardness of Sn0 (74.2 HV) was lower than that of Sr0 (78.3 HV), whereas the EC of Sn0 (57.5% IACS) exceeded that of Sr0 (57.3% IACS). This difference is primarily attributed to the variation in Zr content between the base alloys, with Sr0 containing higher Zr despite its lower Sc content. These results are consistent with previous research, which shows that increasing Zr content generally enhances strength by promoting the formation of more $Al_3(Sc,Zr)$ precipitates, thereby improving mechanical properties [15].

The overall results in Figure 4-3 show that, for both Sn and Sr series alloys, microhardness and EC increased significantly during the first 24 h of the second-step aging and then generally reached peak values after 48 h in most cases. However, for some alloys, EC continued to rise gradually with prolonged aging up to 96 h (Figure 4-3b). To ensure that the maximum EC was achieved in all Al-Zr-Sc conductor alloys, the second-step aging time in the two-step process was set to 96 h for subsequent mechanical, EC, and microstructural examinations of the drawn wires.

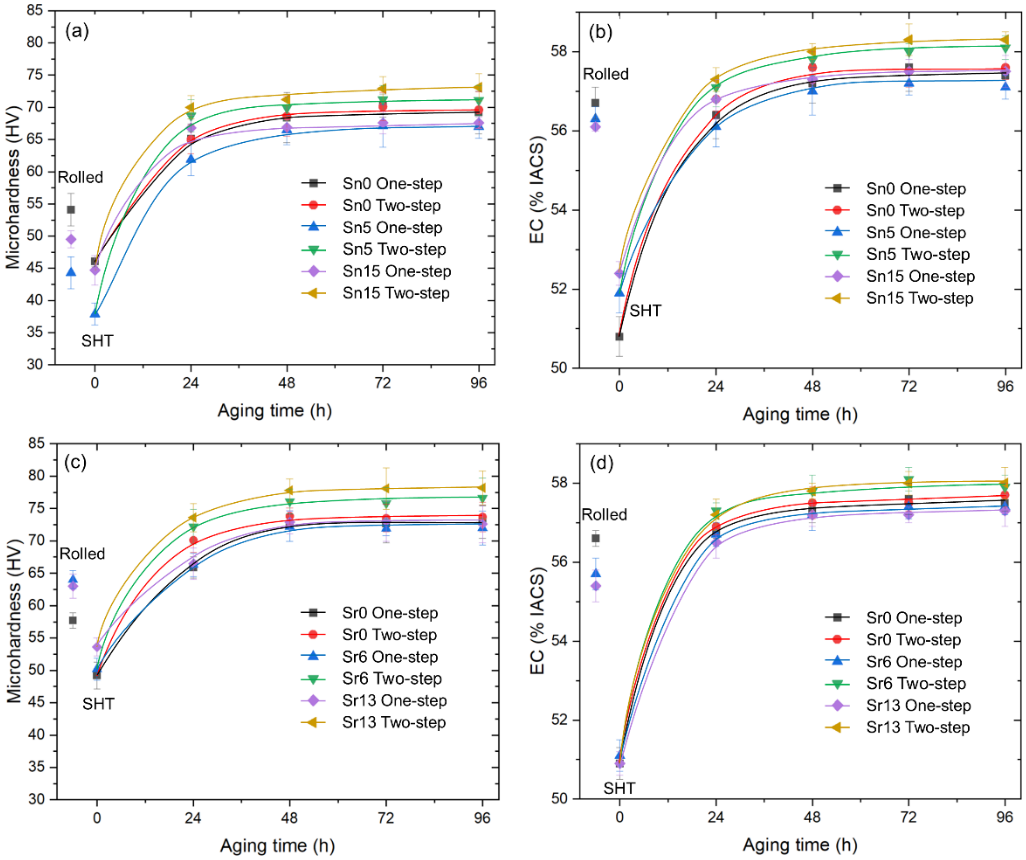

Figure 4-3 Effect of aging time in the one-step process and in the second step of the two-step aging treatment on microhardness and EC: (a, b) Sn-series alloys and (c, d) Sr-series alloys.

4.3.2 Mechanical properties and EC of wires

The two-step aging parameters were optimized in the previous section based on the evolution of microhardness and EC. For Sn-containing alloys, the two-step aging consisted of 300 °C for 4 h followed by 350 °C for 96 h, whereas for Sr-containing alloys, it involved 300 °C for 24 h followed by 350 °C for 96 h. For comparison, the one-step aging treatment was also performed for 96 h at 350 °C. After the one-step and two-step aging treatments, 4.3 mm-diameter wires were produced by cold wire drawing with an area reduction of approximately 68%, followed by annealing at 350 °C for 5 h. The microhardness and EC of the drawn wires for both alloy series are shown in Figure 4-4.

In the Sn series alloys (Figure 4-4a), the Sn0 base alloy exhibited a microhardness of 74.2 HV and an EC of 57.5% IACS after the one-step aging. Sn5 showed a microhardness of 73.3 HV and a conductivity of 57.2% IACS, whereas Sn15 recorded 72.8 HV and 57.5% IACS. The mechanical and electrical properties of both Sn-containing alloys were slightly lower than those of Sn0. After the two-step aging, Sn0 reached a microhardness of 74.3 HV and maintained an EC of 57.5% IACS, indicating negligible change compared with the one-step aging. In contrast, Sn5 and Sn15 demonstrated marked improvements after the two-step aging: Sn5 increased to 77.4 HV and 58.1% IACS, and Sn15 reached 78.3 HV and 58.3% IACS. These results indicate that the two-step aging significantly enhanced microhardness and EC in Sn-containing alloys. The negligible change in Sn0 confirms that the two-step aging provided no additional benefit in the absence of Sn. The improvements in Sn5 and Sn15 appeared only after applying the two-step aging, suggesting that Sn plays a critical role during the first step of aging by promoting the nucleation of $Al_3(Sc,Zr)$ precipitates. This leads to a more uniform and denser precipitate distribution, contributing to improved mechanical properties and reduced electron scattering, as discussed in Section 4.3.3.

In the Sr series alloys (Figure 4-4b), the Sr0 alloy exhibited a microhardness of 78.3 HV and an EC of 57.3% IACS after the one-step aging. Sr6 showed values of 78.5 HV and 57.2% IACS, whereas Sr13 recorded 78.0 HV and 57.3% IACS, indicating no evident benefit from Sr additions under the one-step aging condition. After the two-step aging, the microhardness and EC of Sr0 remained nearly unchanged. In contrast, Sr6 increased to 82.9 HV and 57.9% IACS, and Sr13 reached 83.2 HV and 58.0% IACS, confirming the strengthening and conductivity benefits of the optimized two-step aging treatment. The effect of Sr microalloying became apparent only under the two-step aging, likely because it promoted the nucleation of $Al_3(Sc,Zr)$ precipitates during the first step of aging. These improvements in microhardness and EC are consistent with literature findings that Sr accelerates the nucleation of $Al_3(Sc,Zr)$ precipitates by enhancing Sc diffusivity through strong Sr–vacancy binding [10].

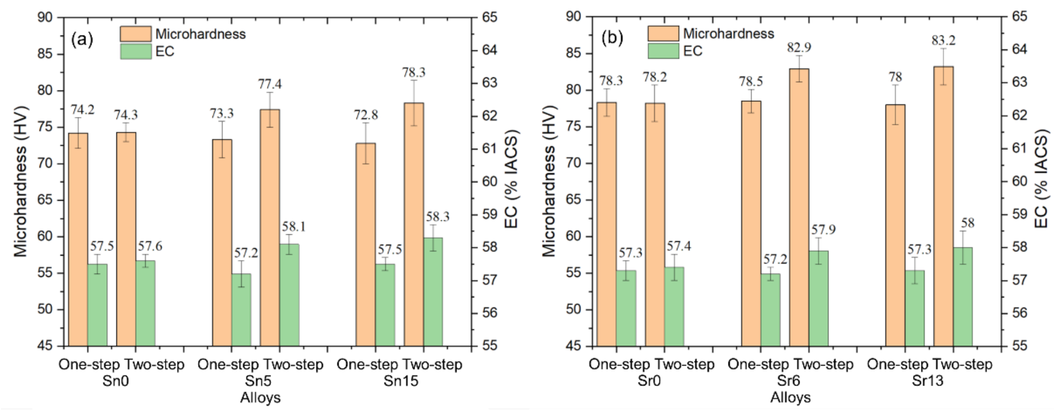

Figure 4-4 Microhardness and electrical conductivity of (a) Sn series alloys and (b) Sr series alloys after one-step and two-step aging treatments.

The tensile properties of both series alloys were evaluated through UTS and El measurements on the drawn wires, as shown in Figure 4-5. Under the one-step aging condition, the Sn0, Sn5, and Sn15 alloys exhibited UTS values of 205.6, 205.8, and 205.2 MPa, respectively, with elongation ranging from 5.5% to 6.0%. After the two-step aging, Sn0 showed almost no change in UTS or El. In contrast, the Sn-containing alloys demonstrated notable increases in strength, with UTS values reaching 212.3 MPa in Sn5 and 215.9 MPa in Sn15, whereas their elongation slightly decreased to 4.8% and 4.4%, respectively. These results confirm that Sn5 and Sn15 benefited from the two-step aging process, reinforcing that Sn plays a critical role in activating precipitation strengthening during the first step of aging. Overall, the two-step aging effectively enhanced mechanical strength without severely compromising ductility.

For the Sr series alloys (Figure 4-5b), Sr0, Sr6, and Sr13 after the one-step aging exhibited UTS values of 214.9, 215.3, and 215.4 MPa, respectively, with elongation ranging from 5.1% to 5.8%. After the two-step aging, Sr0 achieved a slightly higher UTS of 217 MPa. In contrast, Sr6 and Sr13 showed substantial increases in strength, reaching 225.7 MPa and 226.5 MPa, respectively. Notably, the UTS and EC values of both Sr6 and Sr13 met the AT2 grade requirements specified in the international standard IEC 62004 for thermal-resistant aluminum alloy wire used in overhead line conductors (225 MPa and 55% IACS) [30]. Elongation values for all alloys remained between 4.2% and 6.0%, exceeding the minimum requirements for thermal-resistant aluminum alloy conductors. The consistent elongation above 4% for both Sr-containing alloys after the two-step aging indicates that the strength gains were achieved without sacrificing ductility [30]. These results underscore the beneficial role of Sr in enhancing precipitation kinetics and promoting a more optimal microstructure during the two-step aging.

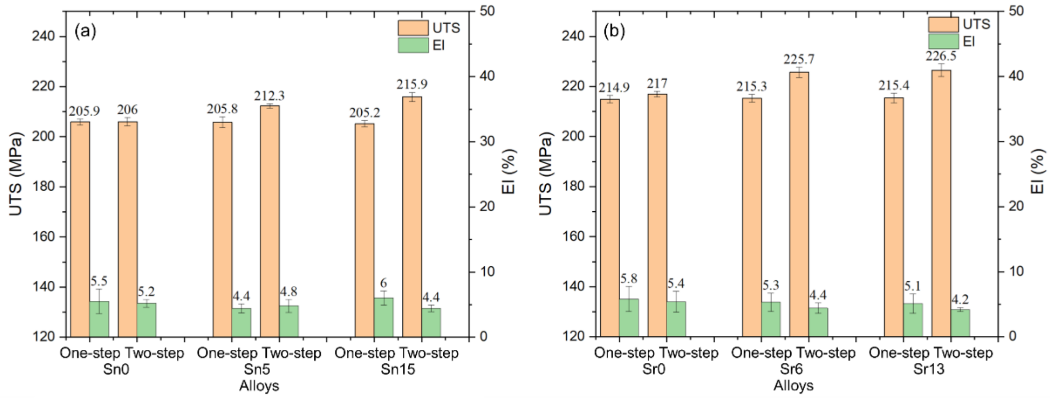

Figure 4-5 Ultimate tensile strength (UTS) and elongation (El) comparison after the one-step and two-step aging treatments: (a) Sn series alloys and (b) Sr series alloys.

The enhancements in EC, microhardness, and UTS of Sn- and Sr-containing alloys after the two-step aging are summarized in Figure 4-6. Notably, the increases in EC for alloys Sn5, Sn15, Sr6, and Sr13 were 0.9, 0.8, 0.7, and 0.7% IACS, respectively. The corresponding improvements in microhardness were 4.1, 5.5, 4.4, and 5.2 HV, whereas the UTS gains were 6.5, 10.7, 10.4, and 10.9 MPa, respectively. These UTS improvements show a strong correlation with the increases in microhardness. In both Sn- and Sr-containing alloys, higher alloying levels led to incremental gains in EC, microhardness, and UTS, confirming a composition-dependent enhancement in performance under the two-step aging condition.

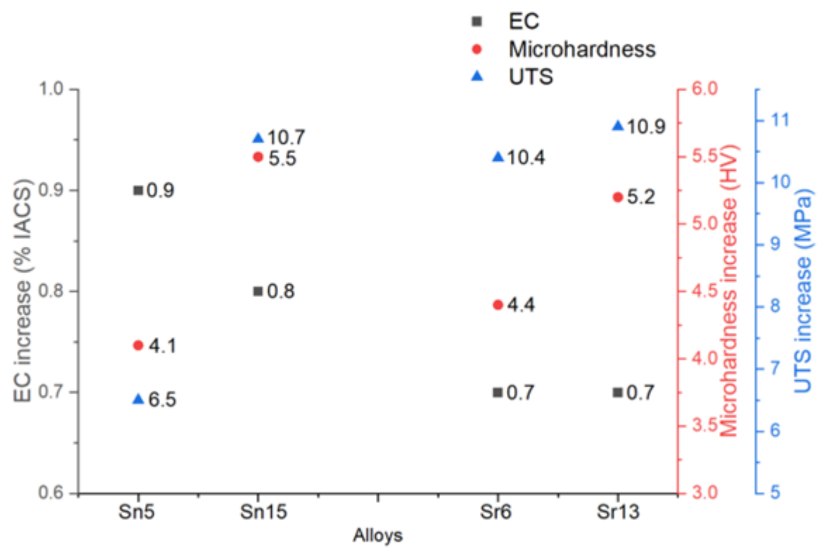

Figure 4-6 Electrical conductivity, microhardness, and UTS increase after two-step aging.

These results demonstrate the effectiveness of two-step aging in enhancing the overall performance of Sn- and Sr-containing aluminum alloys. The observed improvements are primarily attributed to the promoted nucleation of $Al_3(Sc,Zr)$ precipitates during the first step of aging, where the presence of Sn and Sr appears to increase the availability and mobility of vacancies, thereby facilitating early-stage precipitation. The greater enhancements in mechanical strength and microhardness at higher Sn and Sr levels suggest that these trace elements play a synergistic role in modifying vacancy behavior and accelerating precipitate formation [10]. Furthermore, the simultaneous increase in EC indicates that the precipitation evolution does not significantly hinder electron mobility, which is critical for conductive applications. Overall, the two-step aging strategy achieves a balanced improvement in mechanical and electrical properties, making it a promising approach for developing high-performance thermal-resistant aluminum conductors.

4.3.3 Precipitate microstructure

Figure 4-7 displays dark-field TEM images and corresponding selected area electron diffraction patterns (SAEDPs) for the Sn series alloys after traditional one- and two-step aging treatments. In all alloys, regardless of the aging method, fine $Al_3(Sc,Zr)$ nanoprecipitates were uniformly distributed in the Al matrix. Quantitative analyses of these precipitates are summarized in Table 4-2. For the Sn0 alloy, the number density and diameter of the precipitates remained nearly unchanged between the one-step and two-step aging conditions, with values of approximately 5.3 nm and 1.18×10^{22} m^{-3}, respectively. In contrast, the Sn5 and Sn15 alloys exhibited a higher number of finer precipitates after the two-step aging. Specifically, the number density increased from 1.16×10^{22} m^{-3} and 1.15×10^{22} m^{-3} after the one-step aging to 1.32×10^{22} m^{-3} and 1.39×10^{22} m^{-3}, respectively, after the two-step aging. The precipitate diameters of $Al_3(Sc,Zr)$ remained similar for all alloys under both aging conditions, at approximately 5.3 nm.

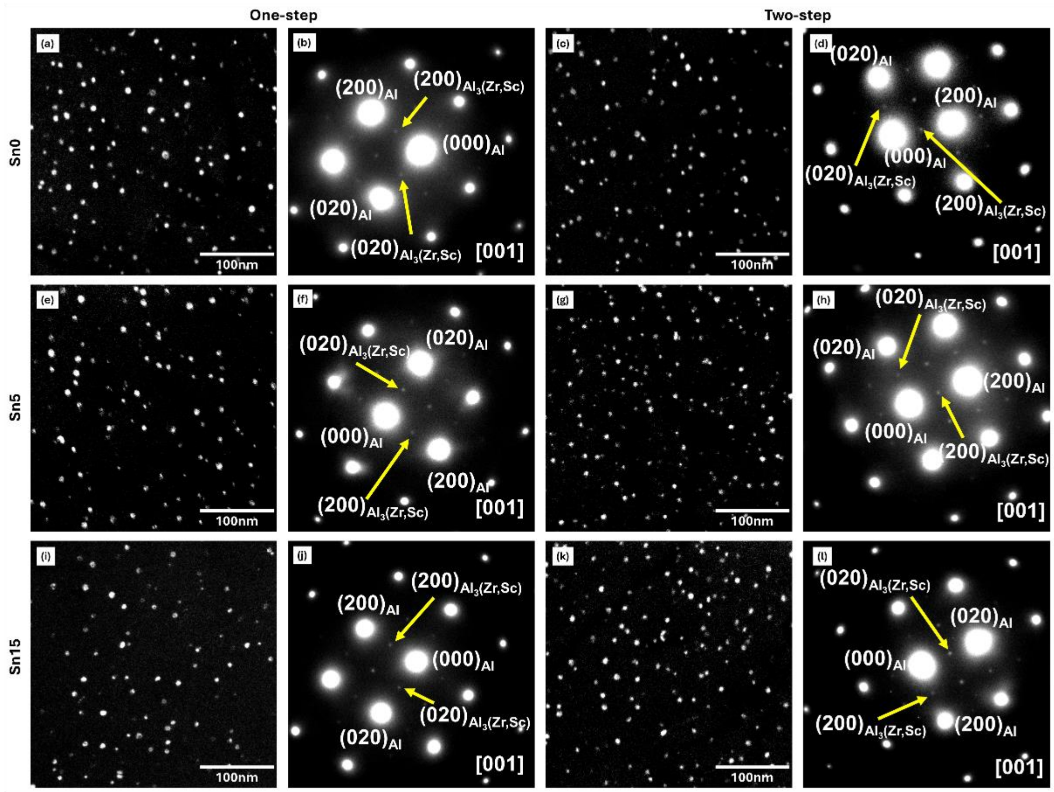

Figure 4-7 Dark-field TEM images and corresponding SAEDPs of the Sn series alloys after the one-step and two-step aging treatments, showing $Al_3(Sc,Zr)$ precipitates: (a, b, c, d) alloy Sn0, (e, f, g, h) alloy Sn5, and (I, j, k, l) alloy Sn15.

Table 4-2 Characteristics of $Al_3(Sc,Zr)$ precipitates in the experimental alloys.

Alloys	Aging condition	N_v ($\times 10^{22}$ m^{-3})	D (nm)
Sn0	One-step	1.17 ± 0.11	5.3 ± 0.9
	Two-step	1.19 ± 0.16	5.2 ± 1.8
Sn5	One-step	1.16 ± 0.9	5.2 ± 1.4
	Two-step	1.32 ± 0.9	5.4 ± 1.7
Sn15	One-step	0.12 ± 0.06	2.9 ± 0.7
	Two-step	1.39 ± 0.18	5.5 ± 1.4
Sr0	One-step	1.36 ± 0.17	5.1 ± 1.1
	Two-step	1.42 ± 0.22	5.2 ± 1.3
Sr6	One-step	1.38 ± 0.18	5.3 ± 1.5
	Two-step	1.53 ± 0.21	5.5 ± 1.2
Sr13	One-step	1.38 ± 0.12	5.4 ± 1.1
	Two-step	1.55 ± 0.19	5.3 ± 1.3

Figure 4-8 shows dark-field TEM images and corresponding SAEDPs for the Sr series alloys subjected to both aging treatments. In all alloys, fine $Al_3(Sc,Zr)$ nanoprecipitates were uniformly distributed in the Al matrix under both conditions, with quantitative results provided in Table 4-2. For the Sr0 alloy, the number density and diameter of precipitates were nearly identical after the one-step and two-step aging, at approximately 1.37×10^{22} m^{-3} and 5.1 nm, respectively. In contrast, the number density of precipitates in Sr6 and Sr13 increased markedly after the two-step aging, from 1.38×10^{22} m^{-3} after the one-step aging to 1.53×10^{22} m^{-3} and 1.54×10^{22} m^{-3}, respectively. Similar to the Sn series alloys, the precipitate diameters for all Sr alloys remained consistent across both aging treatments, at approximately 5.3 nm.

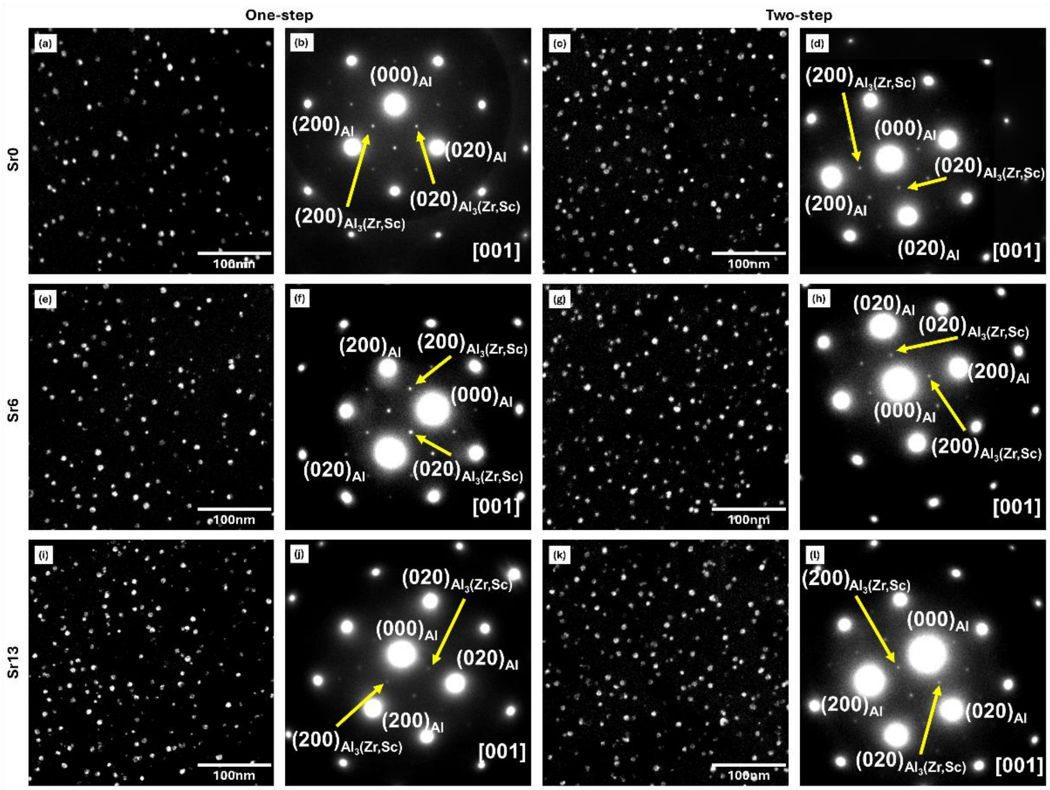

Figure 4-8 Dark-field TEM images and their corresponding SAEDPs of the Sr series alloys after one-step and two-step aging treatment, showing the $Al_3(Sc,Zr)$ precipitates: (a, b, c, d) alloy Sr0, (e, f, g, h) alloy Sr6, and (I, j, k, l) alloy Sr13.

In both alloy systems, the two-step aging process did not significantly affect the average precipitate size, which remained at approximately 5.3 nm. However, the number density of $Al_3(Sc,Zr)$ nanoprecipitates increased markedly in the Sn5, Sn15, Sr6, and Sr13 alloys compared with their traditional one-step aging counterparts. This indicates that the two-step aging process effectively promotes a higher nucleation rate of precipitates without causing excessive coarsening. The nearly unchanged size, combined with the increased number density, is consistent with the observed improvements in mechanical strength and electrical conductivity, confirming that the two-step aging enhances precipitation hardening primarily through more efficient particle formation rather than growth.

The dark-field TEM images, SAEDPs, and EDS results of the Sn15 alloy after only the first-step aging at 300 °C for 4 h are shown in Figure 4-9. The EDS analysis confirmed the presence of Sc and Zr, indicating the formation of early-stage $Al_3(Sc,Zr)$ nanoprecipitates (Figure 4-9d). As shown in Figure 4-9a and b, several tiny $Al_3(Sc,Zr)$ precipitates were observed, with an average diameter of 2.9 nm and a number density of 0.12×10^{22} m^{-3}. These precipitates likely formed during the initial aging at 300 °C owing to the presence of inoculant-rich clusters [27], which facilitated the enhanced formation of $Al_3(Sc,Zr)$ during the subsequent second-step aging. This, in turn, contributed to the increased precipitation strengthening observed in the Sn-containing alloys. Previous studies have reported that Sn exhibits favorable binding energies with vacancies in the Al lattice, whereas Sc and Zr tend to repel vacancies, as shown by first-principles calculations at 0 K, supporting Sn's role in promoting early-stage precipitation [31]. Additionally, the Sn peaks detected in the outer shell of the precipitates may suggest nearest-neighbor attractions between Zr and Sn, with these elements diffusing as dimers through a solute–vacancy exchange mechanism [27]. In this study, the addition of Sn to the Al–Zr–Sc alloys promoted cluster formation at 300 °C, significantly enhanced the early nucleation of $Al_3(Sc,Zr)$ precipitates, and increased their number density, thereby improving the mechanical properties of the alloys.

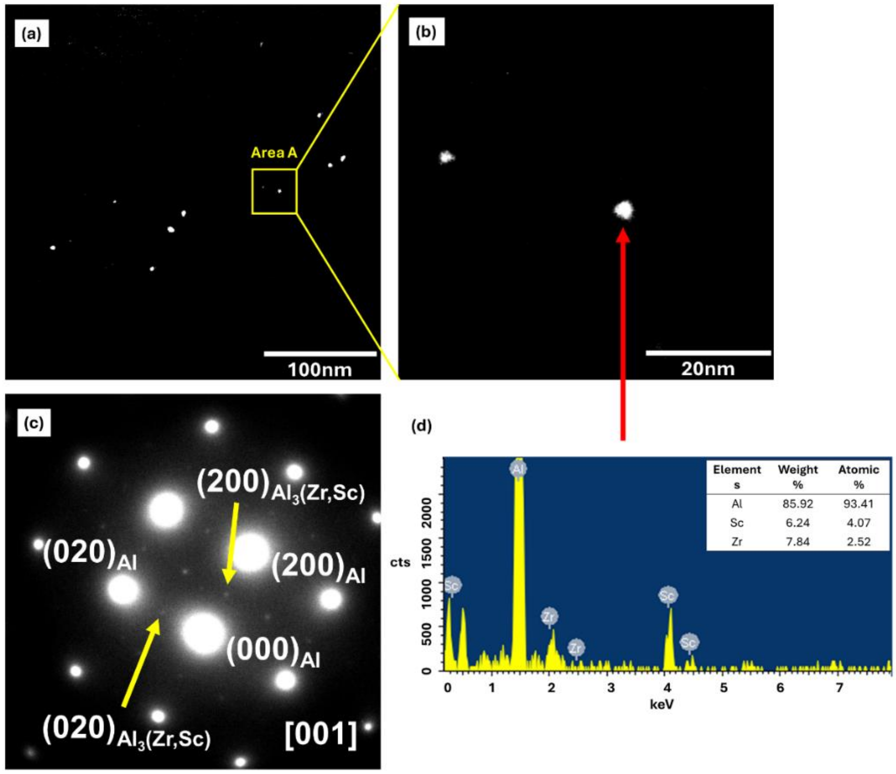

Figure 4-9 Dark-field TEM image of the Sn15 alloy after the first-step aging at 300 °C for 4 h: (a) tiny $Al_3(Sc,Zr)$ precipitates, (b) enlarged view of precipitates in area A of (a), (c) corresponding SAEDP, and (d) EDS spectrum.

Figure 4-10 shows bright-field TEM images of the Sr13 alloy after the one-step and two-step aging treatments. Dislocations are outlined with red dashed lines, and selected $Al_3(Sc,Zr)$ nanoprecipitates are indicated by yellow arrows. After the one-step aging, dislocations were often pinned by $Al_3(Sc,Zr)$ precipitates (Figure 4-10a). In contrast, after the two-step aging, a higher number density of $Al_3(Sc,Zr)$ precipitates was frequently observed in association with stacking faults and dislocations (Figure 4-10b). In general, $Al_3(Sc,Zr)$ nanoprecipitates act as effective dislocation pinning sites, and a greater precipitate density leads to stronger alloys. The frequent presence of stacking faults after the two-step aging also introduced numerous obstacles to dislocation motion [23]. As dislocations accumulated at these barriers, the increased resistance to motion strengthened the Sr-containing alloys [32, 33]. These observations are consistent with first-principles energy calculations showing that Sr and Sc can significantly lower the stacking fault energy in aluminum at 300 K [28]. A reduced stacking fault energy promotes fault formation through the slip of partial dislocations or the dissociation of full dislocations during plastic deformation [34]. In this study, adding Sr to the Al–Zr–Sc alloys promoted stacking fault formation after the two-step aging. The high density of stacking faults served as effective barriers to dislocation motion, whereas the increased number density of $Al_3(Sc,Zr)$ precipitates (Figure 4-8 and Table 4-2) simultaneously contributed to improving mechanical strength.

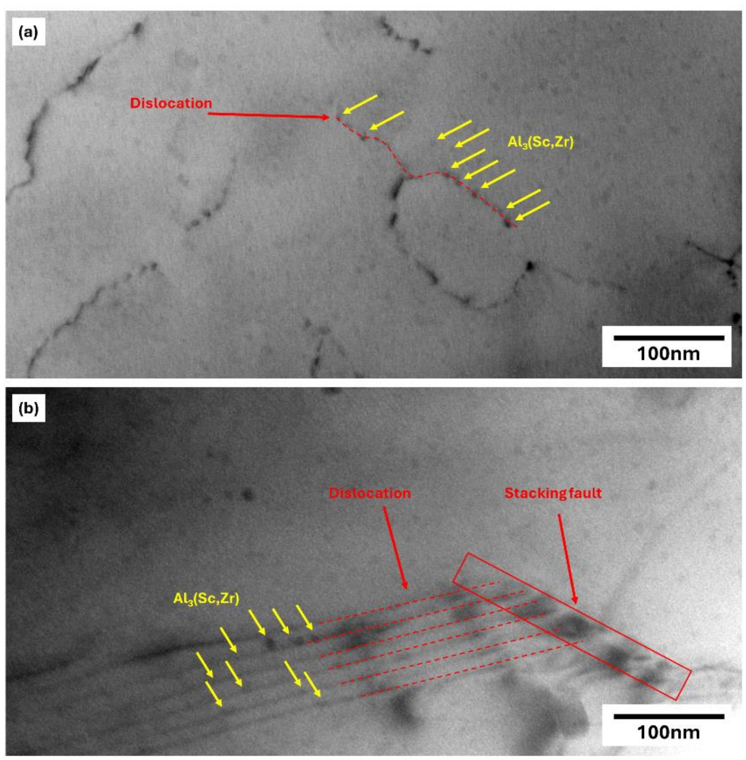

Figure 4-10 Bright-field TEM image of the Sr13 alloy: (a) after one-step aging and (b) after two-step aging.

4.3.4 Grain structure

EBSD All-Euler and grain orientation spread (GOS) maps of the Sn15 and Sr13 alloys subjected to the two aging treatments are shown in Figure 4-11, where deformed, substructured, and recrystallized grains are indicated in red, yellow, and blue, respectively, and the corresponding statistical distribution of these grain structures is presented in Figure 4-12. In both alloys, the grains in the drawn wires were elongated along the rolling direction, with deformed grains predominating. For the Sn15 alloy under one-step aging, the fractions of deformed, substructured, and recrystallized grains were 95.5%, 3.0%, and 1.5%, respectively, changing to 96.7%, 2.0%, and 1.3% after the two-step aging, indicating a slight increase in deformed grains. Retaining a higher fraction of deformed structures is associated with enhanced mechanical properties, consistent with the increases in microhardness and ultimate tensile strength reported in Section 4.3.2. A similar trend was observed in the Sr13 alloy, where the fraction of deformed grains increased from 96.0% after the one-step aging to 98.5% after the two-step aging. Notably, the two-step aging led to a slight increase in the fraction of deformed grains for both Sn15 and Sr13 alloys, accompanied by a corresponding decrease in substructured and recrystallized fractions. This increased retention of deformation structures suggests that the two-step aging effectively suppressed recovery and recrystallization, enhancing microstructural stability and improving mechanical strength.

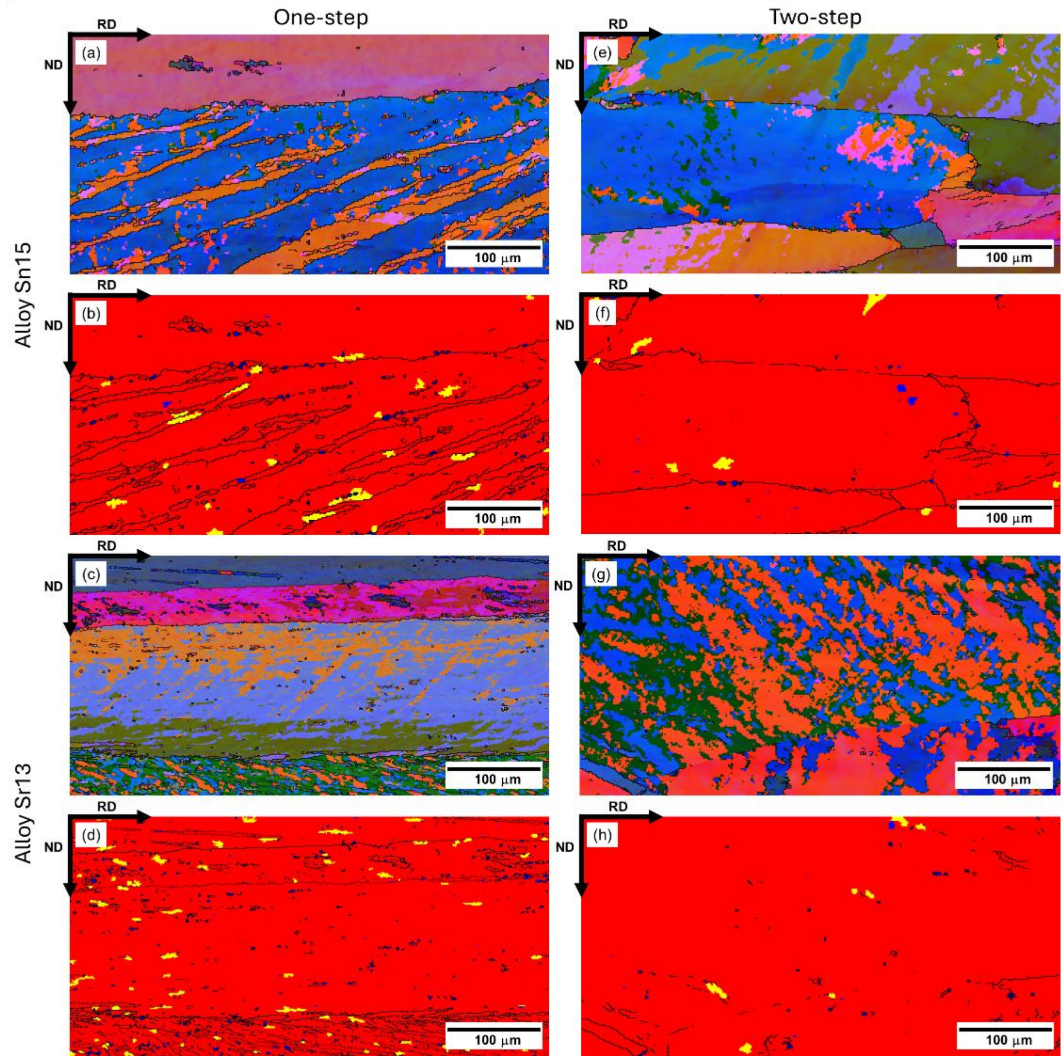

Figure 4-11 EBSD All-Euler and GOS maps under two aging conditions: (a, b) and (c, d) the one-step aging of Sn15 and Sr13 alloys, (e, f) and (g, h) the two-step aging for Sn15 and Sr13 alloys.

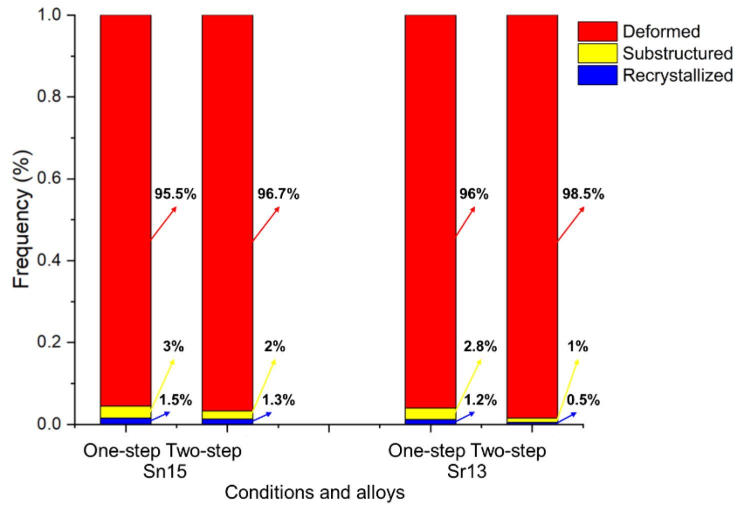

Figure 4-12 Statistical distribution of the fractions of different grain structures based on the GOS maps.

4.4 Conclusions

In this study, the effects of trace additions of Sn and Sr, combined with a novel two-step aging treatment, on the microstructure and mechanical properties of Al–Zr–Sc conductor alloys were systematically investigated. The alloy performance, evaluated in terms of microhardness, EC, and tensile strength, was examined in relation to the precipitation behavior and grain structure characteristics. The key findings are as follows:

1. The additions of trace Sn and Sr, combined with the two-step aging, significantly improved the mechanical strength and EC of Al–Sc–Zr conductor alloys, demonstrating their effectiveness in optimizing conductor performance. The microhardness of the Sn15 and Sr13 alloys after the two-step aging reached 78 HV and 83 HV, respectively, representing an improvement of 4.1 to 5.5 HV compared with the one-step aging. The EC of the Sn15 and Sr13 alloys following the two-step aging attained 58.3% IACS and 58% IACS, respectively, showing an increase of 0.7 to 0.9% IACS.

2. The tensile strengths of the Sn15 and Sr13 alloys after the two-step aging reached 216 MPa and 227 MPa, respectively, reflecting an increase of approximately 10 to 12 MPa compared with the one-step aging.

3. The above improvements are primarily attributed to a higher number density of fine $Al_3(Sc,Zr)$ precipitates formed during the two-step aging. The early-stage formed $Al_3(Sc,Zr)$ precipitates were observed in the Sn15 alloy after the first step of aging at 300 °C for 4 h, facilitated by inoculant-rich clusters. Consequently, the precipitation of a larger number of $Al_3(Sc,Zr)$ nanoprecipitates was promoted under the two-step aging, leading to improved precipitation strengthening.

4. In the Sr-containing alloys, enhanced strengthening was also associated with the increased dislocation resistance in the presence of stacking faults. The stacking faults introduced a high density of obstacles that effectively obstructed and pinned dislocations, further contributing to the improvement in strength.

5. The two-step aging effectively suppressed recovery and recrystallization in the drawn wires of both Sn- and Sr-containing alloys, thereby enhancing microstructural stability and improving mechanical strength.

References

[1] Murashkin MY, Sabirov I, Sauvage X, Valiev R. Nanostructured Al and Cu alloys with superior strength and electrical conductivity. Journal of materials science 2016; 51(1):33-49.

[2] Blackburn JL. Symmetrical components for power systems engineering. CRC press2017.

[3] Yuan W, Liang Z, Zhang C, Wei L. Effects of La addition on the mechanical properties and thermal-resistant properties of Al–Mg–Si–Zr alloys based on AA 6201. Materials & Design 2012; 34:788-792.

[4] Yuan W, Liang Z. Effect of Zr addition on properties of Al–Mg–Si aluminum alloy used for all aluminum alloy conductor. Materials & Design 2011; 32(8-9):4195-4200.

[5] Khelfa T, Lachhab R, Azzeddine H, Li F, Muñoz-Bolaños J, Cabrera-Marrero J et al. Thermal Stability of an Al-Mg-Si alloy after Equal Channel Angular Pressing. 2020.

[6] Shao Q, Elgallad E, Maltais A, Chen XG. Developing Al-Zr-Sc Alloys as High-Temperature-Resistant Conductors for Electric Overhead Line Applications. Light Metals 20232023, pp. 1266-1272.

[7] Glerum JA, Kenel C, Sun T, Dunand DC. Synthesis of precipitation-strengthened Al-Sc, Al-Zr and Al-Sc-Zr alloys via selective laser melting of elemental powder blends. Additive Manufacturing 2020; 36:101461.

[8] Zhang C, Jiang Y, Cao F, Hu T, Wang Y, Yin D. Formation of coherent, core-shelled nano-particles in dilute Al-Sc-Zr alloys from the first-principles. Journal of Materials Science & Technology 2019; 35(5):930-938.

[9] Liu L, Jiang J-T, Zhang B, Shao W-Z, Zhen L. Enhancement of strength and electrical conductivity for a dilute Al-Sc-Zr alloy via heat treatments and cold drawing. Journal of Materials Science & Technology 2019; 35(6):962-971.

[10] Lin JD, Seidman DN, Dunand DC. Improving coarsening resistance of dilute Al-Sc-Zr-Si alloys with Sr or Zn additions. Materials Science and Engineering: A 2019; 754:447-456.

[11] Li Liu J-TJ, Bo Zhang, Wen-Zhu Shao, Liang Zhen. Enhancement of strength and electrical conductivity for a dilute Al-Sc-Zr alloy via heat treatments and cold drawing. J. Mater. Sci. Technol. 2019; 35(6):962-971.

[12] Knipling KE, Karnesky RA, Lee CP, Dunand DC, Seidman DN. Precipitation evolution in Al–0.1 Sc, Al–0.1 Zr and Al–0.1 Sc–0.1 Zr (at.%) alloys during isochronal aging. Acta Materialia 2010; 58(15):5184-5195.

[13] Shao Q, Elgallad EM, Maltais A, Chen XG. Development of thermal-resistant Al–Zr based conductor alloys via microalloying with Sc and manipulating thermomechanical processing. Journal of Materials Research and Technology 2023; 25:7528-7545.

[14] Guan R, Shen Y, Zhao Z, Wang X. A high-strength, ductile Al-0.35 Sc-0.2 Zr alloy with good electrical conductivity strengthened by coherent nanosized-precipitates. Journal of Materials Science & Technology 2017; 33(3):215-223.

[15] Shao Q, Elgallad EM, Maltais A, Chen XG. Thermal stability of Al–Zr-Sc conductor alloys during long-term elevated-temperature exposures. Journal of Materials Research and Technology 2025; 35:164-175.

[16] Akopyan T, Letyagin N, Belov N, Fortuna A, Nguen X. The role of Sn trace addition in the precipitation behavior and strengthening of the wrought Al–Cu–Mn-based alloy. Journal of Materials Science 2023; 58(19):8210-8229.

[17] Akopyan TK, Belov NA, Letyagin NV. Effect of trace addition of Sn on the precipitation hardening in Al-Si-Cu eutectic alloy. Jom 2019; 71:1768-1775.

[18] Ma L, Tang J, Tu W, Ye L, Jiang H, Zhan X et al. Effect of a trace addition of Sn on the aging behavior of Al–Mg–Si alloy with a different Mg/Si ratio. Materials 2020; 13(4):913.

[19] Yang Z, Dong Y, Li W, Liu X, Feng H. Effect of Sr on Microstructure and Strengthening Mechanism of Al-4.6 Mg Alloy. Materials 2023; 16(15):5450.

[20] Che H, Jiang X, Qiao N, Liu X. Effects of Er/Sr/Cu additions on the microstructure and mechanical properties of Al-Mg alloy during hot extrusion. Journal of Alloys and Compounds 2017; 708:662-670.

[21] Liu T, Morales S, Karkkainen M, Nastac L, Arvikar V, Levin I et al. The combined effects of Sr additions and heat treatment on the microstructure and mechanical properties of high pressure die cast A383 alloy. Materials Science and Engineering: A 2019; 756:373-380.

[22] Ma S, Sun Y, Wang H, Lü X, Qian M, Ma Y et al. Effect of a minor Sr modifier on the microstructures and mechanical properties of 7075 T6 al alloys. Metals 2017; 7(1):13.

[23] Shi Z, He R, Chen Y, Yan H, Song H, Luo C et al. Microstructural evolution and strengthening mechanisms of a novel Al–11Si–3Cu alloy microalloyed with minor contents of Sr and Sc. Materials Science and Engineering: A 2022; 853.

[24] Zhao J, Lee L, Chang K, Hung F. A novel two-stage heat treatment with medium-temperature aging influence on microstructure, Al3 (Sc, Zr) nanoprecipitation, and application properties, enhancing selective laser melting of Al–Mg–Sc–Zr alloy. Nanomaterials 2022; 12(12):2078.

[25] Guo Z, Zhao G, Chen XG. Effects of two-step homogenization on precipitation behavior of Al3Zr dispersoids and recrystallization resistance in 7150 aluminum alloy. Materials Characterization 2015; 102:122-130.

[26] Wang M, Bian Z, Zhu A, Cai Y, Zhang D, Wu Y et al. Optimizing the Heat Treatment Method to Improve the Aging Response of Al-Fe-Ni-Sc-Zr Alloys. Materials 2024; 17(8):1772.

[27] Okle P, Lin JD, Zhu T, Dunand DC, Seidman DN. Effect of micro-additions of Ge, In or Sn on precipitation in dilute Al-Sc-Zr alloys. Materials Science and Engineering: A 2019; 739:427-436.

[28] Liu L, Chen J, Fan T, Liu Z, Zhang Y, Yuan D. The possibilities to lower the stacking fault energies of aluminum materials investigated by first-principles energy calculations. Computational Materials Science 2015; 108:136-146.

[29] Meier J, Shin D, Poplawsky JD, Allard LF, Cheng H, Ohnishi I et al. Effect of Sn microalloying on the nucleation of L12 Al3Zr precipitates in a dilute aluminum-zirconium alloy. Journal of Alloys and Compounds 2025:180433.

[30] Thermal-resistant aluminium alloy wire for overhead line conductor. International Standard IEC 62004 2007.

[31] Wolverton C. Solute–vacancy binding in aluminum. Acta Materialia 2007; 55(17):5867-5872.

[32] Xu C, Zhang J, Liu S, Jing Y, Jiao Y, Xu L et al. Microstructure, mechanical and damping properties of Mg–Er–Gd–Zn alloy reinforced with stacking faults. Materials & Design 2015; 79:53-59.

[33] Xue S, Fan Z, Lawal OB, Thevamaran R, Li Q, Liu Y et al. High-velocity projectile impact induced 9R phase in ultrafine-grained aluminium. Nature communications 2017; 8(1):1653.

[34] Zhang Z, Fu Q, Wang J, Yang R, Xiao P, Ke F et al. Simultaneously achieving strength and ductility in Ni3Al nanowires with superlattice intrinsic stacking faults. International Journal of Mechanical Sciences 2022; 215:106953.

Chapter 5

Conclusions and recommendations

5.1 General conclusions

This project focused on the development of thermally resistant aluminum conductors by optimizing Sc and Zr microalloying, evaluating their long-term thermal stability at elevated temperatures, and investigating the effects of trace additions of Sn and Sr. The objective was to improve the mechanical strength, electrical conductivity, and thermal resistance of Al-Sc-Zr alloys using cost-effective alloying strategies and processing methods. The main conclusions are as follows:

1. The addition of a low level of Sc (≤ 0.10 wt.%) to Al–Zr alloys significantly improved mechanical strength, achieving values between 188 and 209 MPa. This represents an increase of 73 to 88 % compared to the Sc-free base alloy, while maintaining high electrical conductivity in the range of 57.4 to 59.9 % IACS.

2. The strength improvement was mainly attributed to the formation of fine and dense $Al_3(Sc,Zr)$ precipitates, which exhibited much higher number density and smaller average size than the Al_3Zr precipitates in the base alloy. These features provided enhanced precipitation hardening and improved thermal resistance.

3. In the first part, both processing routes, where cold wire drawing was applied before or after aging, resulted in comparable mechanical and electrical properties. The maximum differences were 12 MPa in tensile strength and 1.4 % IACS in conductivity, offering flexibility for industrial application.

4. The thermal stability of Al–Zr–Sc alloys was systematically evaluated for the first time under long-term exposures at 310, 350, and 400 °C for up to 1000 hours. Alloys showed excellent thermal resistance and stable microstructure at 310 °C and maintained minimal strength loss at 350 °C for at least 200 hours.

5. Prolonged exposure at 400 °C led to noticeable strength degradation due to precipitate coarsening and grain recovery. Alloys with higher Zr content exhibited better thermal stability under these extreme conditions, showing smaller reduction in tensile strength, lower precipitate coarsening, and higher resistances to static recovery.

6. The introduction of trace Sn (0.05–0.15 wt.%) and Sr (0.006–0.013 wt.%), combined with optimized two-step aging, further improved microhardness, tensile strength, and electrical conductivity. Sn- and Sr-containing alloys achieved UTS values up to 215.9 MPa and 226.5 MPa, respectively, with conductivities of 58.3 % and 58.0 % IACS.

7. These enhancements were attributed to different mechanisms: Sn promoted early-stage $Al_3(Sc,Zr)$ nucleation, while Sr increased dislocation resistance by generating stacking faults. Together, these findings present a cost-effective and efficient approach to designing high-performance, thermally stable aluminum conductor alloys.

8. The excellent combinations of mechanical, electrical, and thermal-resistant properties of the Al-Zr-Sc alloys made them promising low-cost materials for manufacturing different IEC standard grades of thermal-resistant aluminium conductors with conventional or designed two-step thermomechanical processes.

5.2 Recommendations

Based on the recent findings of this study, the following recommendations could be given for future work in this area.

1. Sc is a highly effective microalloying element in Al–Zr alloys due to its ability to form fine, coherent $Al_3(Sc,Zr)$ precipitates, which significantly improve both mechanical strength and thermal stability. However, the high cost of Sc presents a challenge for widespread industrial application. Future research should focus on identifying the minimum Sc content required to achieve target property levels, particularly for strength and conductivity. Additionally, systematic studies on varying the Sc/Zr ratio could offer a pathway to optimizing precipitate morphology, number density, and coarsening resistance, while reducing reliance on expensive Sc additions.

2. To gain deeper insight into the structure, morphology, and interface characteristics of $Al_3(Sc,Zr)$ precipitates, high-resolution TEM (HRTEM) is recommended. Additionally, atom probe tomography (APT) should be employed to analyze the three-dimensional distribution, composition, and coarsening behavior of precipitates at the atomic scale.

3. While tensile properties and thermal resistance were addressed in this study, aluminum conductors in service conditions are often exposed to cyclic thermal and mechanical loads. Future studies should include low-cycle and high-cycle fatigue tests, as well as creep tests at elevated temperatures (e.g., 200–350 °C), to provide a more comprehensive assessment of long-term durability and reliability.

4. Recent studies have reported that trace additions of rare earth and metalloid elements such as erbium (Er), yttrium (Y), and antimony (Sb) can influence the precipitation behavior and

mechanical properties of aluminum alloys. These elements may modify the nucleation and growth of strengthening phases or interact with dislocations and grain boundaries. Future research should explore the effects of these elements on Al–Sc-Zr alloys.

List of publications

Journal papers:

1. Shao, Q., Elgallad, E., Maltais, A., and Chen, X. G. (2023). Developing Al-Zr-Sc Alloys as High-Temperature-Resistant Conductors for Electric Overhead Line Applications. In *TMS Annual Meeting & Exhibition, Light Metals* 2023 (pp. 1266-1272). Cham: Springer Nature Switzerland.

2. Shao, Q., Elgallad, E., Maltais, A., and Chen, X. G. (2023). Development of thermal-resistant Al–Zr based conductor alloys via microalloying with Sc and manipulating thermomechanical processing. *Journal of Materials Research and Technology,* 25, 7528-7545.

3. Shao, Q., Elgallad, E., Maltais, A., and Chen, X. G. (2025). Thermal stability of Al-Zr-Sc conductor alloys during long-term elevated-temperature exposures. *Journal of Materials Research and Technology,* 35, 164-175.

4. Shao, Q., Elgallad, E., Maltais, A., and Chen, X. G. Enhancing strength and electrical conductivity in thermal-resistant Al-Sc-Zr alloys via Sn and Sr microalloying with two-step heat treatment. (This article is under internal review.)

5. Shao, Q., Tu S., Maltais, A., and Chen, X. G. Texture evolution and mechanical property development in cold-worked Al–Sc–Zr alloys. Under preparation.

Scientific Posters:

1. High Performance Aluminum Electrical Conductor Alloys for Elevated Temperature Applications, "Quan Shao, Emad Elgallad, Alexandre Maltais, X. -Grant Chen." REGAL Students' Day, Canada, October. 2021.
2. Developing Al-Zr-Sc Alloy- Conductors for Elevated Temperature Applications, "Quan Shao, Emad Elgallad, Alexandre Maltais, X. -Grant Chen." REGAL Students' Day, Canada, October. 2022.
3. Effect of Sc addition and thermomechanical processing on the electrical, mechanical and thermal-resistant properties of Al-Zr based conductor alloys, "Quan Shao, Emad Elgallad, Alexandre Maltais, X. -Grant Chen." REGAL Students' Day, Canada, October. 2023. (Award 10 finalist poster prize).
4. Effect of Zr and Sc on the thermal stability of Al-Zr-Sc conductor alloys, "Quan Shao, Emad Elgallad, Alexandre Maltais, X. -Grant Chen." REGAL Students' Day, Canada, October. 2024. (Award 1st poster prize (Rio Tinto prize)).
5. Enhanced mechanical properties of Al-Sc-Zr conductor alloys through Sn and Sr additions and two-step aging, "Quan Shao, Emad Elgallad, Alexandre Maltais, X. -Grant Chen." COM 2025 Meets LightMAT 2025, Canada, July. 2025.